ACADEMIC YEAR 2022/2023

UNIVERSITY OF NAPLES FEDERICO II

DEPARTMENT OF EARTH SCIENCES, ENVIRONMENT AND RESOURCES

DOCTORATE OF EARTH, ENVIRONMENTAL AND RESOURCES SCIENCE
CYCLE XXXVI – COORDINATOR PROF. DI MAIO ROSA

ARCHAEOMETRIC STUDY OF CERAMIC PRODUCTION IN SOUTHERN ATBAI (EASTERN SUDAN)

PH.D. CANDIDATE
D'UVA FRANCESCO

TUTOR
PROF. MORRA VINCENZO

CO-TUTOR
PROF. DE BONIS ALBERTO

DiSTAR Dipartimento di Scienze della Terra, dell'Ambiente e delle Risorse

UNIVERSITÀ DEGLI STUDI DI NAPOLI FEDERICO II

Abstract

The entire history of northeast Africa can be rewritten if studied from the perspective of its hinterland cultural groups; for a long time erroneously considered regressive elements in its evolution.
These, able to evolve autonomously, were part of a network of mutual exchange that touched the entire northeast Africa. In particularly, those of the southern Atbai, the subject of this study, assumed a necessary role for ancient Egypt, thus redefining the idea we have today of its dominance.
In this context, the archaeometric study of the ceramic material culture of the various southern Atbai cultural groups makes it possible to investigate in a unprecedented way, for each group, the origin of the raw materials used and the choices made in the production of this material. The resulting mineral-petrographic and chemical description is obtained by processing the data collected through a specifically designed diagnostic procedure. In addition to the classical analytical techniques (PLM, FESEM-EDS, XRPD, XRF), there are two that are scarcely used in this type of study: QEMSCAN and TIMS; which are necessary to resolve the compositional complexity of the samples and determine in detail, thanks to Sr and Nd isotopic characterisation, their locality or otherwise, respectively. In order to achieve this second purpose, three presumed raw materials were also analysed by means of TIMS. In addition, a new statistical data processing method was applied to those obtained by XRF.
The analysed ceramic sampling covering the Southern Atbai cultural sequence, ranging from 6000 BC to 2000 BC and coming from fourteen archaeological sites located in the region, consists of 90 samples.
In the production of ceramic material, the cultural groups of interest used appropriately selected raw materials that, once shaped, were fired under conditions that improved over time.
The results obtained make it possible to define the contacts of the cultural groups of southern Atbai, thus helping to delineate the exchange network of the entire northeast Africa, and the course of their technological progress over time evaluating its possible correlation to the establishment and disruption of contacts.

Index

1. Introduction

In the analysis of a system, only a variation of the perspective from which it is studied can show us what was previously obscure to our knowledge; in archaeological research, one such variation lies in the transition from a processual to a post-processual ideology.
In the 1980s, this led prof. Rodolfo Fattovich (Marks and Mohammed Ali, 1980; Marks and Fattovich, 1989; Fattovich, 1982; Fattovich, Marks and Mohammed Ali, 1984), and still motivates prof. Andrea Manzo to consider cultural groups, erroneously deemed irrelevant by a process ideology, indispensable in the historical reconstruction inherent to the whole of northeast Africa (Barnard and Duistermaat, 2012; Friedman, 2002; Trigger, 1994). These groups turn out to be the ones that, from 10000 B.C. onwards (Cremaschi et al., 1986; Shiner et al., 1971), occupied the area of southern Atbai and influenced the Nile Valley in ideologies, demographics and were of crucial importance to it in terms of the supply of raw materials (Manzo, 2017).

In this context, the ceramic cultures study of existing southern Atbai cultural groups, which persist in time more than who produced them, testify the past existence and the essence, in its shades, of the producing group, thus making it possible to explore the extent of its influence in the surroundings and vice versa. The ceramic material is one of the first materials produced by man and used until today; consequently one of the main materials of our material culture. Due to its versatility of use and the easy availability of its raw material, it has proved to be widespread, thus resulting suitable as an element of comparison between different producer cultural groups.

There are two variations of perspectives that allow to extaction of as much information as possible from such material. The first lies in analysing the material with eyes belonging to a disciplinary area other than archaeology; that of the geological sciences. Indeed, examining the mineralogical, petrographic and chemical aspects of such a material makes it possible to investigate archaeometrically in a unprecedented way, for each southern Atbai cultural group, the origin of the raw materials used and the choices made in the production of this material (Quinn, 2022).

The second lies in technological and data processing methods advancement that provides new tools, thus increasing the range of available perspectives from which to analyse the system. This archaeometric study employs a classic diagnostic procedure (PLM, FESEM-EDS, XRPD, XRF) to which two analytical techniques scarcely used in this type of study are added: QEMSCAN and Sr-Nd TIMS necessary, respectively, to resolve the compositional complexity of the samples and to determine in detail, thanks to Sr and Nd isotopic characterisation, their locality or not. To define the locality, three presumed raw materials were also analysed using TIMS. In addition, a new statistical data processing method was applied to those obtained by XRF.

The data collected from each of the perspectives listed above are processed, thus providing, within the exclusively holistic vision of a multidisciplinary archaeometrical approach, a result that can best approximate the historical reality of the cultural groups of southern Atbai and their influence in the writing of that of northeast Africa.

2. Archaeological context and investigated materials

The sampling related to the Ceramic Atbai Tradition covers the cultural sequence of the area for almost the entire ceramic period (6000 - 2000 B.C.); this sequence can be divided into phases and groups. The phases considered, in descending chronological order, were Pre-Saroba, Saroba and Kassala within each of which specific cultural groups were selected: Amm Adam, Malawiya, Butana and Gash; also listed in descending chronological order (Tab. 1) (Manzo, 2017). Table 1 shows the selected archaeological sites associated with the respective group and corresponding phase, which arise from the need to define different cultural expressions to different degrees of detail.

Different culural expressions are illustrated below according to phase and group, however, not all of the following decorations are present in the sampling (Fig. 1).

In the Pre-Saroba phase (6000 - 5000 B.C.) (Fig. 1 a-g) (Tab. 1) the occupation of two areas is recorded: the first, in terms of numbers of sites, is located between the Atbara and the Gash with a tendency to spread towards Khashm el Ghirba, while the second is located to the north of the Gash (Fattovich, 1989a; Fattovich, 1990; Fattovich, 1991; Fattovich, Marks and Mohammed Ali, 1984; Manzo et al. 2012; Marks, 1987; Marks and Fattovich, 1989; Marks and Sadr, 1988). In the latter, the Amm Adam cultural group can be distinguished by the presence of mainly knobbed ware and, to a lesser extent, wavy line and rocker stamp decorated ware; the latter recorded to a greater extent at sites in the first area and comparable to the coeval ware found in the Nile Valley (Fattovich, 1990; Manzo, 2017; Manzo et al., 2012). The previously listed decorations can be combined with the surface treatment of scraping, which began to spread in the area of interest during this period (Manzo, 2012; Manzo, 2017). This treatment had already begun to occur during 7000 B.C. in the Nile Valley (Salvatori, 2012).

Later, during the Saroba phase (5000 - 4000 B.C.) (Fig. 1, h, i) (Tab. 1), variations in the ceramic tradition identifying the Malawiya cultural group emerge in sites are distributed between the Atbara and the Gash (Fattovich, 1989a; Fattovich, 1990; Fattovich, 1991; Marks and Fattovich, 1989; Marks and Sadr, 1988; Manzo et al., 2012; Shiner, 1971). The knobbed ware persists, however improved by a more finished surface and usually only along the rim, while in the Amm Adam Group it was apparently covering most of the surface of the vessel. This supports the hypothesis of continuity in the development of the regional ceramic tradition since the Pre-Saroba phase, (Fattovich, 1990a; Fattovich, Marks and Mohammed Ali, 1984; Manzo, 2012; Manzo, 2017). The wavy line decoration no longer occurs and the spaced rocker comb and alternated pivoted stamp impressed decorations appear for the first time characterising this group (Manzo, 2017). These decorations are also recorded in the Nile Valley, mainly during a Neolithic phase (Salvatori, 2012).

Subsequently, the occupied area shifts and concentrates towards the Atbara and Khor Marmareb rivers. However, sites are also recorded north of the latter and in the area near the Gash; these changes in the settlement patter occur during the Early Kassala phase (4000-3000 B.C.) (Fig. 1, j-m) (Tab. 1). As far as ceramics are concerned, in this phase rims begin to feature incisions in herringbone patterns on the lip. There are restricted orifice bowls with incised or impressed external decoration,

often organised in herringbone patterns, scraped vessels with pinched or impressed indented rim, burnished patterns, wipped ware, rippled ware and black topped ware, often decorated with parallel rows of notches on the outer surface. In addition to the surface treatment of scraping, black-topped ware occurs (Manzo, 2017). As can be seen, the ceramic tradition develops and becomes more elaborate. Some of the aspects of the ceramic types listed above can also be found in the following Nile Valley cultures: Pre-Kerma in Upper Nubia and A-Group in Lower Nubia (Manzo, 2011; Manzo et al., 2012; Manzo, 2014). All variations related to the ceramic traditions, along with one concerning the mode of subsistence, which goes from hunting-gathering, until then adopted in the Saroba and Pre-Saroba phases, to agro-pastoral, characterise the Butana Group (Manzo, 2017). Furthermore, the group, most likely characterised by a complex social structure in which some members occupied subordinate positions compared to others, became part of a more consolidated trade network (Manzo, 2017).

At the beginning of the Middle Kassala phase (3000-1800 B.C.) (Fig. 1, n-v) (Tab. 1) a shift of the occupied area towards the Gash river and the Shurab el Gash area is evident. This phase is characterized by the arising of the Proto-Gash cultural group (3000 - 2700 B.C.), which will later be replaced by the Gash cultural group from 2700 B.C. (Fattovich, 2010; Manzo, 2017). The latter can be subdivided into: Early Gash (2700-2300 BC), Middle Gash (2300-2000 BC), Classic and Late Gash (2000 - 1800 BC) (Fattovich, 1989b, Fattovich, 1991; Fattovich 1993; Fattovich, Sadr and Vitagliano 1988-1989; Fattovich and Vitagliano 1987). The division just listed is based on the ceramic typology, which over the entire phase is very diversified and elaborated. For this reason, we refer to Manzo 2017 for detailed descriptions of the ceramic typologies discriminating the groups present in the Middle Kassala phase and their similarities with those of the Nile Valley (Manzo, 2017). Form the stylistic point of view, in Early Gash Group times the ceramics are mainly characterized by comb impressed decorations covering the upper part of the vessels, often associated with rim bands of impressions made with a triangular punch and by bands of impressions of the lip, Middle Gash Group ceramics are mainly characterized by rim bands framed by horizontal parallel incisions and by back micaceous slips. Late Gash Group is characterized by impressed rim bands often with a red wzslip band on the lip and by incised rim bands, finger nail decoration and by big sized scraped bowls with pinched and/or impressed rim . In term of socio-economic setting, the characteristics that were emerging in the Butana group were consolidated, leading to a cultural group with an agro-pastoral mode of subsistence, with a hierarchical structure and representing a crucial node in a well consolidated long-distance trade network (Manzo, 2017).

In southern Atbai, the material culture has strongly regional traits. However, the parallels with the ceramic traditions of the Nile Valley lead to the assumption of an influence between the two parts, although who influenced whom in certain ages and why they originated are only partially delineated. This line of reasoning is also valid by restricting the field of observation, thus take as reference the different parts settled within the southern Atbai (Manzo, 2017).

Fig. 1) The decoration and superficial treatment of southern Atbai ceramic production. a) AAS1-235; knobbed ware b) AAS1-203; comb rocker impressed c) ASS1-201; comb rocker impressed d) AAS1-157; double point pivoting e) AAS1-28; comb rocker impressed; f) UA 50 17, wavy line; g) UA 50 3 6, wavy line; h) UA 50 1 14, double point pivoting; i) UA50-4-21, comb rocker impressed; j) KG 23c-D3-17, scraped ware; k) KG 23c-D3-17, scraped ware; l) KG 23c-D1-17A, wiped ware; m) KG 23c-D1-5, herringbone lip band; n) JH1-20, double incised chevron o) JH1-25, engobe muscovite; p) JH1-7, black topped ware; r) 1Bis-1, Incised (1c) x 3; s) 1D-1, incised (6) t) 3-1; incised (9); u) 6-2, incised (16b); v) 4Bis-1, texturing.

Tab. 1) The sampling investigated associated with the respective decoration, archaeological sites, phase and group (Manzo, 2017). TThe samples, for a total of 90, are divided between the various groups as follows: 33, Late Gash; 1v0, Middle Gash; 1, Early Gash; 11, Butana; 28, Malawiya; 10, Amm Adam. There are samples of doubtful belonging that can potentially fall into two groups given the impossibility, due to the excessively fragmented state, of discriminating belonging to one rather than another.

Time Span (B.C.)	Phase	Group	Site	Samples	Decoration	Superficial Treatment
2000 - 1800	Middle Kassala	Late Gash	Jebel Abu Gamal 1 (JAG1)	1C-1	impressed (18)	
				2A-1	impressed (11a)	
				3-1	incised (9)	
				3A-2	incised (11b)	
				4D-1	incised (1a, 20d) / impressed (6d)	
				4Tris-1	incised (1b)	
				6-2	incised (16b)	
			Kassla 2 (K2)	1A-1		scraped ware
				1D-1	incised (6)	rough
				4A-1	texturing (grooving)	
			Shurab el Gash 7 (SEG7)	1B-1	impressed (12b)	
				1Fine-1	impressed (2a)	
				2C-1	impressed (3b)	
				3A-1	incised (11b)	
				3B-2	incised (1b)	
				3D-1	incised (12b)	
				4E-1	incised (12b) / incised (10)	scraped ware
			Shurab el Gash 6 (SEG6)	1Bis-1	Incised (1c)*3	
				SEG6-4	Incised (1c)*3	
			Shurab el Gash 14 (SEG14)	3B-1	incised (N.d)	wiped / black top ware
			Shurab el Gash 19 (SEG19)	2B-1	incised (1b)	
			Shurab el Gash 56 (SEG56)	3C-1	impressed (12b)	
			Eriba Station 2 (ES2)	4Bis-1	texturing (grooving)	texturing (grooving)
			Egelit 4 (EG4)	6-1	incised (1a)	
			Jebel Hawra 1 (JH1)	JH1-1	crossing rim band	
				JH1-10		
				JH1-11	parallel incision	
				JH1-13		
				JH1-18		scraped ware
				JH1-19	impressed band	scraped ware
				JH1-20	douple incised chevron	
				JH1-24	crossing rim band	black topped ware

Tab. 1) (continued)

Time Span (B.C.)	Phase	Group	Site	Samples	Decoration	Superficial Treatment
				JH1-28		scraped ware
2300 - 2000		Middel Gah	Jebel Abu Gamal 1 (JAG1)	1C-1	impressed (18)	
				4D-1	incised (1a; 20d) / impressed (6d)	polished
				JAG-1928	mixed motif (2)	scraped ware
			Shurab el Gash 7 (SEG7)	3Bis-1	incised (2a)	
			Shurab el Gash 7 (SEG7)	4C-1		scraped ware
			Jebel Hawra 1 (JH1)	JH1-7		black topped ware
				JH1-9		black topped ware
				JH1-18		scraped ware
				JH1-25		muscovite engobe
				JH1-28		scraped ware
2700 - 2300		Early Gash	Jebel Abu Gamal 1 (JAG1)	1E-1	incised (1a)	
2700 - 3000		Proto - Gash				
3000 - 4000	Early Kassala	Butana	Khashm el-Ghirba 23 (KG23)	KG23-A1-2	plane ware	
				KG23-A2-2	plane ware	
				KG23-D1-5	harringbone lip band	
				KG23c-C2-13	wipped ware	
				KG23c-C2-26	wipped ware	
				KG23c-C3-3	wipped ware	
				KG23c-D1-17A	wipped ware	
				KG23c-D1-17B	plane ware	
				KG23c-D3-13		scraped ware
				KG23c-D3-17		scraped warev
			Gharab el Gash (GEG23)	7-1	incised (1b, 11d)	
4000 - 5000	Saroba	Malawiya	Upper Atbara Irrigation Scheme (UA50)	UA50-1-12	comb rocker impressed	
				UA50-1-13	comb rocker impressed	
				UA50-1-14	double point pivoting	
				UA50-1-15	comb rocker impressed	
				UA50-1-16	comb rocker impressed	
				UA50-1-18	double point pivoting	
				UA50-2-1	plane ware	
				UA50-2-2	comb rocker impressed	

Tab. 1) (continued)

Samples	Decoration	Superficial Treatment	Time Span (B.C.)	Phase	Group	Site
UA50-2-3	comb rocker impressed					Amm Adam Sation 1 (AAS1)
UA50-2-4	double point pivoting					
UA50-3-5	plane ware					
UA50-3-7	plane ware					
UA50-3-8	double point pivoting					
UA50-3-9	double point pivoting					
UA50-3-10	double point pivoting					
UA50-3-11	double point pivoting					
UA50-4-19	plane ware					
UA50-4-20	comb rocker impressed					
UA50-4-21	double point pivoting					
UA50-4-22	plane ware					
UA50-4-23	comb rocker impressed					
UA50-4-24	double point pivoting					
UA50-4-25	plane ware					
UA50-4-26	double point pivoting					
AAS1-154	double point pivoting					
AAS1-157	double point pivoting					
AAS1-158	double point pivoting					
AAS1-174	double point pivoting					
UA50-1-17	dot wavy line		5000 - 6000	Pre-Saroba	Amm Adam	Upper Atbara Irrigation Scheme (UA50)
UA50-3-6	dot wavy line					
AAS1-21	comb rocker impressed					Amm Adam Sation 1 (AAS1)
AAS1-28	comb rocker impressed					
AAS1-49	knobbed ware					
AAS1-98	knobbed ware					
AAS1-112	knobbed ware					
AAS1-201	comb rocker impressed					
AAS1-203	comb rocker impressed					
AAS1-235	knobbed ware					
					Khashm el-Ghirba	

3. Geological and geomorphological context

The spatial and temporal distribution of the archaeological sites considered covers an area consisting of two physiographic units: the western edge of the Eritrean Plateau (western Eritrea) and the alluvial plain of the southern Atbai (eastern Sudan) (Fig.1) (Costanzo et al., 2021); these are separated by the final section of the Gash River, possessing a SSE-NNW orientation.

The first, east of the Gash River, consists of portions of the Eritrean Plateau modelled into inselbergs, or whaleback formations, together with colluvial deposits extending to the Gash River. West of the latter, the second delineated by it and the Atbara, comprising mainly alluvial deposits related to the Gash and its palaeochannel system and, to a lesser extent, those related to the Atbara (Costanzo et al., 2021; Garzanti et al., 2006, Manzo, 2017). These palaeochannels demonstrate the gradual shift of the end section, together with the endoheric fan, of the Gash River from SW to NE orientation during the Late Pleistocene to Holocene period; due to regional tectonics and climatic and environmental fluctuations. In particular, of interest to us are the alluvial deposits of the oldest palaeochannels: those oriented to the SW that can be attributed to the Late Pleistocene (Manzo, 2017).

The origin of the loose detrital material that constitutes the alluvial deposits referred to the latter Gash palaeochannel and the colluvial ones present in the first physiographic unit is to be sought in Eritrea (Garzanti, 2006, Padoan et al., 2011). In particular, it should be ascribed to the disintegration of the lithotypes, constituting the portion of the Eritrean plateau that overlies and partially occupies the above-mentioned area, associated with a volcanic arc geotectonic context established during the closure of the Mozambique Ocean, in the Neoproterozoic. The latter ended with the continental collision between the East and West Gondwana cratons, Archean and Palaeoproterozoic respectively, which determined the metamorphic character in amphibolite facies of the above-mentioned lithotypes (Andersson et al., 2006; Drury and De Souza Filho, 1998). This was followed by a cooling and exhumation phase that imparted, partially overwriting the previous one, another character in green shale facies (Andersson et al. 2006).

These tectonic events (0.9 -0.7 Ga) led to the formation of what is now known as the Arabian Nubian Shield. It consists of Neoproterozoic rocks, with a juvenile character and mantle source (Teklay, 1997), generally composed of metamorphic lithotypes, derived from different protoliths, intrusive, volcanic and sedimentary, generally subject to the same metamorphic grade, falling mainly in the green shale facies and, in particular contexts, in the amphibolite facies, partially overlain by retrograde events in green shale one. Metamorphic rocks may also be accompanied by post-tectonic plutons (Jhonson, 2021; Abbate, 2022).

Eritrea, which occupies its southern-western part, from a geological point of view, can be divided into two domains (Ghareb, 2005): one, located in the central portion, consisting of green shale facies rocks together with intrusive rocks (Teklay, 1997), the other, located in its eastern and western marginal zones, consisting of rocks in amphibolite prograde facies followed by a retrograde green shale one; a domain, the latter, of our interest (Ghebreab, 1996; Anderssen et al. , 2006). Indeed, the portion of the Eritrean Plateau of interest, and from which all the seasonal wadis in

addition to the Gash flow downstream (Costanzo et al., 2021), is none other than the above-mentioned western marginal zone, named the Barka sub-domain, which is mainly composed of gneisses, including orthogneisses, falling within the metamorphic conditions typical of marginal zones (Drury and De Souza Filho, 1998, Andersson, 2006).

The Eritrean Plateau, as previously pointed out, also partially encroaches on the Sudan region (Fig.1) (Geological & Mineral Resources Department (G. M. R. D. Khartoum - Sudan), 1981). In that region, however, it, and thus the Barka sub-domain, can be attributed to the Khasheb Series formation (Vail, 1988; Gabert, 1960), which corresponds to the Primitive System studied by Ruxton in 1956.

Although the above-mentioned studies attribute these formations to an age that is now considered erroneous (Abbate, 2022), they nonetheless provide a valid description in terms of mineralogical occurrence and structure of the constituent lithotypes. In particular, the compositions of the gneisses, which remind ones of protoliths, vary from granitic, passing through a granodioritic, the most common, to a more mafic of a dioritic type (Ruxton, 1956).

The plain alluvial deposits in the proximity of the Atbara River are contaminated by sediments from the Continental Flood Basalt formation cut by the latter. This formation, north of the alluvial plain, is characteristic of prerift volcanism, established in the Holocene, related to the continental break-up that separated Africa from Arabia (Pik, 1997; Garzanti et al., 2006; Padoan et al., 2011).

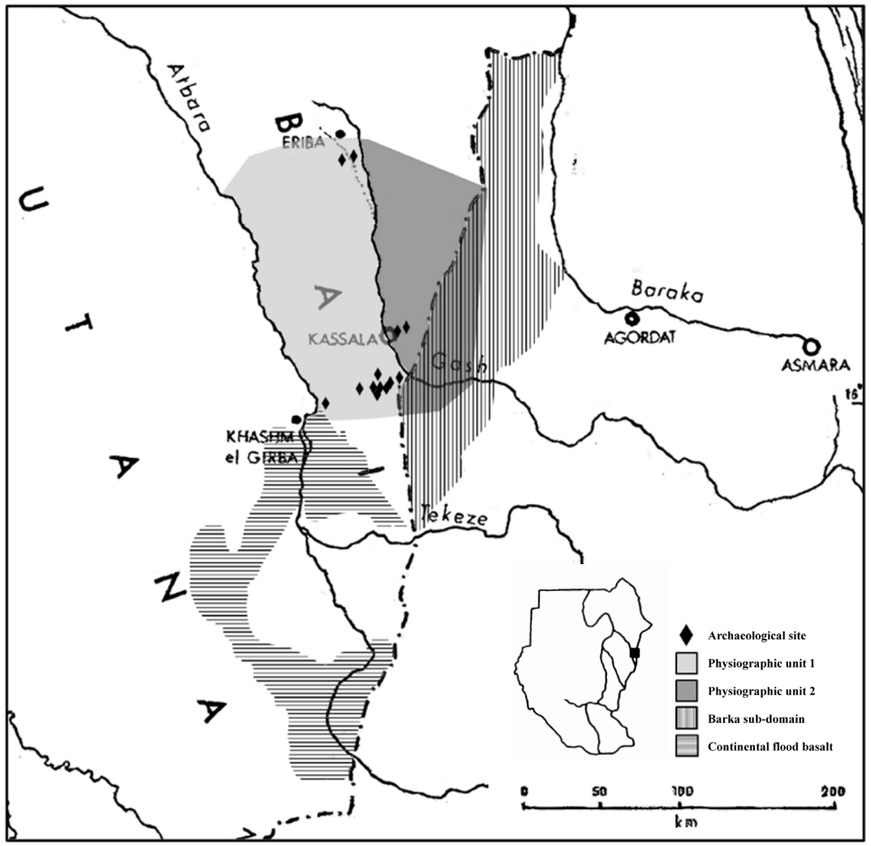

Fig. 2) Map of southern Atbai representing both the area occupied by the physiographic units and the gelogical formations of interest. In addition, the distribution of the archaeological sites from which the sample under analysis comes is illustrated. Below right a map of Sudan, indicating the exact location of the area in which the archaeological sites are distributed, is present (modified by Fattovich, Marks and Mohammed Ali, 1984).

4. Materials and methods

Ninety ceramic samples, from fourteen archaeological sites located in the southern Atbai floodplain and covering a time span from 6000 BC to 2000 BC (Tab. 1), were analysed, using a multi-analytical approach, using: polarised light microscopy (PML), high-resolution emission field scanning electron microscopy (FESEM) coupled with energy dispersive spectroscopy (EDS), automated scanning electron microscopy (QEMSCAN), X-ray powder diffraction (XRPD) and X-ray fluorescence (XRF) and thermal ionisation mass spectrometry (TIMS). In addition, three presumed raw materials sampled from one of the possible supply sites related to one of the archaeological contexts under investigation were analysed with the latter type of spectrometry.

In awareness of the uniqueness of the samples under analysis, this diagnostic procedure has been proven to be the most suitable, to date, in order to extrapolate from them the highest amount of useful information in delineating the origin of raw materials and technological knowledge present in the ceramic production

4.1. Polarised light microscopy (PML)

The observation using a polarised light microscope, employing a LEITZ Laborlux 12 POL microscope coupled with a Zeiss Axiom 105 colour camera equipped with ZEN 2.2 blue edition software/with dedicated software, is carried out with the aim of obtaining a preliminary classification and characterisation of the ceramic sample; necessary to design the idea of an optimal diagnostic procedure for its analysis. Classification and characterisation are based on the evaluation of the constituents of the main descriptive elements of the ceramic body; inclusions, porosity and matrix; and their structure considering both the individual element and the latter in relation to the entire ceramic material (Quinn, 2022).

However, this study strongly focuses on the constituents and structures of the inclusions, carrying out two observations at different degrees of detail: one relating to the entire ceramic body and one relating to individual inclusions. In addition, the qualitative mode, and later the quantitative one, will only consider mineralogical phases, including both those occurring as loose minerals and those aggregated in lithics, in a way that does not distort the effective mode. However, it is deemed necessary to create an additional mode considering lithics versus loose material.

Thin sections, 30 µm thick, were polished and metallised before the following two analyses were performed.

4.2. High-resolution emission field scanning electron microscopy (FESEM) coupled with energy dispersive spectroscopy (EDS).

Where the previous analysis did not allow the certain definition of the mineralogical phases present, and where the limits of magnification did not allow the study of mineralogical phases with small sizes, quantitative punctual chemical microanalysis was carried out by means of energy dispersive spectroscopy (EDS) conducted

with a Zeiss Merlin VP Compact high-resolution emission field scanning electron microscope (FESEM) coupled with an Oxford X-Max detector operating under the following conditions:acceleration voltage, 15 kV; probe current, variable mA; spot diameter, variable µm; acquisition time, 10 s. The instrument makes it possible to investigate elements between Be and U assessing, after appropriate calibration using the standards employed (Guarino et al., 2019; Franciosi et al., 2019), the quantity with limits of precision and accuracy reported in Risopli et al. 2019.

Where it has been deemed appropriate, the high magnifications allowed by FESEM, 1-10 µm, allow the study of important microstructural features both in section and in fresh fracture; specifically, in the latter case, features such as the degree of sintering (Maniatis and Tite, 1981; Maniatis and Tite, 1982).

4.3. Quantitative evaluation of minerals by scanning electron microscopy (QEMSCAN)

However, aware of the complex mineral-petrographic and chemical characteristics of the samples, which can only be partially resolved by means of a standard diagnostic procedure, I made use of the FEI QEMSCAN® Quanta 650F, installed at the University of Geneva (Carloni et al., 2020). The analysis concerns a properly selected sampling of 50 samples, this sampling is representative of the whole. Thanks to semi-quantitative punctual chemical microanalysis carried out at a step of 10 um, this instrument makes it possible to define the chemical variation in the area occupied by the sample in thin section, the latter appropriately polished and metallised. The instrument is operated under the following conditions:accelerating voltage, 15 kV; probe current, 10 nA; spot diameter, 2 um; acquisition time, 10 ms.

Through the processing of the chemical data acquired during the scan, it is possible to discriminate the mineralogical phases and compounds and define their quantitative mode. Here too, two observations were carried out at different degrees of detail: one relating to the entire ceramic body and one relating to individual inclusions; from which it will also be possible to extract structural and microstructural evidence.

By virtue of this, the mineralogical phase database of the University of Geneva was implemented during the analysis of the samples under consideration, creating the elementary definitions of the following phases:tschermakite, ferrotschermakite, magnesiohornblende, ferrohornblende, tremolite, actinolite, ferro-actinolite, magnesiohstingsite, hastingsite, pargasite, ferropargasite, edenite, ferro-edenite, anthophtllite/cummingtonite, ferro-anthophyllite/grunerite, diopside, hedenbergite, augite, enstatite, ferrosilite, epidote, zoisite (Deer, Howie and Zussman, 1997a; Deer, Howie and Zussman, 1997b; Deer, Howie and Zussman, 1997c). These definitions can be read by the iDiscover programme dedicated to processing data acquired by QEMSCAN.

Furthermore, through image analysis, it was possible to obtain from the scans, appropriately binarised, granulomentric parameters such as the minimum Feret dia-

meter (mF). This diameter, expressed in millimetres, is used in the calculation of Krumbein's phi scale (ϕ_{mF} = -log2 (mF)), a fundamental scale in the description of particle size distribution (GSD). In sedimentology, this parameter is based on the effective diameter that determines the particle size of a class obtained by sieving (De Bonis et al., 2020; Folk, 1974; Friedmann, 1961).
For each sample, descriptive statistical parameters such as mean, standard deviation and skewness were extracted from the cumulative frequency distribution of the values assumed by Krumbein's phi by grafical methods inticating in Folk and Ward, 1957 (De Bonis et al., 2020; Folk, 1974; Friedmann, 1961).

4.4. X-ray powder diffraction (XRPD)

The ceramic and raw material samples, not handled, were pulverised using a PM 100 planetary ball mill in order to obtain powders suitable for the preparation of samples for the following and subsequent type of analysis.

The qualitative estimation of the mineralogy of the ceramics and raw materials, considered not handled, was determined by means of X-ray diffraction on powders, without preferential orientation, using the PANalytical X'Pert PRO 3040/60 PW diffractometer. The instrument, equipped with RTMS X'Celerator detector, operates under the following acquisition conditions: radiation, CuKα; acceleration voltage; 30kV; current through tungsten filament, 10mA; scan interval; 4-70° 2θ; using a step interval, 0.017° 2θ; step count time 66s. The Panalytical Highscore Plus 3.0c software was used to identify the mineralogical assemblage of samples by comparison with reference patterns in the ICSD database.

4.5. X-Ray fluorescence (XRF)

Chemical analysis by X-ray fluorescence spectrometry, ergo the quantitative evaluation of the values of the major elements (SiO_2, TiO_2, Al_2O_3, Fe_2O_3, MnO, MgO, CaO, Na_2O, K_2O and P_2O_5 in wt. %) and the trace elements (Rb, Sr, Y, Zr, Nb, Ba, Cr, Ni, Sc, V, Co, Cu, Zn, Ga, Hf, Ta, Pb, Th, U F, Cl, S, La, Ce, Pr, Nd, Sm and Yb in ppm), of the ceramics, not handled and reduced in powder pallets, was performed with a PANalytical Axios instrument.

Evaluation made quantitively by calibration using the standards reported in Guarino et al. 2021. The instrument is equipped with six analyser crystals, three primary collimators and two detectors, a flow counter and a scintillator, operating at different kV and mA for each analyte. Analytical uncertainties are in the order of 1%-2% and 5%-10% for major and trace elements, respectively (Cucciniello et al., 2022).

During the processing of the data obtained from the above-mentioned analysis, in order to validate or not, and at the same time potentially implement, a preliminary classification of the sampling, the chemical attributes of the latter were subjected to multivariate cluster analysis.

This analysis was performed on standardised data in order to make comparable the values assumed by the attributes taken into consideration and describing the samples. The partitioning into k groups made use of Euclidean distance functions elaborated by a ward.D. hierarchical agglomerative method; an accord this, considering the nature of the samples, deemed suitable for extrapolating significant information (Anderberg, 1973; Becker, Chambers, and Wilks, 1988; Everitt, 1974; Gordon, 1999; Hartigan, 1975; Hartigan, 1975; Legendre and Legendre, 2012; McQuitty, 1966; Murtagh, 1985; Murtagh and Legendre, 2014; Sneath and Sokal, 1973)

With the aim of identifying a set of attributes that assumed a high weight in resolving the birth of each group, as defined by the above-mentioned analysis, and aware of the limitations proposed by PCA in this study (Becker, Chambers, and Wilks , 1988; Mardia, Kent, and Bibby, 1979; Venables, and Ripley 2002), the following was done.

Working on standardised data, at first, the values outside the interquartile considering the data distribution of the values assumed by the ith attribute uhnder analysis among the k groups were assessed. The ith group whose constituents were, for almost all or all, outside the interquartile range and at the same time belonged to the same quartile, was considered to be characterised by a divergence, than the remaining groups, due the values assumed by the attribute under analysis.
Later, similar reasoning was applied analysing the values outside the interquartile considering, however, the data distribution of the values that each sample, of the ith group under analysis, assumed for the attributes describing it. Which of the latter, for almost all or all of the samples of the ith group under consideration, occurred outside the interquartile and were simultaneously part of the same quartile was considered descriptive of the existence of the group under analysis.

It was decided to use this solution rather than others, such as the PCA, as the latter did not include attributes that were considered significant and non-negligible for the method described above, the latter, in fact, simultaneously considers the behaviour of the ith group separately and in relation to the set of groups.

4.6. Thermal ionisation mass spectrometry (TIMS)

In defining the origin of the ceramic material, the isotopic composition, in terms of $^{87}Sr/^{86}Sr$ and $^{143}Nd/^{144}Nd$ isotope ratios, of a portion of the sample and raw materials was determined.

The selected samples were treated layers using an acid attack programme comprising HF, HNO_3 and HCl of Suprapur® grade. In this way, the elements contained in the samples were brought into solution and subsequently separated, from the solution produced, Sr and Nd through cation exchange resins contained in quartz columns; AG® 50W-X8 for Sr and Ln Spec® for Nd, respectively.
Isotope ratios were determined by thermal ionisation mass spectrometry (TIMS) using the ThermoFisher Triton Plus mass spectrometer On average, the mean 2σ, hence the standard error with N =180, was ± 0.000009 for Sr measurements and

± 0.000007 for Nd measurements.The measured mean values of $^{87}Sr/^{86}Sr$ for the NIST SRM 987 standard and $^{143}Nd/^{144}Nd$ for the La Jolla standard were 0.710231 ± 0.000019 (2σ, N = 169) and 0.511845 ± 0.000010 (2σ, N = 55), respectively; the external reproducibility (2σ) during the measurement period was calculated according to Deines et al. (2003). The measured $^{87}Sr/^{86}Sr$ and $^{143}Nd/^{144}Nd$ ratios were normalised for intra-analysis isotope fractionation to $^{87}Sr/^{86}Sr = 0.1194$ and $^{143}Nd/^{144}Nd = 0.7219$. The final measured values of the isotope ratio were normalised to the recommended values of the NIST SRM 987 ($^{87}Sr/^{86}Sr = 0.71025$) and La Jolla ($^{143}Nd/^{144}Nd = 0.51185$) international standards.

5. Results

5.1. Petrography and microchemistry

The following results have been obtained from the analyses described below: polarized light microscopy (PML), high resolution emission field scanning electron microscopy (FESEM) coupled with energy dispersive spectroscopy (EDS) and automated scanning electron microscopy (QEM-SCAN). The latter two techniques examined a selection of samples representative of the whole compositional and morpho-typological features.

Among the inclusions of each ceramic body, lithics beyond loose mineralogical phases commonly occur. The high grain size of lithics together with their common occurrence represent ideal conditions for investigating their paragenesis and structure. For each ceramic sample, the presence of lithics attributable to a single lithotype and, to a lesser extent, also to a secondary one is attested. In analysing the paragenesis of the lithics and the loose mineralogical phases, a coherence in mineralogical nature is defined between the two parts. The reasoning pathway listed above leads to the assertion that the inclusions in each ceramic sample derive from the disintegration of a specific lithotype to which, however, may occasionally be added those derived from the disintegration of a secondary one.

In doing so, four petrographic groups (PG) were identified: dioritic gneiss inclusion (PG-1), granodioritic gneiss inclusion (PG-2), granitic gneiss inclusion (PG-3) and tonalitic gneiss inclusion (PG-4); named according to the nature of the lithotype whose disintegration produced the inclusions analysed in them. Beginning with the petrographic group granodioritic gneiss, two petrographic sub-groups arise based on the significant occurrence, in addition to the inclusions of that group, of those resulting from the disintegration of limestone (SPG-1) or basalt (SPG-2).

PG - Dioritic gneiss inclusions (PT-1)

This group consists of three samples: SEG6-4, 1Bis-1, and UA50-4-21.

The inclusions (51.24 %, 39.50 % and 44.78 %; SEG6-4, 1Bis-1 and UA50-4-21) (Tab. 2) have both elongated and equidimensional shape and a degree of rounding that varies from angular to rounded and to sub-rounded for sample UA50-4-21 (Quinn, 2022). They show a spatial distribution between the two limits close-spaced and single-spaced (Quinn, 2022), mean average size of 4.81 Φ and a size distribution described by type of sorting very well-sorted (0.03, 0.04 and 0.03; SEG6-4, 1Bis-1 and UA50-4-21) and type of skewness nearly symmetrical for sample 1Bis-1 (-0.09) and coarse skewness for the other samples (-0.12 and -0.15; SEG6-4 and UA50-4-21) (Folk, 1974; Folk and Ward, 1957; Friedmann, 1961) (Fig. 3; Tab. 2).

The porosity (19.89 %, 11.69 % and 16.83 %; SEG6-4, 1Bis-1 and UA50-4-21) (Tab. 2) consists mainly of vugh (micro-meso) and secondarily of planar voids (micro-meso) (Quinn, 2022).

The clay matrix (28.87 %, 48.82 % and 38.39 %; SEG-6-4, 1Bis-1 and UA50-4-21) (Tab. 2) has an optical activity that varies: randomly from active to moderately active in sample SEG6-4, shifting from the margins toward the core from moderately

Tab. 2) For each sample analysed with QEMSCAN, the data are given: of the descriptive statistical parameters (mean, standard deviation and skewness) of the cumulative frequency distributions from the minimum Feret values of the inclusions, of the essential components characterising a ceramic material (inclusions, matrix, porosity) (in %) and of the modality of the mineralogical phases present as inclusions (in %).

	Site	Petrographic Group	Mean	Standard Deviation	Skewness	Inclusion	Matrix	Porsity	Quartz	K-feldspar	Plagioclase	Ca-Amphibole	(Mg-Fe-Mn-Li)-Amphibole	Clinopyroxene	Orthopyroxene	Olivine	Epidote	Biotite	Chlorite	Muscovite	Calcite	Others
SEG6-4	SEG6	PG-1	4.68	0.03	-0.12	51.24	28.87	19.89	10.23	0.48	14.98	9.07	1.86	1.25	0.95	0.01	7.68	0.02	1.06	0.14	0.01	3.50
1Bis-1	SEG6	PG-1	4.80	0.04	-0.09	39.50	48.82	11.69	7.15	0.40	9.49	15.92	0.08	1.57	0.07	0.00	1.71	0.01	1.93	0.27	0.01	0.86
UA50-4-21	UA 50	PG-1	4.95	0.03	-0.15	44.78	38.39	16.83	11.33	0.37	7.44	7.14	0.68	4.42	1.05	0.01	1.36	0.06	6.20	0.54	1.80	2.39
UA50-2-1	UA50	PG-2	4.76	0.01	-0.14	49.16	31.22	19.62	20.68	1.53	17.29	2.65	0.40	0.05	0.16	0.01	1.68	0.71	0.85	0.43	0.44	2.29
UA50-2-2	UA50	PG-2	4.76	0.01	-0.17	51.86	28.30	19.84	25.69	1.58	15.39	3.23	0.20	0.04	0.07	0.00	1.48	0.18	0.87	0.15	0.35	2.64
UA50-3-5	UA50	PG-2	4.83	0.01	-0.16	50.82	29.55	19.64	23.64	1.68	16.29	3.17	0.24	0.06	0.13	0.00	1.17	0.47	1.03	0.26	0.32	2.35
1A-1	K2	PG-2	4.87	0.03	-0.12	47.45	34.28	18.27	22.72	4.17	15.07	0.74	0.07	0.03	0.01	0.00	0.82	0.58	1.47	0.54	0.01	1.22
AAS1-174	AAS1	PG-2	5.04	0.02	-0.13	57.53	26.90	15.57	35.99	3.61	11.25	0.78	0.09	0.07	0.01	0.00	1.11	0.39	1.47	0.44	0.01	2.31
UA50-1-14	UA50	PG-2	4.92	0.02	-0.15	52.26	31.01	16.73	27.12	3.70	13.09	0.99	0.15	0.27	0.01	0.00	1.50	0.31	1.49	0.36	1.36	1.89
UA50-1-15	UA50	PG-2	4.96	-0.01	-0.16	53.97	28.68	17.35	27.45	3.30	15.99	1.08	0.09	0.17	0.01	0.02	1.85	0.53	1.21	0.63	0.01	1.62
UA50-1-16	UA50	PG-2	4.99	0.01	-0.11	46.28	38.92	14.80	26.26	2.82	10.68	1.15	0.07	0.10	0.01	0.00	1.50	0.64	0.65	0.70	0.25	1.43
UA50-4-24	UA50	PG-2	4.74	0.02	-0.14	51.41	27.82	20.77	26.88	6.08	12.52	1.07	0.06	0.07	0.02	0.01	1.55	0.54	0.89	0.53	0.09	1.12
AAS1-21	AAS1	PG-2	4.93	0.02	-0.15	54.49	28.69	16.82	30.38	4.25	13.18	0.82	0.12	0.09	0.01	0.00	1.16	0.33	1.32	0.43	0.07	2.33
AAS1-98	AAS1	PG-2	4.89	0.03	-0.14	55.85	30.41	13.74	37.57	3.55	10.01	0.50	0.05	0.08	0.01	0.00	0.69	0.21	0.71	0.37	0.26	1.84
UA50-3-9	UA50	PG-2	4.83	0.01	-0.17	56.86	26.25	16.89	31.59	6.68	11.61	1.42	0.11	0.06	0.10	0.00	1.33	0.05	0.57	0.17	1.12	2.04
UA50-4-20	UA50	PG-2	4.85	0.02	-0.16	54.93	24.65	20.43	32.97	3.23	11.36	1.34	0.12	0.06	0.07	0.00	1.42	0.05	0.49	0.22	1.49	2.09
UA50-4-22	UA50	PG-2	4.72	0.02	-0.15	54.80	22.69	22.51	26.91	5.09	15.80	2.10	0.08	0.08	0.09	0.00	1.56	0.17	0.30	0.27	0.66	1.68
KG23-A1-2	KG23	PG-2	4.87	0.03	-0.08	43.94	39.98	16.08	24.72	3.27	10.65	0.73	0.07	0.07	0.02	0.00	1.22	0.81	0.64	0.42	0.02	1.29
KG23c-D1-17b	KG23	PG-2	4.84	0.01	-0.15	46.88	35.77	17.35	24.19	3.34	12.72	0.99	0.11	0.04	0.01	0.00	1.63	0.50	1.14	0.41	0.01	1.80
3A-1	SEG7	PG-2	5.01	0.03	-0.10	31.31	39.75	28.94	17.48	2.60	7.09	0.43	0.04	0.07	0.01	0.00	1.00	0.41	0.52	0.36	0.01	1.28
3D-1	SEG7	PG-2	4.99	0.03	-0.13	39.04	31.66	29.30	17.43	4.87	13.07	0.65	0.07	0.04	0.01	0.00	0.59	0.12	1.19	0.08	0.01	0.92
3Bis-1	SEG7	PG-2	4.76	0.03	-0.15	46.29	28.60	25.11	19.00	2.64	16.80	2.80	0.20	0.07	0.09	0.00	1.42	0.23	1.23	0.24	0.01	1.57
5-1	GEG	PG-2	4.93	0.04	-0.11	39.81	47.08	13.11	21.59	2.13	7.82	0.71	0.09	0.16	0.01	0.00	1.14	0.31	1.40	0.43	2.59	1.43
KG23c-C2-13	KG23	PG-2	5.02	0.01	-0.16	42.04	36.39	21.56	22.72	3.03	10.70	0.86	0.06	0.11	0.02	0.00	1.55	0.14	1.37	0.33	0.04	1.12
AAS1-158	AAS1	PG-2	4.85	0.03	-0.17	47.50	36.83	15.67	29.92	2.78	9.29	0.69	0.07	0.09	0.01	0.00	0.97	0.14	1.16	0.37	0.46	1.54
UA50-3-7	UA50	PG-2	4.88	0.04	-0.12	47.71	39.51	12.78	28.77	2.65	11.02	0.70	0.06	0.09	0.01	0.00	1.14	0.42	0.76	0.41	0.02	1.66
AAS1-112	AAS1	PG-2	4.84	0.03	-0.15	48.07	33.96	17.97	28.55	2.34	10.82	0.80	0.06	0.25	0.01	0.00	1.06	0.25	1.22	0.48	0.22	2.00
1E-1	JAG1	PG-2	5.02	0.03	-0.12	39.50	37.96	22.54	19.12	5.38	10.43	0.60	0.06	0.02	0.01	0.00	0.67	0.46	1.04	0.34	0.01	1.38
3-1	JAG1	PG-2	5.02	0.04	-0.09	27.85	52.20	19.95	16.99	2.22	5.39	0.39	0.05	0.04	0.01	0.00	0.62	0.45	0.35	0.26	0.06	1.03
3A-2	JAG1	PG-2	5.01	0.04	-0.08	22.13	57.74	20.13	12.79	0.81	4.96	0.33	0.05	0.02	0.01	0.00	0.78	0.53	0.36	0.19	0.25	1.07
JAG-1928	JAG1	PG-2	5.00	0.04	-0.10	30.15	40.18	29.67	15.98	1.92	6.81	0.64	0.07	0.05	0.01	0.00	0.98	0.15	1.40	0.25	0.46	1.44
KG23c-C3-3	KG23	PG-2	4.98	0.04	-0.07	26.50	57.07	16.43	16.62	1.09	5.09	0.28	0.06	0.03	0.01	0.00	0.67	0.46	0.72	0.27	0.05	1.16
1C-1	JAG1	PG-2	4.75	0.03	-0.12	46.71	38.99	14.30	24.48	4.53	14.55	0.36	0.02	0.02	0.00	0.00	0.40	0.54	0.21	0.26	0.01	1.32
1D-1	K2	PG-2	4.91	0.03	-0.14	45.57	29.82	24.62	17.04	7.94	16.74	0.49	0.07	0.04	0.01	0.00	0.61	0.48	0.74	0.28	0.01	1.13
JH1-7	JH1	PG-2	4.96	0.02	-0.15	62.29	21.90	15.81	33.80	10.12	15.17	0.42	0.02	0.03	0.00	0.00	0.46	0.45	0.24	0.22	0.01	1.34
JH1-10	JH1	PG-2	4.89	0.03	-0.15	48.58	35.41	16.01	19.30	6.11	17.62	1.24	0.06	0.01	0.01	0.00	0.34	0.79	0.82	0.25	0.01	2.01
JH1-11	JH1	PG-2	4.95	0.03	-0.15	44.74	31.42	23.84	18.73	5.84	14.13	1.34	0.32	0.06	0.17	0.00	0.29	0.45	1.26	0.14	0.05	1.97
JH1-19	JH1	PG-2	4.96	0.03	-0.13	43.19	34.64	22.17	19.10	5.65	13.31	1.24	0.14	0.02	0.05	0.00	0.29	0.46	0.83	0.15	0.02	1.93
JH1-18	JH1	PG-2	4.86	0.03	-0.14	43.01	38.38	18.61	16.55	4.92	16.31	1.11	0.07	0.01	0.02	0.00	0.33	0.79	1.13	0.20	0.01	1.55
JH1-28	JH1	PG-2	4.92	0.03	-0.14	43.18	34.55	22.26	18.04	5.34	15.16	0.95	0.06	0.01	0.01	0.00	0.26	0.69	0.60	0.16	0.10	1.80
JH1-25	JH1	PG-2	4.95	0.03	-0.14	53.08	34.62	12.30	29.72	4.15	14.70	1.09	0.06	0.01	0.01	0.00	0.23	0.65	0.45	0.15	0.00	1.87
AAS1-157	AAS1	PG-3	4.60	0.03	-0.11	39.92	42.14	17.94	15.27	18.76	4.11	0.23	0.00	0.00	0.00	0.00	0.05	0.15	0.76	0.34	0.02	0.22
AAS1-201	AAS1	PG-3	4.87	0.03	-0.15	48.02	36.65	15.34	24.82	15.41	2.56	0.03	0.00	0.00	0.00	0.00	0.08	0.08	0.44	4.00	0.01	0.58
AAS1-203	AAS1	PG-3	4.94	0.02	-0.16	42.24	32.75	25.01	19.55	12.96	3.23	0.01	0.01	0.00	0.00	0.00	0.08	0.02	0.32	5.66	0.05	0.34
AAS1-28	AAS1	PG-3	4.72	0.03	-0.10	46.80	40.16	13.04	24.08	11.40	8.65	0.07	0.01	0.00	0.00	0.00	0.34	0.03	0.11	0.66	0.03	1.42
4Bis-1	E2	PG-4	4.73	0.02	-0.14	51.07	38.35	10.58	33.51	0.22	14.84	0.28	0.01	0.02	0.00	0.00	0.68	0.10	0.17	0.17	0.02	1.05
UA50-3-10	UA50	SPG-1	4.97	0.01	-0.15	60.08	20.03	19.89	38.17	1.26	8.98	1.61	0.09	0.19	0.04	0.00	1.85	0.07	1.13	0.15	4.58	1.95
UA50-4-19	UA50	SPG-1	4.82	0.03	-0.13	50.76	34.94	14.29	29.07	1.97	5.57	0.73	0.07	0.09	0.01	0.00	0.78	0.20	1.02	0.16	9.86	1.24
UA50-4-25	UA50	SPG-1	4.82	0.02	-0.15	56.43	24.46	19.12	39.26	2.07	6.44	0.64	0.05	0.09	0.01	0.00	0.81	0.11	0.89	0.16	4.51	1.38
KG23-C2-26	KG23	SPG-2	5.03	-0.01	-0.17	48.72	30.58	20.70	27.81	2.63	11.24	0.44	0.13	2.24	0.04	0.14	0.38	0.21	0.37	0.13	0.01	2.97
KG23c-D3-13	KG23	SPG-2	4.96	0.01	-0.14	46.79	34.74	18.46	27.14	1.83	10.71	0.55	0.17	1.88	0.06	0.06	0.68	0.33	0.57	0.19	0.02	2.59

active to active for sample 1Bis-1 and is fully active for sample UA50-4-21 (Quinn, 2022).

In sample 1Bis-1, the matrix shows an inhomogeneous shaded colouration: orange-red at the edges and a yellowish-orange colour in the core; this both in plane polarized light and crossed polars. Instead, samples UA50-4-21 and SEG6-4 show, respectively, brown and orange-brown colorations under plane polarized lights and mustard and orange-brown one with crossed polar (Quinn, 2022).

The mineralogical phases both loose and aggregated in the lithics, which modes are expressed in Tab. 2, and the structures recognized in the latter can be traced to a dioritic gneiss. Attention was mainly focused on those elements that, if further studied, could have provided valuable information about the relict and metamorphic assemblage of the dioritic gneiss whose disintegration produced the inclusions under analysis.

The pyroxenes are strongly altered and show a tendency to reorganize into amphiboles. The clinopyroxenes, augitic, show reorganizations into magnesihornblende and into actinolite (Fig. 4; Fig. 5, a-c; Fig; 6; Tab. 3), while anthophyllite crystallizes at the expense of orthopyroxene, ferrosilite (Fig. 5, d-f, Fig. 6; Tab. 3) (Deer, Howie and Zussman, 1997a; Deer, Howie and Zussman, 1997c; Leake, 1997; Spray, 1969; Winter, J.D., 2001). These rearrangements can distribute as rim, portion and recrystallizations that follow the cleavage planes (Fig. 5, a-c) (Spray, 1969; Winter, J.D., 2001). The chemistry of pyroxenes is defined both by high and low values of ratio $^{4}Al/^{6}Al$ (Fig. 7) (Deer, Howie and Zussman, 1997a).

Concerning amphiboles, in addition to those crystallised at the expense of pyroxenes (Fig. 4; Fig. 5; Fig. 11; Fig, 12; Fig, 13; Tab. 4), magnesihornblende and pargasite crystals were observed to rearrange themselves into tschermakite, magnesihornblende and pargasite but imposing an increase in ^{6}Al content at the expense of ^{4}Al (Fig. 8 a-c; Fig, 9 a-c, Tab. 4). The amphiboles described can be transformed into actinolite , anthopillyte and, to a lesser extent, into chlorite (Fig. 8, d-f; Fig. 9) (Deer, Howie and Zussman, 1997a; Leake, 1997; Spray, 1969; Winter, J.D., 2001). The above-mentioned rearrangements can also distribute themselves as rim and portions at the expense of the phase from which they originate (Fig. 8) (Spray, 1969; Winter, J.D., 2001). Noteworthy among the various mineralogical phases is the occurrence of epidote and zoisite (Fig. 8, d-f) (Deer, Howie and Zussman, 1997b).

In the lithics (~20%, ~10%, and ~20%; SEG6-4, 1Bis-1 and UA50-4-21) (Terry and Chilingar, 1955), granoblastic, decussate, and recrystallized quartz structures with irregular margins formed due to the bulging determined by the migration of grain boundaries are readable (Spray, 1969; Winter, J.D., 2001) (Fig. 10). Among the structures within individual mineralogical phases, we find in the plagioclase deformed albite gemination coupled partially with that of the pericline, whereas the microcline may exhibit deformed and/or incomplete gridiron gemination and portions replaced by orthoclase. However, there also exists the occasion where orthoclase is the host phase of the microcline (Spray, 1969; Winter, J.D., 2001).

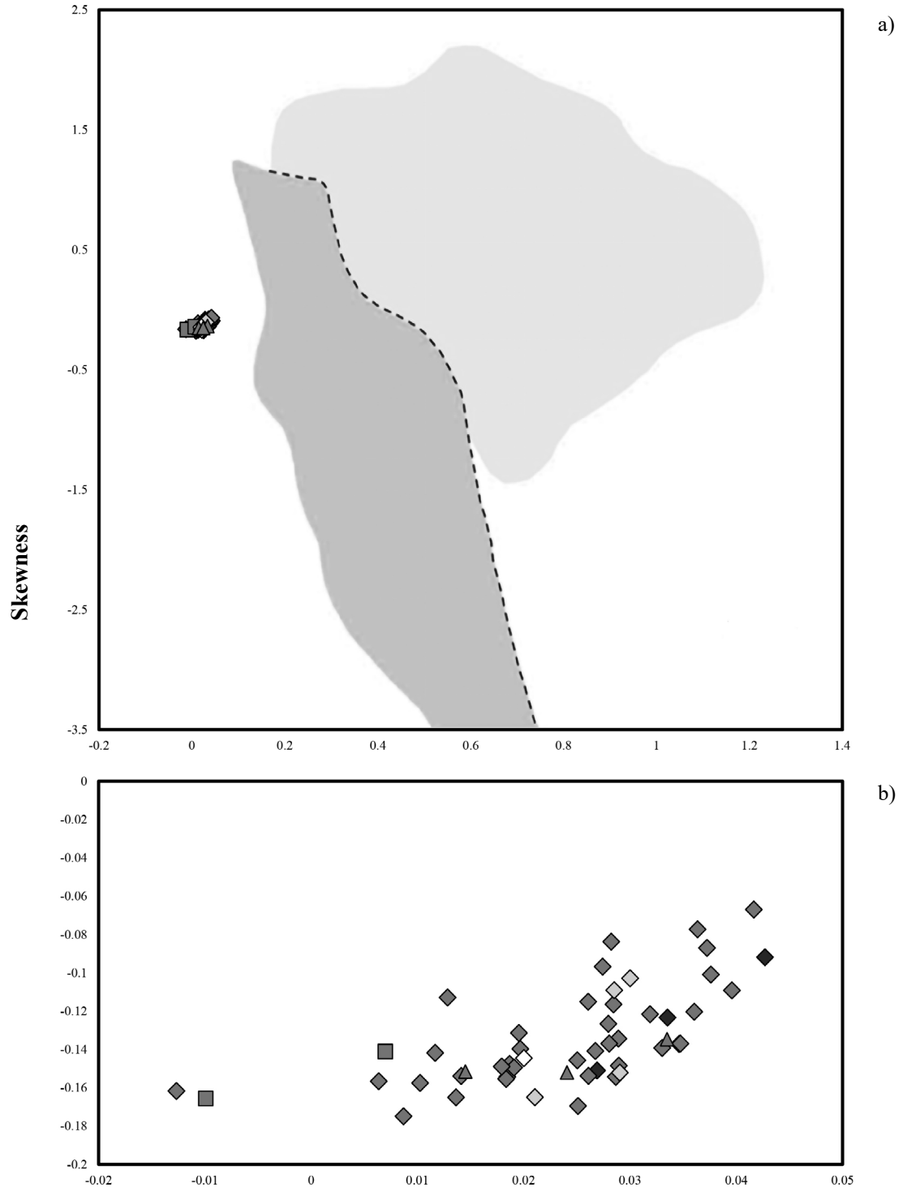

Fig. 3) Binary diagrams standard deviation versus skewness of the cumulative frequency distributions from from the cumulative frequency distribution of the values assumed by Krumbein's phi the calculated on the basis of minimum Feret values. b) results in an enlargement of a) which considers the area occupied by the samples (Folk, 1974; Folk and Ward, 1957; Friedmann, 1961). Black rhombus, PT-Dioritic gnesiss inclusion; dark grey rhombus, PT-Granodioritic gnesiss inclusions; light grey rhombus, PT-Granitic gnesiss inclusions; white rhombus, PT-Tonalitic gnesiss inclusions; dark grey square, PT-Granodioritic gnesiss + basalt inclusions; dark grey triangle, PT-Granodioritic gnesiss + limestone inclusions; light grey area, river sand; dark grey area; beach sand.

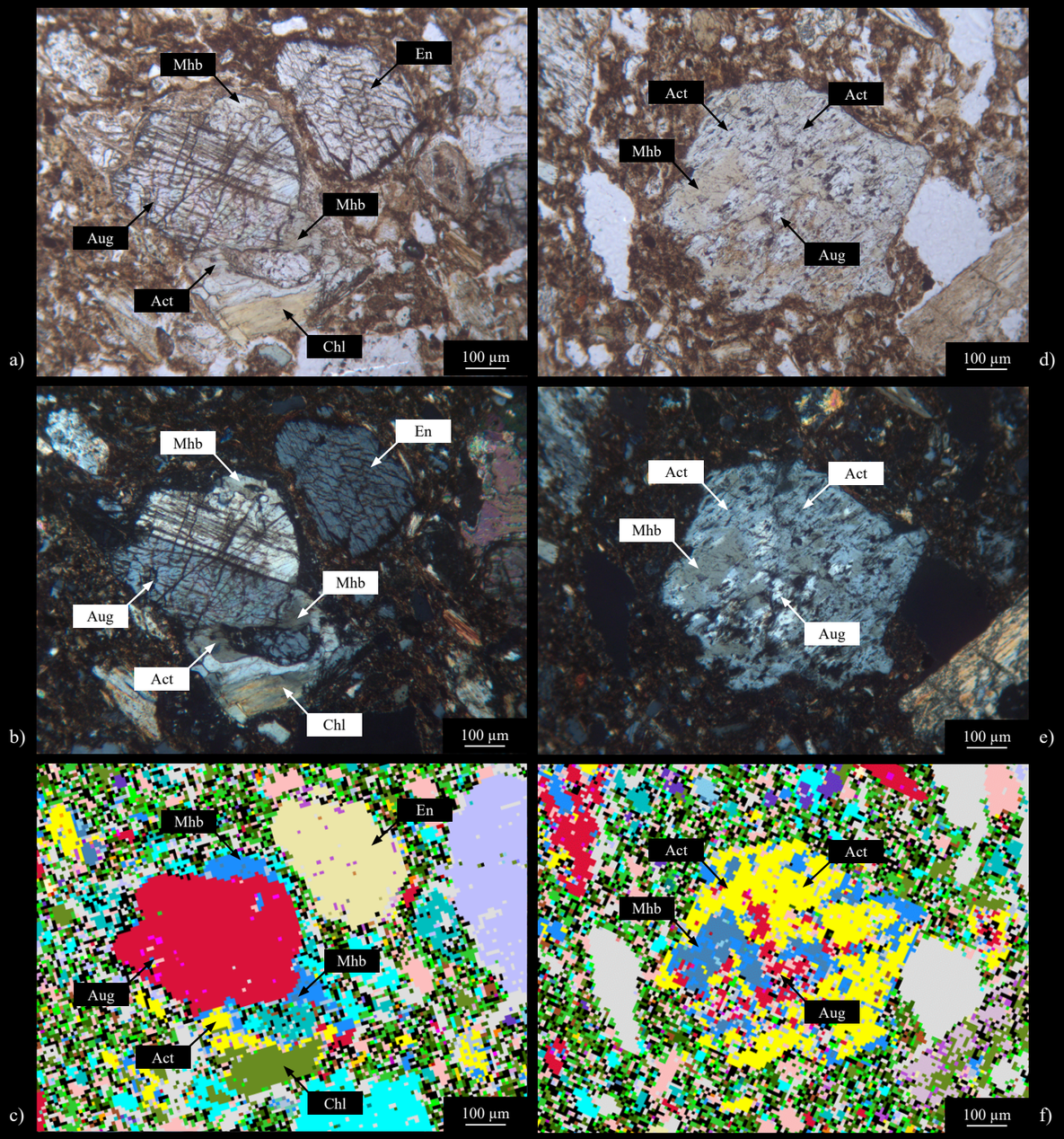

Fig. 4) UA50-4-21; Augite reorganising into magnsiohornblende, actinolite and chlorite; these recrystallisations are distributed in a rim surrounding the clinopyroxene: a) and b), Respectively plane polarized light and crossed polar view microphotographs; c) QEMSCAN scansion. UA50-4-21 Augite relict crystal almost completely replaced by magnesiohorneblende and actinolite: d) and e), Respectively plane polarized light and crossed polar view microphotographs; f) QEMSCAN scansion. Mineral abbreviation (Whitney and Evans, 2010): Act, actinolite; Aug, augite; Chl, chlorite; En, enstatite; Mhb, magnesiohornblende.

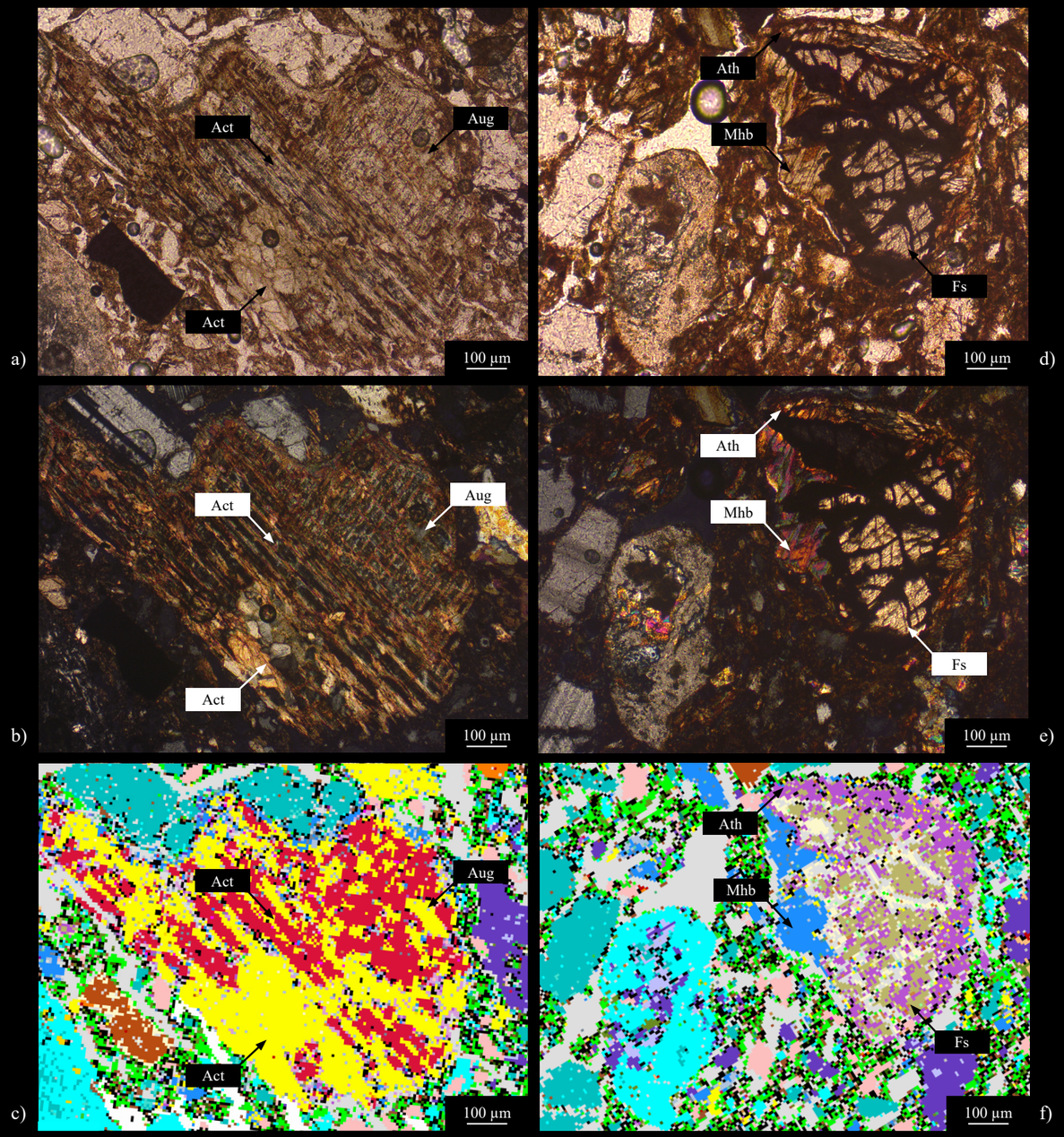

Fig. 5) SEG6-4; Augite relict crystal almost completely replaced by actinolite recrystallizations that start from the cleavage planes of the clinopyroxene: a) and b), Respectively plane polarized light and crossed polar view microphotographs; c) QEMSCAN scansion. SEG6-4; Ferro-anthophyllite and magnesiohornblende recrystallisations at the expense of ferrosilite. These recrystallisations are distributed in rim surrounding the orthopyroxene: d) and e), Respectively plane polarized light and crossed polar view microphotographs; f) QEMSCAN scansion.tion (Whitney and Evans, 2010): Act, actinolite; Aug, augite; Chl, chlorite; En, enstatite; Mhb, magnesiohornblende. Mineral abbreviation (Whitney and Evans, 2010): Act, actinolite; Aug, augite; Ath, anthophyllite; Fs, ferrosilite; Mhb, magnesiohornblende.

Tab. 3) EDS data of the pyroxene.

	UA50-4-21	UA50-4-21	UA50-4-21	UA50-4-21	UA50-4-21	UA50-4-21	UA50-4-21	UA50-4-21	UA50-4-21	SEG6-4	UA50-4-21	UA50-4-21	UA50-4-21
	PG-1	PG-1	PG-1	PG-1	PG-1	PG-1	PG-1	PG-1	PG-1	PG-1	PG-1	PG-1	PG-1
SiO_2	55.57	55.43	54.14	53.78	54.67	53.30	50.68	51.13	51.30	51.74	52.29	52.77	51.50
TiO_2	0.33	0.37	0.31	0.48	0.25	0.41	1.63	0.32	0.16	0.26	0.69	0.77	0.55
Al_2O_3	1.77	1.70	2.07	2.09	1.63	2.03	4.55	4.94	4.95	1.06	2.95	3.16	3.24
FeO	15.00	14.65	14.76	14.63	15.12	15.53	17.67	18.08	17.99	25.85	4.95	5.56	6.29
MnO	0.14	0.66	0.41	0.56	0.43	0.43	0.18	0.17	0.19	0.72	bdl	0.09	0.23
MgO	28.37	28.61	27.58	27.87	27.45	26.01	23.63	23.83	23.68	19.21	15.84	15.43	15.56
CaO	1.30	1.06	0.77	0.95	0.83	1.28	0.29	0.33	0.34	1.90	22.69	22.15	22.15
Na_2O	0.10	0.16	bdl	bdl	0.13	0.03	bdl	0.08	0.07	0.10	0.48	0.45	0.39
K_2O	bdl	bdl	bdl	bdl	bdl	bdl	0.11	bdl	bdl	0.09	bdl	bdl	0.12
BaO	bdl	bdl	bdl	bdl	bdl	bdl	0.20	0.04	bdl	bdl	bdl	0.09	bdl
SrO	bdl	bdl	0.07	bdl	0.05	bdl	0.11	bdl	0.13	0.27	bdl	0.07	bdl
Cr_2O_3	0.41	0.19	bdl	bdl	0.12	0.06	0.24	0.35	0.40	0.04	0.26	0.30	0.24
NiO	bdl	bdl	bdl	bdl	0.23	bdl	0.05	0.20	bdl	bdl	bdl	bdl	bdl
ZrO_2	0.40	0.08	bdl	bdl	bdl	bdl	bdl	bdl	bdl	bdl	bdl	bdl	bdl
V_2O_3	bdl	bdl	bdl	bdl	0.07	0.17	0.17	0.24	0.09	0.11	bdl	0.10	0.04
F	bdl	bdl	bdl	bdl	bdl	bdl	bdl	0.28	bdl	bdl	bdl	bdl	bdl
Cl	bdl	bdl	bdl	bdl	bdl	bdl	bdl	bdl	0.03	bdl	bdl	0.03	bdl
S	bdl	bdl	0.15	bdl	bdl	bdl	0.12	bdl	bdl	bdl	bdl	bdl	bdl
P_2O_5	bdl	bdl	0.04	bdl	0.06	bdl	0.05	bdl	0.03	0.13	bdl	bdl	bdl
sum	103.38	102.92	100.37	100.37	101.04	99.25	99.69	99.98	99.37	101.46	100.14	101.98	100.37
Normalized at 6 oxygens													
Si	1.93	1.93	1.94	1.92	1.95	1.93	1.86	1.87	1.88	1.94	1.91	1.92	1.89
Ti	0.01	0.01	0.01	0.01	0.01	0.01	0.05	0.01	0.00	0.01	0.02	0.02	0.02
^{IV}Al	0.07	0.07	0.06	0.08	0.05	0.07	0.14	0.13	0.12	0.06	0.09	0.08	0.11
^{VI}Al	0.00	0.00	0.02	0.01	0.02	0.02	0.06	0.08	0.09	0.00	0.04	0.05	0.04
Fe_{tot}	0.44	0.43	0.45	0.44	0.46	0.48	0.55	0.56	0.56	0.82	0.15	0.17	0.20
Fe^{3+}	0.05	0.05	0.03	0.04	0.03	0.02	0.01	0.02	0.01	0.05	0.04	0.01	0.06
Fe^{2+}	0.40	0.38	0.42	0.40	0.43	0.46	0.56	0.53	0.54	0.77	0.12	0.16	0.14
Mn	0.00	0.02	0.01	0.02	0.01	0.01	0.01	0.01	0.01	0.02	0.00	0.00	0.01
Mg	1.49	1.50	1.49	1.50	1.47	1.42	1.31	1.31	1.31	1.09	0.87	0.85	0.86
Ca	0.05	0.04	0.03	0.04	0.03	0.05	0.01	0.01	0.01	0.08	0.89	0.86	0.87
Na	0.01	0.01	0.00	0.00	0.01	0.00	0.00	0.01	0.01	0.01	0.03	0.03	0.03
K	0.00	0.00	0.00	0.00	0.00	0.00	0.01	0.00	0.00	0.00	0.00	0.00	0.01
Ba	0.00	0.00	0.00	0.00	0.00	0.00	0.00	0.00	0.00	0.00	0.00	0.00	0.00
Sr	0.00	0.00	0.00	0.00	0.00	0.00	0.00	0.00	0.00	0.01	0.00	0.00	0.00
Cr	0.01	0.01	0.00	0.00	0.00	0.00	0.01	0.01	0.01	0.00	0.01	0.01	0.01
Zr	0.01	0.00	0.00	0.00	0.00	0.00	0.00	0.00	0.00	0.00	0.00	0.00	0.00
sum	4.02	4.03	4.01	4.02	4.01	4.00	3.99	4.00	4.00	4.04	4.02	4.00	4.03
$^{IV}Al/^{VI}Al$	24.83	33.38	2.71	7.70	3.31	2.85	2.58	1.55	1.30	0.00	2.14	1.53	2.92

Tab. 3) (continued)

	1Bis-1	1Bis-1	UA50-4-21	1Bis-1	UA50-4-21	UA50-4-21	UA50-4-21	UA50-4-21	SEG6-4	KG 23c D8 13	KG 23c D8 13	KG 23c D8 13	KG 23c D3 17	KG 23c D3 17
	PG-1	PG-1	PG-1	PG-1	PG-1	PG-1	PG-1	PG-1	PG-1	SPG-2	SPG-2	SPG-2	SPG-2	SPG-2
	49.62	50.88	51.48	49.51	52.31	51.48	53.61	52.63	51.57	50.90	52.49	52.24	51.11	50.53
	0.80	0.20	0.43	0.66	0.60	0.80	0.55	0.46	0.63	0.49	0.57	0.62	0.79	0.92
	4.40	5.18	3.19	4.41	3.26	3.17	2.41	3.79	1.93	0.67	2.54	1.53	3.42	3.30
	6.06	7.54	5.59	6.48	5.92	6.04	5.95	6.38	12.37	23.10	7.16	9.92	7.03	7.27
	0.23	0.20	0.11	0.29	0.22	0.15	0.13	0.27	0.19	0.49	0.19	0.25	0.09	0.21
	14.38	14.33	15.22	14.50	14.97	14.83	15.51	14.32	13.19	17.77	17.30	16.95	15.43	15.21
	20.43	19.57	22.79	21.22	22.66	22.63	24.00	22.22	20.44	4.39	18.87	17.79	21.03	20.98
	0.50	0.81	0.40	0.67	0.42	0.57	0.43	0.56	0.33	0.23	0.32	0.25	0.40	0.37
	bdl	0.09	0.10	bdl	0.03	0.06	bdl	bdl	bdl	bdl	bdl	bdl	bdl	bdl
	bdl	0.15	0.20	bdl	bdl	0.13	bdl	bdl	bdl	bdl	bdl	bdl	bdl	bdl
	bdl	bdl	0.21	bdl	bdl	0.16	0.14	bdl	0.11	bdl	bdl	bdl	bdl	bdl
	0.30	0.36	0.31	0.34	0.27	0.35	0.17	0.48	0.18	bdl	0.81	0.09	1.03	0.82
	bdl	0.08	0.07	bdl	bdl	0.12	bdl	bdl	0.15	bdl	bdl	bdl	bdl	bdl
	0.20	bdl	bdl	0.25	bdl	bdl	bdl	0.07	bdl	bdl	bdl	bdl	bdl	bdl
	bdl	bdl	bdl	0.21	0.08	0.16	bdl	bdl	0.15	bdl	bdl	0.18	0.22	0.14
	bdl	bdl	0.04	bdl	0.20	bdl	bdl	bdl	bdl	bdl	bdl	bdl	bdl	bdl
	bdl	bdl	bdl	bdl	bdl	0.03	bdl	bdl	bdl	bdl	bdl	bdl	bdl	bdl
	bdl	0.11	bdl	bdl	0.07	0.04	bdl	bdl	0.08	bdl	bdl	bdl	bdl	bdl
	bdl	bdl	0.04	bdl	0.03	bdl	bdl	bdl	bdl	bdl	bdl	bdl	bdl	bdl
	96.94	99.50	100.19	98.54	101.03	100.70	102.90	101.19	101.33	98.04	100.25	99.82	100.55	99.75
	1.88	1.89	1.90	1.86	1.91	1.89	1.92	1.91	1.92	1.96	1.92	1.94	1.88	1.88
	0.02	0.01	0.01	0.02	0.02	0.02	0.02	0.01	0.02	0.01	0.02	0.02	0.02	0.03
	0.12	0.11	0.10	0.14	0.09	0.11	0.08	0.09	0.08	0.04	0.08	0.06	0.12	0.12
	0.08	0.12	0.04	0.06	0.05	0.03	0.03	0.08	0.01	0.00	0.03	0.00	0.03	0.02
	0.19	0.24	0.17	0.21	0.18	0.19	0.18	0.20	0.39	0.75	0.22	0.31	0.22	0.23
	0.02	0.03	0.05	0.09	0.03	0.06	0.05	0.01	0.05	0.02	0.02	0.04	0.05	0.05
	0.17	0.20	0.12	0.12	0.16	0.13	0.13	0.19	0.34	0.73	0.20	0.27	0.17	0.18
	0.01	0.01	0.00	0.01	0.01	0.00	0.00	0.01	0.01	0.02	0.01	0.01	0.00	0.01
	0.82	0.80	0.85	0.82	0.82	0.82	0.84	0.79	0.74	1.03	0.95	0.95	0.86	0.85
	0.83	0.78	0.90	0.85	0.89	0.89	0.92	0.86	0.82	0.18	0.74	0.71	0.83	0.83
	0.04	0.06	0.03	0.05	0.03	0.04	0.03	0.04	0.02	0.02	0.02	0.02	0.03	0.03
	0.00	0.00	0.00	0.00	0.00	0.00	0.00	0.00	0.00	0.00	0.00	0.00	0.00	0.00
	0.00	0.00	0.00	0.00	0.00	0.00	0.00	0.00	0.00	0.00	0.00	0.00	0.00	0.00
	0.00	0.00	0.00	0.00	0.00	0.00	0.00	0.00	0.00	0.00	0.00	0.00	0.00	0.00
	0.01	0.01	0.01	0.01	0.01	0.01	0.00	0.01	0.01	0.00	0.02	0.00	0.03	0.02
	0.00	0.00	0.00	0.00	0.00	0.00	0.00	0.00	0.00	0.00	0.00	0.00	0.00	0.00
	4.01	4.02	4.03	4.03	4.01	4.02	4.02	4.00	4.02	4.02	4.01	4.01	4.01	4.02
	1.49	0.98	2.44	2.49	1.69	3.14	3.03	1.09	6.96	0.00	2.85	22.07	4.29	5.64

Tab. 3) (continued)

	KG 23c D3 17	KG 23c D8 13	KG 23c D8 13	KG 23c D3 17	KG 23c D8 13
	SPG-2	SPG-2	SPG-2	SPG-2	SPG-2
SiO_2	50.82	50.79	50.34	50.32	48.14
TiO_2	0.97	1.08	1.26	1.26	2.28
Al_2O_3	3.73	2.60	2.72	3.60	4.43
FeO	6.78	9.27	10.35	10.61	8.92
MnO	0.06	0.25	0.37	0.33	0.33
MgO	15.20	15.16	14.66	14.59	13.53
CaO	21.82	19.72	19.10	18.96	20.82
Na_2O	0.40	0.27	0.37	0.32	0.60
K_2O	bdl	bdl	bdl	bdl	bdl
BaO	bdl	bdl	bdl	bdl	bdl
SrO	bdl	bdl	bdl	bdl	bdl
Cr_2O_3	0.73	0.17	bdl	0.27	0.09
NiO	bdl	bdl	bdl	bdl	bdl
ZrO_2	bdl	bdl	bdl	bdl	bdl
V_2O_3	0.12	0.09	0.16	0.08	0.15
F	bdl	bdl	bdl	bdl	bdl
Cl	bdl	bdl	bdl	bdl	bdl
S	bdl	bdl	bdl	bdl	bdl
P_2O_5	bdl	bdl	bdl	bdl	bdl
sum	100.63	99.40	99.33	100.34	99.29
Normalized at 6 oxygens					
Si	1.87	1.90	1.89	1.87	1.82
Ti	0.03	0.03	0.04	0.04	0.07
^{IV}Al	0.13	0.10	0.11	0.13	0.18
^{VI}Al	0.03	0.01	0.01	0.03	0.01
Fe_{tot}	0.21	0.29	0.33	0.33	0.28
Fe^{3+}	0.05	0.04	0.05	0.04	0.08
Fe^{2+}	0.16	0.25	0.28	0.29	0.20
Mn	0.00	0.01	0.01	0.01	0.01
Mg	0.84	0.86	0.83	0.82	0.77
Ca	0.86	0.79	0.77	0.75	0.84
Na	0.03	0.02	0.03	0.02	0.04
K	0.00	0.00	0.00	0.00	0.00
Ba	0.00	0.00	0.00	0.00	0.00
Sr	0.00	0.00	0.00	0.00	0.00
Cr	0.02	0.01	0.00	0.01	0.00
Zr	0.00	0.00	0.00	0.00	0.00
sum	4.02	4.02	4.02	4.02	4.03
$^{IV}Al/^{VI}Al$	4.29	6.88	7.91	4.07	12.4

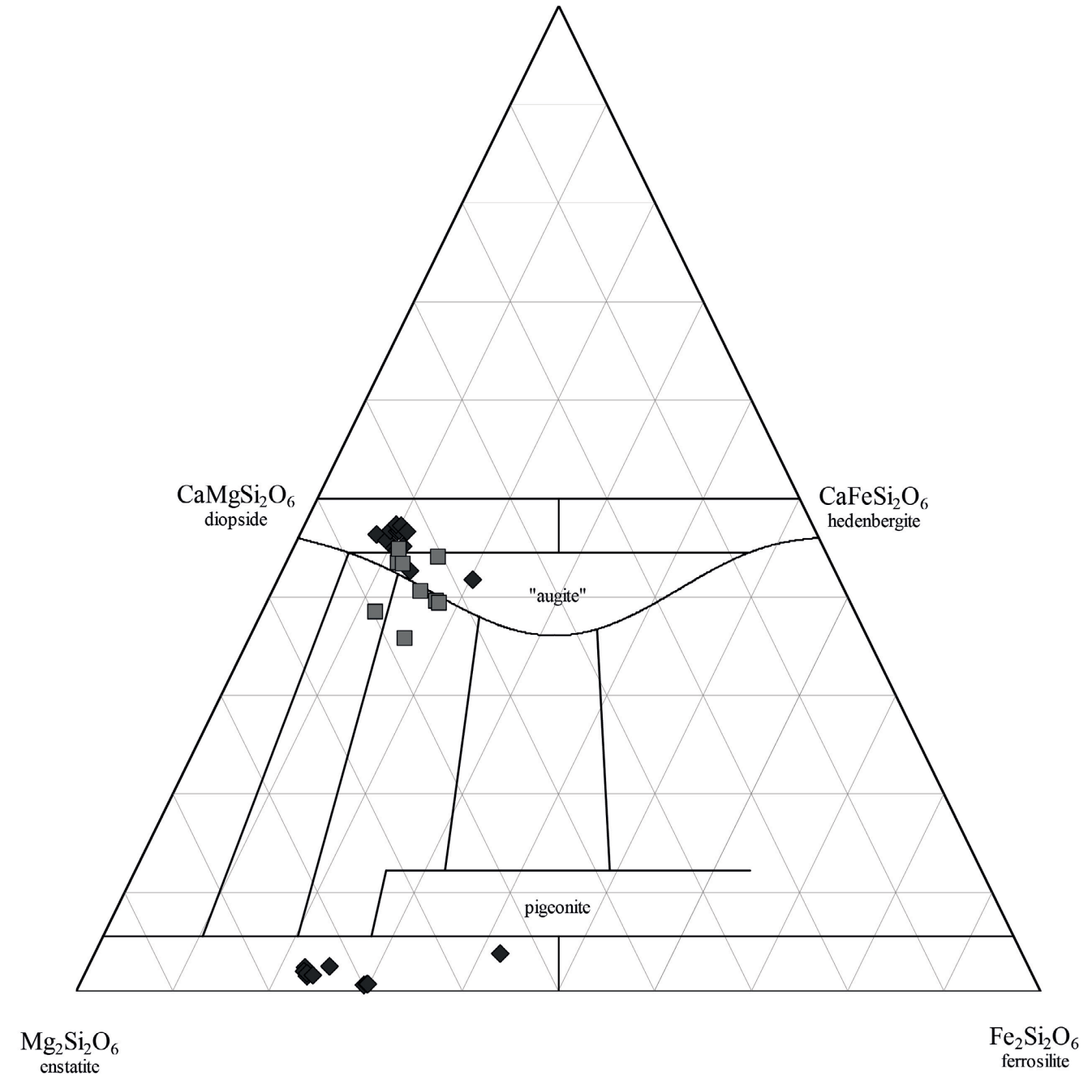

Fig. 6) Ca–Mg–Fe classification diagrams of the pyroxene. Black rhombus, PT-Dioritic Gnesiss Inclusion; dark grey square, PT-Granodioritic Gnesiss + Basalt Inclusions.

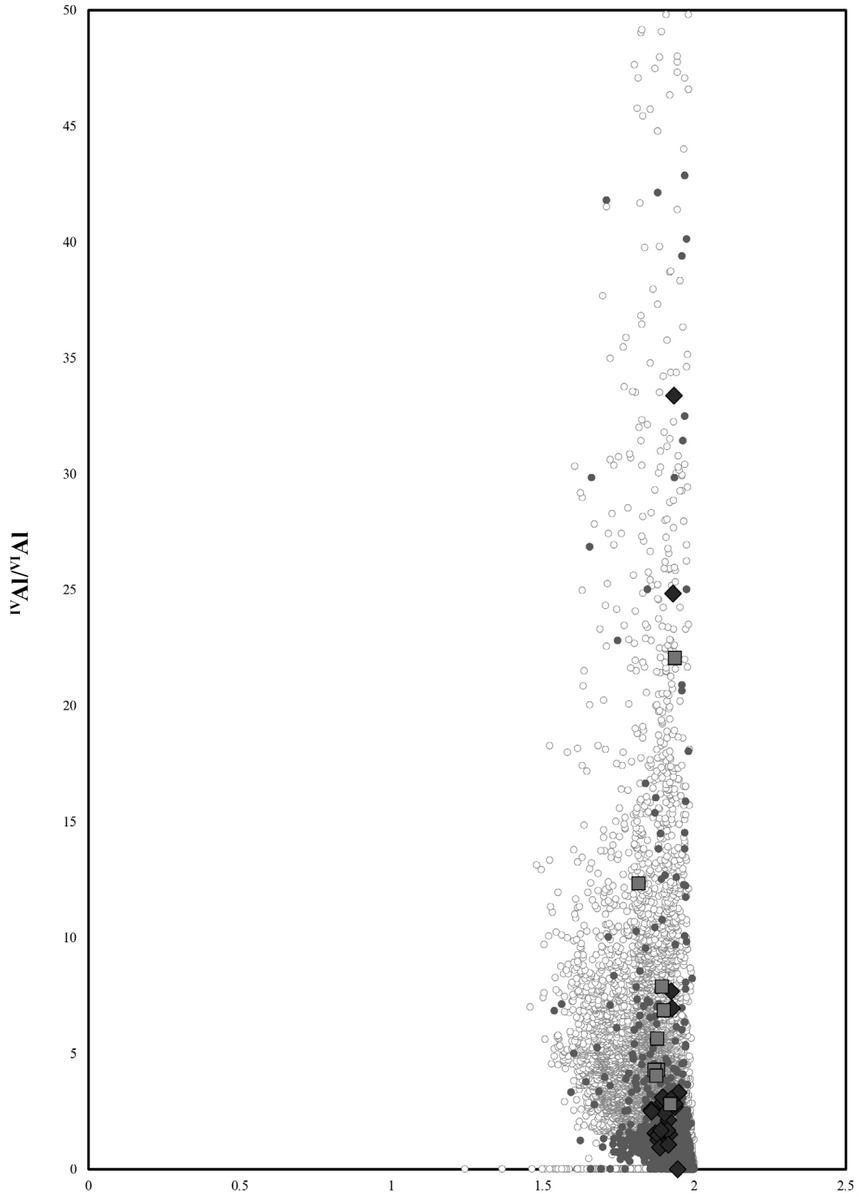

Fig. 7) Binary diagram Si (in apfu) versus $^{IV}Al/^{VI}Al$ in pyroxene. Black rhombus, PT-Dioritic Gnesiss Inclusion; dark grey square, PT-Granodioritic Gnesiss + Basalt Inclusions; dark grey square; white circles, Igneous amphibole; dark gray circles, Metamorphic amphibole. The eds data of the last two diagram elements come from the GEOROC database.

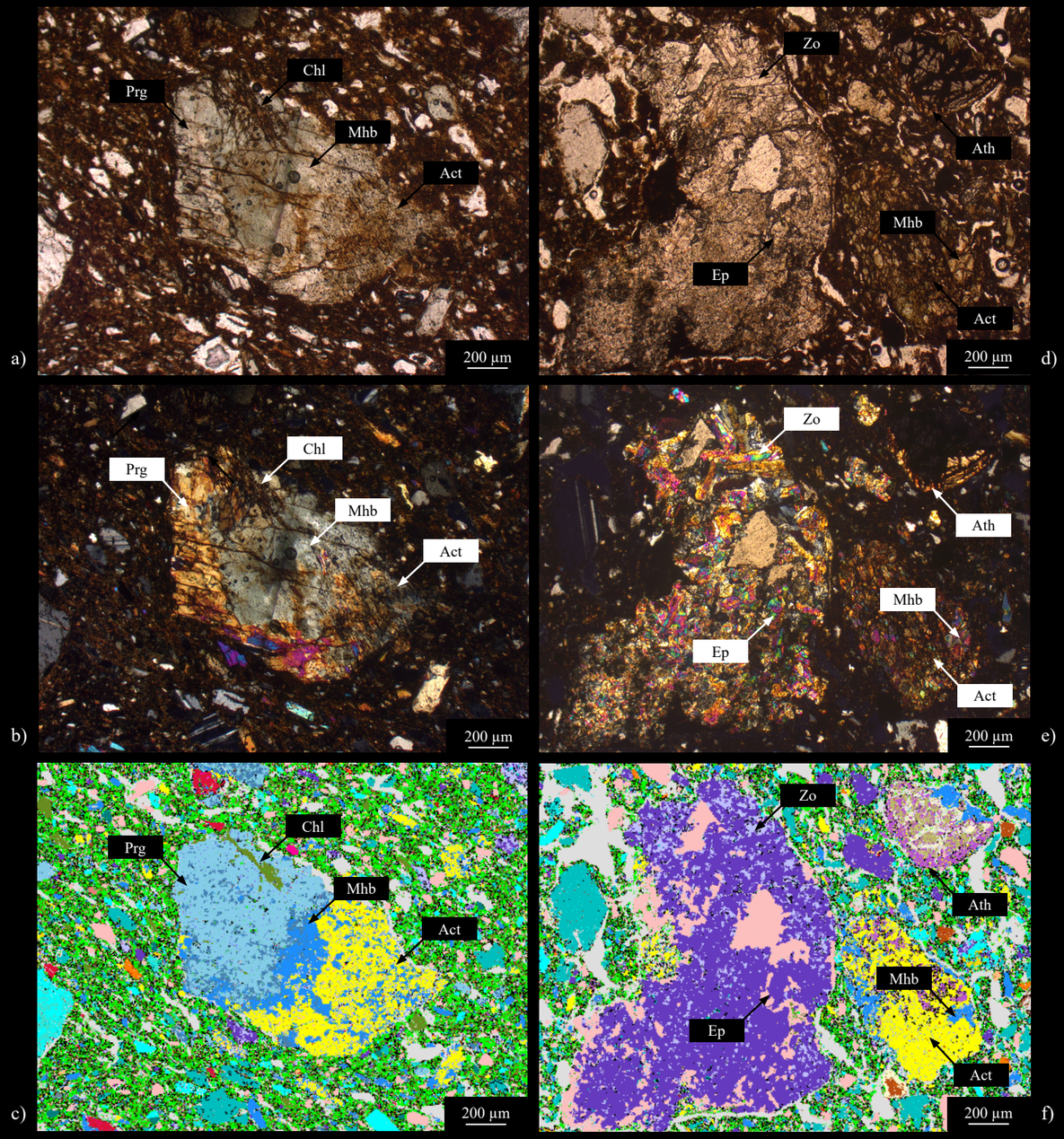

Fig. 8) 1Bis-1; Pargasite, actinolite and chlorite recrystallizzations at the expense of magnesiohornblende. These reorganisations are almost completely replacing the crystal of magnesiohornblende: a) and b), respectively plane polarized light and crossed polar view microphotographs; c) QEMSCAN scansion. 1Bis-1; Drioitic geniss lithics consists in domain of epidote and zoisite crystals (on the left) in which a decussate structure is obvious and fibrous aggregate of actinolite (on the right) in witch magneiohornblende crystals are also present: d) and e), respectively plane polarized light and crossed polar view microphotographs; f) QEMSCAN scansion. Mineral abbreviation (Whitney and Evans, 2010): Act, actinolite; Ath, anthophyllite; Ep, epidote; Mhb, magnesiohornblende; Prg, pargasite; Zo, zosite.

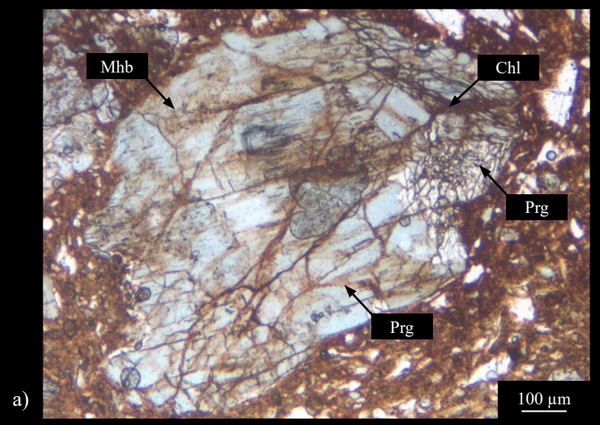

a)

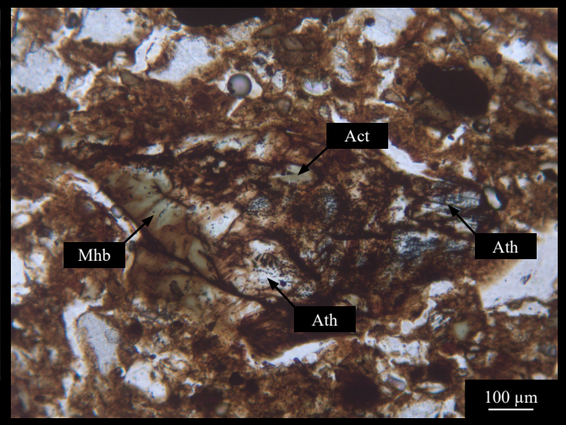

d)

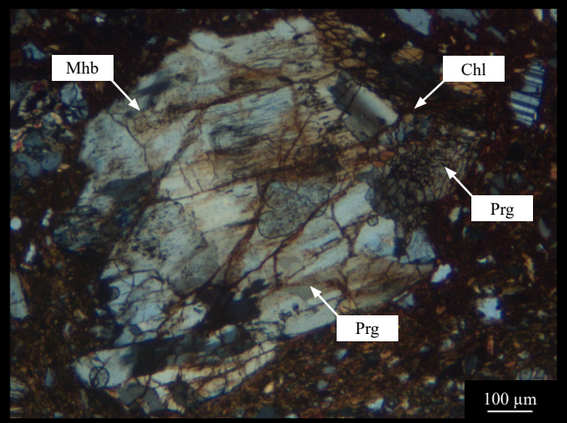

b)

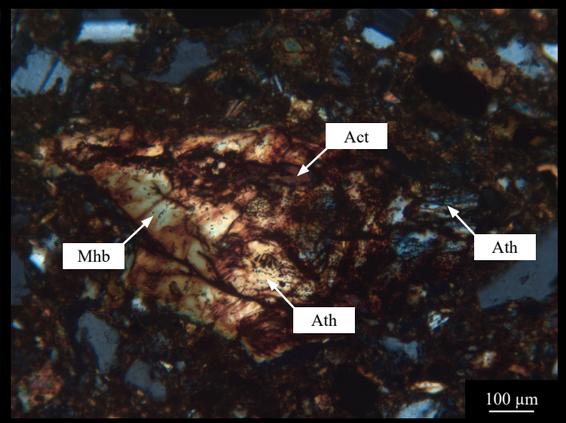

e)

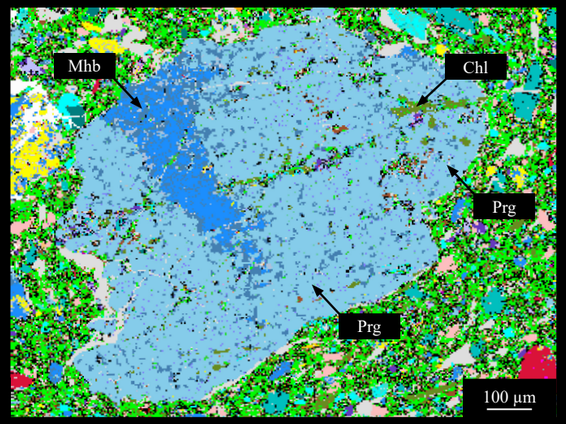

c)

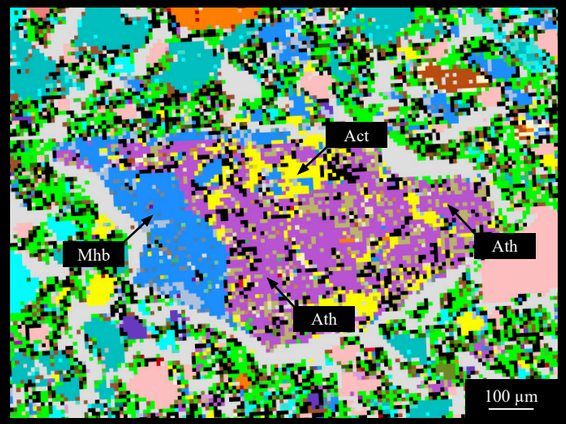

f)

Fig. 9) 1Bis-1; Recrystallisation of pargasite at the expense of a magnesiohornblende crystal, the latter being almost totally replaced. Recrystallisation goes as far as the origin of chlorite: a) and b), respectively plane polarized light and crossed polar view microphotographs; c) QEMSCAN scansion. SEG6-4; Recrystallisation of anthophyllite and actinolite at the expense of a mafnesiohornblende crystal, the latter being almost totally replaced. : d) and e), respectively plane polarized light and crossed polar view microphotographs; f) QEMSCAN scansion. Mineral abbreviation (Whitney and Evans, 2010): Act, actinolite; Ath, anthophyllite; Chl, chlorite; Mhb, magnesiohornblende; Prg, pargasite.

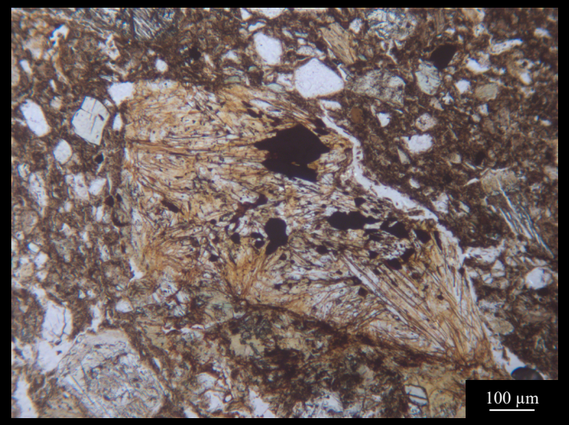

a)

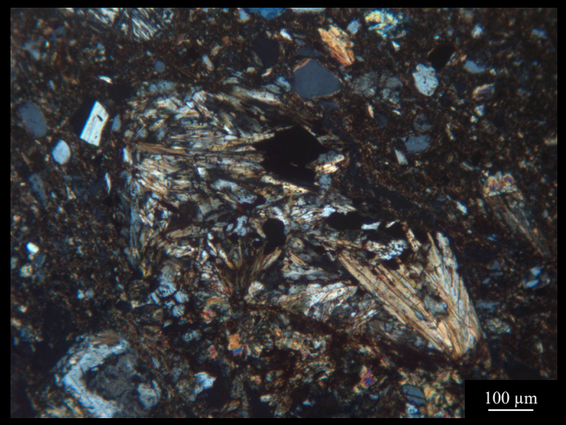

b)

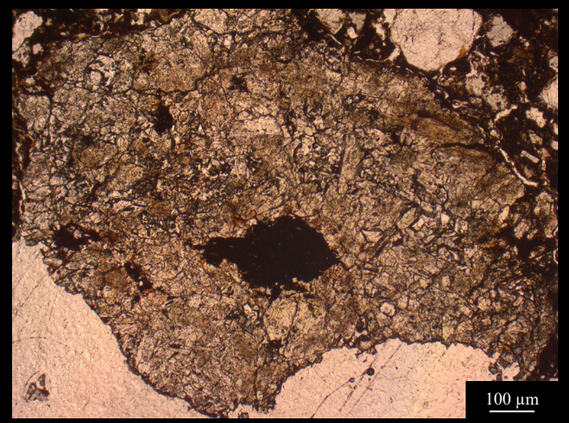

c)

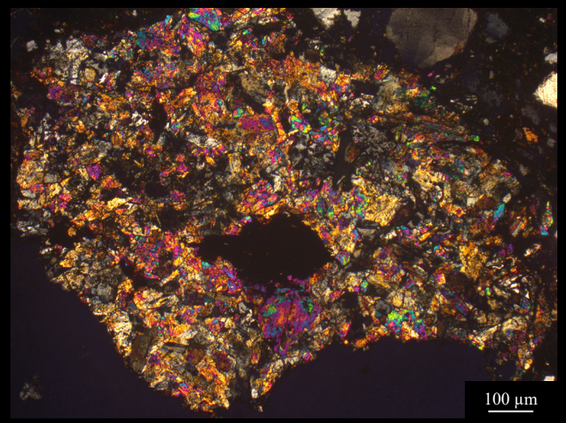

d)

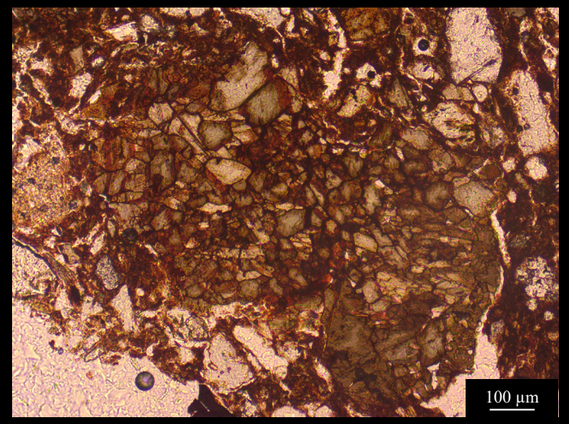

e)

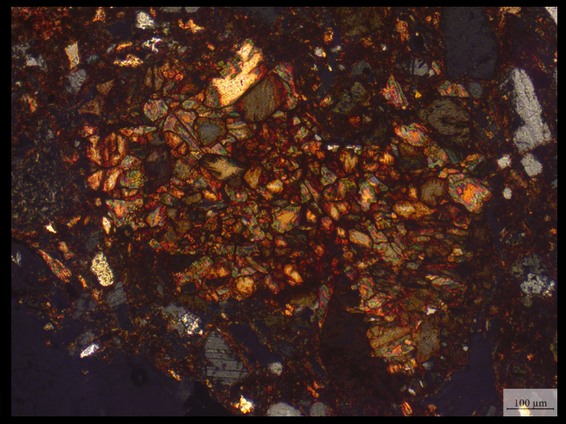

f)

Fig. 10) UA50-4-21; Drioitic geniss lithic consist in fibrous aggregate of actinolite crystals: a) and b), respectively plane polarized light and crossed polar view microphotographs. SEG6-4; Drioitic geniss lithics consists in domain of epidote and zoisite crystals: c) and d), respectively plane polarized light and crossed polar view microphotographs. SEG6-4; Drioitic geniss lithics consists in domain of magnesiohornblende crystals: e) and f), respectively plane polarized light and crossed polar view microphotographs. In all lithichs a decussate structure is obvious. Mineral abbreviation (Whitney and Evans, 2010): Act, actinolite; Ep, epidote; Mhb, magnesiohornblende; Tr, tremolite; Zo, zosite.

Tab. 4) EDS data of the amphibole.

	UA50-4-21	1Bis-1	1Bis-1	1Bis-1	1Bis-1	1Bis-1	UA50-4-21	UA50-4-21	UA50-4-21	UA50-4-21	UA50-4-21	UA50-4-21
	PG-1	PG-1	PG-1	PG-1	PG-1	PG-1	PG-1	PG-1	PG-1	PG-1	PG-1	PG-1
SiO_2	58.49	52.95	53.93	52.10	53.60	52.88	56.22	55.08	53.62	54.65	55.73	55.44
TiO_2	0.14	bdl	bdl	bdl	0.26	bdl	0.24	0.19	0.55	0.04	0.14	0.38
Al_2O_3	0.20	3.46	2.63	2.55	2.95	4.16	1.93	2.25	4.11	2.29	1.85	2.45
FeO	1.21	7.76	6.83	6.85	6.96	8.58	6.29	10.97	5.78	10.7	7.94	8.98
MnO	bdl	0.36	0.25	0.28	0.10	0.25	0.21	0.26	0.17	0.26	0.27	0.22
MgO	24.28	17.70	19.90	18.28	18.71	17.36	20.05	17.07	19.76	16.21	18.45	18.39
CaO	13.78	12.69	11.79	11.86	12.28	12.54	12.87	12.65	12.72	12.85	13.10	12.91
Na_2O	0.15	0.73	0.44	0.35	0.55	0.40	0.26	0.48	0.43	0.34	0.33	0.32
K_2O	bdl	0.20	0.06	0.08	bdl	0.10	bdl	0.13	0.13	0.07	0.09	bdl
BaO	bdl	0.30	bdl	0.15	bdl	0.23	bdl	bdl	0.19	0.28	bdl	bdl
SrO	bdl	bdl	bdl	bdl	0.15	bdl	bdl	0.28	0.26	0.04	0.21	bdl
Cr_2O_3	bdl	bdl	bdl	bdl	0.03	bdl	0.13	0.34	0.06	0.08	bdl	0.13
NiO_2	bdl	bdl	bdl	bdl	0.13	bdl	0.11	0.12	0.08	bdl	bdl	bdl
ZrO_2	0.14	bdl	bdl	bdl	bdl	bdl	bdl	bdl	bdl	bdl	bdl	bdl
V_2O_3	bdl	bdl	bdl	0.06	0.06	0.18	0.04	0.04	0.03	bdl	bdl	bdl
F	0.08	bdl	bdl	bdl	bdl	bdl	bdl	bdl	0.20	0.05	bdl	bdl
Cl	bdl	0.14	0.09	bdl	0.04	bdl	0.05	0.06	bdl	bdl	0.03	0.03
S	0.17	bdl	bdl	bdl	bdl	0.08	0.04	bdl	0.13	bdl	0.05	bdl
P_2O_5	bdl	bdl	bdl	bdl	bdl	bdl	bdl	0.11	bdl	bdl	bdl	bdl
sum	98.64	96.30	95.92	92.57	95.84	96.76	98.46	100.03	98.23	97.90	98.20	99.25v
Normalized at 23 oxygens												
Si	7.92	7.62	7.69	7.73	7.68	7.58	7.80	7.73	7.51	7.80	7.82	7.72
^{IV}Al	0.03	0.38	0.31	0.27	0.32	0.42	0.20	0.27	0.49	0.20	0.18	0.28
^{VI}Al	0.00	0.21	0.14	0.17	0.18	0.29	0.12	0.10	0.19	0.19	0.13	0.12
Ti	0.01	0.00	0.00	0.00	0.03	0.00	0.03	0.02	0.06	0.00	0.01	0.04
Cr	0.00	0.00	0.00	0.00	0.00	0.00	0.01	0.04	0.01	0.01	0.00	0.01
Fe^{3+}	0.05	0.00	0.05	0.00	0.00	0.00	0.00	0.00	0.02	0.00	0.00	0.00
Fe^{2+}	0.09	0.93	0.76	0.85	0.83	1.03	0.73	1.29	0.65	1.28	0.93	1.05
Mn	0.00	0.04	0.03	0.04	0.01	0.03	0.02	0.03	0.02	0.03	0.03	0.03
Mg	4.90	3.80	4.23	4.04	4.00	3.71	4.15	3.57	4.13	3.45	3.86	3.82
Ca	2.00	1.96	1.80	1.88	1.89	1.93	1.91	1.90	1.91	1.97	1.97	1.93
Na	0.04	0.20	0.12	0.10	0.15	0.11	0.07	0.13	0.12	0.09	0.09	0.09
K	0.00	0.04	0.01	0.02	0.00	0.02	0.00	0.02	0.02	0.01	0.02	0.00
Ba	0.00	0.02	0.00	0.01	0.00	0.01	0.00	0.00	0.01	0.02	0.00	0.00
Sr	0.00	0.00	0.00	0.00	0.01	0.00	0.00	0.02	0.02	0.00	0.02	0.00
Cr	0.00	0.00	0.00	0.00	0.00	0.00	0.01	0.04	0.01	0.01	0.00	0.01
Zr	0.01	0.00	0.00	0.00	0.00	0.00	0.00	0.00	0.00	0.00	0.00	0.00
F	0.00	0.00	0.00	0.00	0.00	0.00	0.00	0.00	0.01	0.00	0.00	0.00
Cl	0.00	0.00	0.00	0.00	0.00	0.00	0.00	0.00	0.00	0.00	0.00	0.00
S	0.01	0.00	0.00	0.00	0.00	0.00	0.00	0.00	0.00	0.00	0.00	0.00
OH	0.99	1.00	1.00	1.00	1.00	1.00	1.00	1.00	0.99	1.00	1.00	1.00
sum	16.06	16.20	16.15	16.11	16.12	16.13	16.06	16.16	16.17	16.06	16.06	16.09
$^{B}(Ca+Na)$	2.00	2.00	1.92	1.99	2.00	2.00	1.98	2.00	2.00	2.00	2.00	2.00
^{B}Ca	2.00	1.96	1.80	1.88	1.89	1.93	1.91	1.90	1.91	1.97	1.97	1.93
$^{A}(Na+K)$	0.04	0.20	0.01	0.02	0.05	0.06	0.00	0.08	0.07	0.08	0.09	0.01
^{A}Ca	0.00	0.00	0.00	0.00	0.00	0.00	0.00	0.00	0.00	0.00	0.00	0.00
$Mg/(Mg+Fe^{2+}) = X_{Mg}$	0.98	0.80	0.85	0.83	0.83	0.78	0.85	0.74	0.86	0.73	0.81	0.78
(Mg, Fe^{2+}, Mn, Li)	4.99	4.78	5.02	4.93	4.85	4.77	4.90	4.89	4.80	4.76	4.83	4.89
$^{IV}Al/^{tV}Al$	0.00	1.78	2.23	1.58	1.72	1.44	1.70	2.73	2.58	1.06	1.37	2.32

Tab. 4) (continued)

	SEG6-4	SEG6-4	SEG6-4	SEG6-4	SEG6-4	1Bis-1	1Bis-1	1Bis-1	1Bis-1	1Bis-1	1Bis-1	1Bis-1	1Bis-1	1Bis-1	1Bis-1
	PG-1	PG-1	PG-1	PG-1	PG-1	PG-1	PG-1	PG-1	PG-1	PG-1	PG-1	PG-1	PG-1	PG-1	PG-1
	53.40	55.69	54.11	51.27	52.83	45.46	51.55	44.78	51.51	49.48	50.78	50.55	50.12	45.15	51.14
	0.22	bdl	0.21	0.22	0.31	0.57	0.93	1.28	0.34	bdl	0.10	0.12	0.17	0.38	0.15
	2.60	1.19	1.45	2.67	2.55	12.37	6.10	9.94	5.16	8.83	6.48	5.72	5.97	10.11	4.73
	14.38	10.65	12.61	13.30	13.60	8.55	7.30	9.70	8.04	7.20	8.49	7.90	8.25	10.20	8.25
	0.17	0.21	0.21	0.31	0.36	0.29	0.33	0.30	0.19	0.16	0.11	0.14	0.06	0.19	0.08
	14.94	17.45	16.81	14.91	15.04	14.46	18.30	15.13	18.65	17.35	17.32	17.21	17.03	14.48	18.02
	12.11	12.62	11.95	12.11	12.23	12.08	12.10	11.94	12.67	11.73	12.20	12.00	12.19	11.84	12.23
	0.32	0.18	0.09	0.17	0.29	1.64	0.61	1.38	0.50	1.25	1.02	0.86	1.09	1.55	0.73
	0.09	0.06	0.08	0.12	0.15	0.21	0.24	bdl	0.07	0.25	0.15	0.16	0.10	0.36	0.03
	0.15	bdl	0.07	bdl	bdl	bdl	bdl	bdl	bdl	bdl	bdl	0.05	0.26	0.25	0.17
	bdl	0.13	0.10	0.24	bdl	bdl	bdl	bdl	bdl	bdl	bdl	0.09	0.28	0.06	0.26
	0.03	bdl	0.03	0.04	bdl	bdl	bdl	bdl	bdl	bdl	bdl	0.07	0.14	bdl	bdl
	0.25	0.07	bdl	0.14	0.10	bdl	bdl	bdl	bdl	bdl	0.10	bdl	0.09	bdl	bdl
	bdl	bdl	bdl	bdl	bdl	0.20	bdl	0.18	0.10	0.21	bdl	bdl	bdl	bdl	bdl
	0.10	bdl	bdl	0.06	bdl	bdl	bdl	bdl	bdl	bdl	0.07	bdl	0.10	0.09	0.07
	bdl	bdl	0.65	bdl	bdl	bdl	bdl	0.56	bdl	0.15	bdl	bdl	bdl	bdl	0.13
	bdl	bdl	bdl	0.07	0.04	0.05	0.03	0.13	0.04	0.10	0.03	0.05	0.03	0.03	0.08
	0.05	0.03	bdl	bdl	bdl	bdl	bdl	0.36	bdl	0.21	bdl	0.05	bdl	bdl	bdl
	bdl	0.09	bdl	bdl	bdl	bdl	bdl	bdl	bdl	bdl	bdl	bdl	bdl	bdl	0.12
	98.83	98.41	98.42	95.64	97.52	95.89	97.50	95.69	97.27	96.92	96.86	94.98	95.87	94.67	96.21
	7.70	7.89	7.78	7.63	7.68	6.64	7.29	6.67	7.33	7.08	7.28	7.37	7.30	6.76	7.41
	0.30	0.11	0.22	0.37	0.32	1.36	0.71	1.33	0.67	0.92	0.72	0.63	0.70	1.24	0.59
	0.14	0.08	0.03	0.10	0.12	0.77	0.31	0.42	0.20	0.57	0.38	0.35	0.32	0.55	0.22
	0.02	0.00	0.02	0.02	0.03	0.06	0.10	0.14	0.04	0.00	0.01	0.01	0.02	0.04	0.02
	0.00	0.00	0.00	0.00	0.00	0.00	0.00	0.00	0.00	0.00	0.00	0.01	0.02	0.00	0.00
	0.00	0.00	0.15	0.23	0.04	0.00	0.00	0.29	0.35	0.00	0.00	0.00	0.00	0.09	0.17
	1.73	1.26	1.37	1.42	1.61	1.04	0.86	0.92	0.61	0.86	1.01	0.96	1.00	1.19	0.83
	0.02	0.03	0.03	0.04	0.04	0.04	0.04	0.04	0.02	0.02	0.01	0.02	0.01	0.02	0.01
	3.21	3.68	3.60	3.31	3.26	3.15	3.86	3.36	3.96	3.70	3.70	3.74	3.70	3.23	3.89
	1.87	1.91	1.84	1.93	1.90	1.89	1.83	1.91	1.93	1.80	1.87	1.87	1.90	1.90	1.90
	0.09	0.05	0.03	0.05	0.08	0.46	0.17	0.40	0.14	0.35	0.28	0.24	0.31	0.45	0.21
	0.02	0.01	0.01	0.02	0.03	0.04	0.04	0.00	0.01	0.05	0.03	0.03	0.02	0.07	0.01
	0.01	0.00	0.00	0.00	0.00	0.00	0.00	0.00	0.00	0.00	0.00	0.00	0.01	0.01	0.01
	0.00	0.01	0.01	0.02	0.00	0.00	0.00	0.00	0.00	0.00	0.00	0.01	0.02	0.01	0.02
	0.00	0.00	0.00	0.00	0.00	0.00	0.00	0.00	0.00	0.00	0.00	0.01	0.02	0.00	0.00
	0.00	0.00	0.00	0.00	0.00	0.02	0.00	0.02	0.01	0.02	0.00	0.00	0.00	0.00	0.00
	0.00	0.00	0.03	0.00	0.00	0.00	0.00	0.03	0.00	0.01	0.00	0.00	0.00	0.00	0.01
	0.00	0.00	0.00	0.00	0.00	0.00	0.00	0.00	0.00	0.00	0.00	0.00	0.00	0.00	0.00
	0.00	0.00	0.00	0.00	0.00	0.00	0.00	0.01	0.00	0.01	0.00	0.00	0.00	0.00	0.00
	1.00	1.00	0.97	1.00	1.00	1.00	1.00	0.96	1.00	0.98	1.00	1.00	1.00	1.00	0.99
	16.11	16.04	16.10	16.15	16.12	16.47	16.21	16.49	16.26	16.36	16.31	16.26	16.34	16.56	16.28
	1.96	1.96	1.87	1.98	1.99	2.00	2.00	2.00	2.00	2.00	2.00	2.00	2.00	2.00	2.00
	1.87	1.91	1.84	1.93	1.90	1.89	1.83	1.91	1.93	1.80	1.87	1.87	1.90	1.90	1.90
	0.02	0.01	0.01	0.02	0.03	0.39	0.04	0.31	0.08	0.19	0.19	0.16	0.25	0.42	0.13
	0.00	0.00	0.00	0.00	0.00	0.00	0.00	0.00	0.00	0.00	0.00	0.00	0.00	0.00	0.00
	0.65	0.74	0.72	0.70	0.67	0.75	0.82	0.78	0.87	0.81	0.79	0.80	0.79	0.73	0.82
	4.96	4.97	5.00	4.77	4.92	4.23	4.76	4.32	4.59	4.58	4.73	4.72	4.71	4.45	4.73
	2.23	1.35	8.21	3.91	2.74	1.77	2.33	3.16	3.33	1.63	1.89	1.77	2.20	2.27	2.74

Tab. 4) (continued)

	1Bis-1	1Bis-1	1Bis-1	1Bis-1	1Bis-1	1Bis-1	UA50-4-21	UA50-4-21	UA50-4-21	UA50-4-21	SEG6-4	SEG6-4
	PG-1	PG-1	PG-1	PG-1	PG-1	PG-1	PG-1	PG-1	PG-1	PG-1	PG-1	PG-1
SiO_2	49.15	53.40	52.96	52.20	47.60	47.78	50.91	50.29	46.60	51.39	46.24	49.36
TiO_2	0.54	0.22	0.39	0.34	0.13	bdl	0.78	0.16	1.33	0.68	1.17	1.19
Al_2O_3	8.07	4.98	4.55	4.66	8.55	10.48	7.25	1.82	9.28	6.67	7.70	7.55
FeO	9.90	7.80	7.62	7.77	7.55	7.75	8.41	18.04	10.17	8.25	16.75	16.89
MnO	0.03	0.19	0.03	0.10	0.19	0.18	0.09	0.12	0.09	bdl	0.35	0.35
MgO	15.30	18.80	18.71	18.33	16.32	16.24	16.99	18.21	15.13	17.83	11.61	12.94
CaO	12.56	12.68	12.75	12.68	11.64	12.01	12.65	9.87	12.31	12.66	12.00	11.90
Na_2O	0.95	0.83	0.74	0.71	1.31	1.58	1.06	0.27	1.35	0.86	1.03	0.87
K_2O	0.14	0.06	0.09	0.06	0.12	0.12	0.17	0.28	0.31	0.16	0.34	0.53
BaO	0.09	0.16	bdl	0.06	bdl	bdl	bdl	0.07	0.34	0.27	0.16	0.05
SrO	0.16	0.12	bdl	0.15	bdl	0.15	0.15	0.14	bdl	bdl	0.29	bdl
Cr_2O_3	0.07	0.20	0.04	0.28	bdl	bdl	0.35	0.12	0.20	bdl	bdl	0.17
NiO_2	0.12	0.13	bdl	bdl	0.03	bdl	0.07	0.37	0.11	0.21	0.15	0.17
ZrO_2	bdl	bdl	bdl	bdl	bdl	bdl	bdl	bdl	bdl	bdl	bdl	bdl
V_2O_3	bdl	bdl	bdl	0.07	bdl	0.12	0.08	0.13	0.18	0.11	0.30	0.15
F	bdl	bdl	bdl	0.20	bdl	bdl	0.18	bdl	bdl	0.15	bdl	bdl
Cl	0.07	bdl	0.05	0.04	bdl	0.05	bdl	0.07	bdl	0.04	0.03	0.12
S	bdl	0.10	bdl	bdl	bdl	0.04	bdl	bdl	bdl	bdl	0.05	bdl
P_2O_5	bdl	bdl	bdl	0.06	bdl	bdl	0.03	0.04	bdl	0.11	0.07	bdl
sum	97.16	99.67	97.93	97.71	93.43	96.51	99.18	99.98	97.41	99.39	98.22	102.26
Normalized at 23 oxygens												
Si	7.10	7.42	7.46	7.42	7.06	6.89	7.16	7.34	6.79	7.22	6.92	7.02
^{IV}Al	0.90	0.58	0.54	0.58	0.94	1.11	0.84	0.31	1.21	0.78	1.08	0.98
^{VI}Al	0.48	0.24	0.21	0.20	0.55	0.67	0.37	0.00	0.39	0.33	0.27	0.29
Ti	0.06	0.02	0.04	0.04	0.01	0.00	0.08	0.02	0.15	0.07	0.13	0.13
Cr	0.01	0.02	0.00	0.03	0.00	0.00	0.04	0.01	0.02	0.00	0.00	0.02
Fe^{3+}	0.00	0.03	0.04	0.10	0.00	0.00	0.00	1.23	0.05	0.03	0.25	0.12
Fe^{2+}	1.20	0.88	0.86	0.83	0.94	0.93	0.99	0.97	1.19	0.94	1.84	1.89
Mn	0.00	0.02	0.00	0.01	0.02	0.02	0.01	0.01	0.01	0.00	0.04	0.04
Mg	3.30	3.90	3.93	3.88	3.61	3.49	3.56	3.96	3.29	3.73	2.59	2.74
Ca	1.94	1.89	1.92	1.93	1.85	1.86	1.91	1.54	1.92	1.91	1.92	1.81
Na	0.27	0.22	0.20	0.20	0.38	0.44	0.29	0.08	0.38	0.23	0.30	0.24
K	0.03	0.01	0.02	0.01	0.02	0.02	0.03	0.05	0.06	0.03	0.06	0.10
Ba	0.01	0.01	0.00	0.00	0.00	0.00	0.00	0.00	0.02	0.01	0.01	0.00
Sr	0.01	0.01	0.00	0.01	0.00	0.01	0.01	0.01	0.00	0.00	0.03	0.00
Cr	0.01	0.02	0.00	0.03	0.00	0.00	0.04	0.01	0.02	0.00	0.00	0.02
Zr	0.00	0.00	0.00	0.00	0.00	0.00	0.00	0.00	0.00	0.00	0.00	0.00
F	0.00	0.00	0.00	0.01	0.00	0.00	0.01	0.00	0.00	0.01	0.00	0.00
Cl	0.00	0.00	0.00	0.00	0.00	0.00	0.00	0.00	0.00	0.00	0.00	0.00
S	0.00	0.00	0.00	0.00	0.00	0.00	0.00	0.00	0.00	0.00	0.00	0.00
OH	1.00	1.00	1.00	0.99	1.00	1.00	0.99	1.00	1.00	0.99	1.00	1.00
sum	16.30	16.27	16.23	16.27	16.38	16.45	16.33	16.56	16.50	16.29	16.46	16.40
^{B}(Ca+Na)	2.00	2.00	2.00	2.00	2.00	2.00	2.00	1.62	2.00	2.00	2.00	2.00
^{B}Ca	1.94	1.89	1.92	1.93	1.85	1.86	1.91	1.54	1.92	1.91	1.92	1.81
^{A}(Na+K)	0.25	0.13	0.14	0.15	0.25	0.33	0.24	0.05	0.36	0.17	0.31	0.15
^{A}Ca	0.00	0.00	0.00	0.00	0.00	0.00	0.00	0.00	0.00	0.00	0.00	0.00
Mg/(Mg+Fe^{2+}) = X_{Mg}	0.73	0.82	0.82	0.82	0.79	0.79	0.78	0.80	0.73	0.80	0.58	0.59
(Mg, Fe^{2+}, Mn, Li)	4.50	4.80	4.79	4.72	4.57	4.45	4.56	4.94	4.49	4.68	4.48	4.67
^{IV}Al/^{IV}Al	1.88	2.41	2.54	2.90	1.71	1.65	2.28	0.00	3.13	2.39	3.96	3.43

Tab. 4) (continued)

	SEG6-4	SEG6-4	SEG6-4	1Bis-1	UA50-3-5	UA50-3-5	3B-2	JH1-19	UA50-3-10	KG23c D8 13	KG23c-D8-13	KG23c D8 13	KG23c D8 13	KG23c D8 13	AAS1-203
	PG-1	PG-1	PG-1	PG-1	PG2	PG-2	PG-2	PG-2	SPG-1	SPG-2	SPG-2	SPG-2	SPG-2	SPG-2	PG-3
SiO_2	48.00	52.30	50.50	42.43	48.59	47.38	47.95	49.39	47.60	51.37	45.74	45.89	46.06	48.68	47.39
TiO_2	1.25	0.38	0.39	0.33	0.29	0.43	1.48	0.36	1.52	0.60	0.60	1.37	0.86	0.75	1.44
Al_2O_3	6.91	5.78	5.73	14.09	2.50	9.57	6.10	6.98	6.49	3.69	11.00	7.17	7.04	4.67	6.68
FeO	16.42	13.97	13.78	12.31	12.87	9.98	10.88	11.39	11.20	14.54	11.25	15.44	16.50	14.11	16.07
MnO	0.25	0.19	0.20	0.36	0.33	0.23	0.28	0.31	0.30	0.25	0.15	0.37	0.21	0.38	0.54
MgO	12.73	15.65	15.05	12.88	12.15	15.21	15.71	15.92	15.75	13.55	14.68	12.29	11.91	13.81	12.25
CaO	11.19	11.99	11.35	11.74	14.80	11.87	11.56	11.69	11.72	12.33	10.75	11.53	11.95	12.06	11.26
Na_2O	0.80	0.72	0.61	1.9	0.21	1.22	0.94	0.93	0.92	0.47	1.75	1.24	1.10	0.76	1.23
K_2O	0.59	0.29	0.19	bdl	0.12	0.27	0.71	0.31	0.65	0.26	0.26	0.79	0.80	0.51	0.60
BaO	bdl	bdl	bdl	bdl	bdl	0.05	bdl	0.09	0.04	0.17	0.11	bdl	0.05	bdl	0.25
SrO	0.07	0.11	0.05	bdl	0.05	0.12	bdl	0.24	0.09	0.27	0.18	0.03	0.19	0.10	0.12
Cr_2O_3	bdl	0.11	0.09	bdl	0.03	bdl	bdl	bdl	bdl	bdl	bdl	bdl	bdl	bdl	bdl
NiO_2	0.06	0.15	bdl	bdl	0.19	bdl	bdl	bdl	bdl	bdl	bdl	bdl	bdl	bdl	bdl
ZrO_2	bdl	bdl	bdl	0.16	bdl	0.10	bdl	bdl	bdl	bdl	bdl	bdl	bdl	bdl	bdl
V_2O_3	bdl	0.04	0.06	bdl	bdl	bdl	bdl	bdl	bdl	bdl	bdl	bdl	bdl	bdl	bdl
F	bdl	bdl	0.03	0.26	0.05	0.05	0.50	0.10	0.25	0.05	0.04	0.33	0.68	0.09	bdl
Cl	0.10	0.04	bdl	0.04	0.04	0.03	0.14	bdl	0.05	0.10	bdl	0.11	0.07	0.06	0.15
S	bdl	bdl	bdl	0.34	bdl	0.06	0.17	0.11	0.15	bdl	bdl	0.10	0.06	bdl	bdl
P_2O_5	bdl	bdl	bdl	bdl	bdl	bdl	bdl	bdl	bdl	bdl	bdl	bdl	bdl	bdl	bdl
sum	98.41	101.72	98.06	97.12	92.20	96.56	96.41	97.82	96.73	97.66	96.51	96.66	97.48	95.98	97.98
Si	7.07	7.31	7.31	6.30	7.58	6.91	7.10	7.15	7.02	7.54	6.71	6.94	6.96	7.29	7.04
^{IV}Al	0.93	0.69	0.69	1.70	0.42	1.09	0.90	0.85	0.98	0.46	1.29	1.06	1.04	0.71	0.96
^{VI}Al	0.27	0.27	0.29	0.77	0.04	0.55	0.16	0.34	0.15	0.17	0.61	0.21	0.22	0.12	0.22
Ti	0.14	0.04	0.04	0.04	0.03	0.05	0.16	0.04	0.17	0.07	0.07	0.16	0.10	0.08	0.16
Cr	0.00	0.01	0.01	0.00	0.00	0.00	0.00	0.00	0.00	0.00	0.00	0.00	0.00	0.00	0.00
Fe^{3+}	0.08	0.13	0.15	0.35	0.33	0.05	0.02	0.17	0.17	0.00	0.00	0.03	0.21	0.15	0.00
Fe^{2+}	1.95	1.51	1.52	1.18	1.35	1.16	1.33	1.21	1.22	1.78	1.38	1.92	1.88	1.62	2.00
Mn	0.03	0.02	0.02	0.05	0.04	0.03	0.03	0.04	0.04	0.03	0.02	0.05	0.03	0.05	0.07
Mg	2.79	3.26	3.25	2.85	2.83	3.30	3.47	3.43	3.46	2.96	3.21	2.77	2.68	3.08	2.71
Ca	1.77	1.80	1.76	1.87	2.47	1.85	1.83	1.81	1.85	1.94	1.69	1.87	1.94	1.94	1.79
Na	0.23	0.20	0.17	0.56	0.06	0.34	0.27	0.26	0.26	0.13	0.50	0.36	0.32	0.22	0.35
K	0.11	0.05	0.04	0.04	0.02	0.05	0.13	0.06	0.12	0.05	0.05	0.15	0.15	0.10	0.11
Ba	0.00	0.00	0.00	0.00	0.00	0.00	0.00	0.01	0.00	0.01	0.01	0.00	0.00	0.00	0.01
Sr	0.01	0.01	0.00	0.00	0.00	0.01	0.00	0.02	0.01	0.02	0.02	0.00	0.02	0.01	0.01
Cr	0.00	0.01	0.01	0.00	0.00	0.00	0.00	0.00	0.00	0.00	0.00	0.00	0.00	0.00	0.00
Zr	0.00	0.00	0.00	0.01	0.00	0.01	0.00	0.00	0.00	0.00	0.00	0.00	0.00	0.00	0.00
F	0.00	0.00	0.00	0.01	0.00	0.00	0.03	0.01	0.01	0.00	0.00	0.02	0.04	0.00	0.00
Cl	0.00	0.00	0.00	0.00	0.00	0.00	0.00	0.00	0.00	0.00	0.00	0.00	0.00	0.00	0.00
S	0.00	0.00	0.00	0.01	0.00	0.00	0.01	0.00	0.00	0.00	0.00	0.00	0.00	0.00	0.00
OH	1.00	1.00	1.00	0.97	1.00	0.99	0.96	0.99	0.98	0.99	1.00	0.98	0.96	0.99	1.00
sum	16.37	16.30	16.27	16.72	16.20	16.42	16.41	16.38	16.44	16.17	16.55	16.53	16.55	16.37	16.44
^{B}(Ca+Na)	1.99	1.99	1.93	2.00	2.00	2.00	2.00	2.00	2.00	2.00	2.00	2.00	2.00	2.00	2.00
^{B}Ca	1.77	1.80	1.76	1.87	2.00	1.85	1.83	1.81	1.85	1.94	1.69	1.87	1.94	1.94	1.79
^{A}(Na+K)	0.11	0.05	0.04	0.47	0.09	0.26	0.24	0.15	0.24	0.14	0.25	0.39	0.43	0.26	0.27
^{A}Ca	0.00	0.00	0.00	0.00	0.47	0.00	0.00	0.00	0.00	0.00	0.00	0.00	0.00	0.00	0.00
Mg/(Mg+Fe^{2+}) = X_{Mg}	0.59	0.68	0.68	0.71	0.68	0.74	0.72	0.74	0.74	0.62	0.70	0.59	0.59	0.66	0.58
(Mg, Fe^{2+}, Mn, Li)	4.77	4.79	4.79	4.08	4.22	4.50	4.83	4.68	4.71	4.78	4.61	4.74	4.59	4.75	4.78
^{IV}Al/^{IV}Al	3.51	2.59	2.38	2.21	9.95	2.00	5.64	2.55	6.72	2.68	2.11	4.94	4.71	5.93	4.44

Tab. 4) (continued)

	AAS1-203	1Bis-1	1Bis-1	1Bis-1	1Bis-1	1Bis-1	1Bis-1	1Bis-1	1Bis-1	1Bis-1	1Bis-1	1Bis-1
	PG-3	PG-1	PG-1	PG-1	PG-1	PG-1	PG-1	PG-1	PG-1	PG-1	PG-1	PG-1
SiO_2	45.90	41.49	40.22	42.15	41.49	41.28	40.63	41.26	41.61	41.78	41.73	41.86
TiO_2	0.12	1.37	0.79	0.52	0.37	0.25	0.04	0.65	1.86	2.33	2.29	2.53
Al_2O_3	12.41	13.95	16.15	16.66	14.74	15.58	16.00	13.64	13.52	13.28	13.04	12.90
FeO	8.49	10.82	11.46	10.14	11.23	11.29	11.25	11.93	10.18	10.05	10.05	10.00
MnO	0.26	0.26	0.43	0.50	0.28	0.17	0.29	0.26	0.07	0.14	0.11	0.27
MgO	14.96	12.05	12.07	12.81	12.64	11.99	11.94	12.40	13.57	13.46	13.61	13.50
CaO	11.81	11.80	11.78	11.82	11.87	11.61	11.60	11.89	12.10	12.10	12.16	12.11
Na_2O	1.88	2.19	2.05	2.44	2.03	2.00	2.41	2.08	2.18	2.20	2.27	2.28
K_2O	0.23	0.46	0.47	0.36	0.42	0.32	0.39	0.70	0.60	0.58	0.57	0.62
BaO	bdl	bdl	bdl	bdl	bdl	bdl	bdl	0.27	0.16	0.29	0.19	bdl
SrO	0.19	bdl	bdl	bdl	0.16	0.05	bdl	0.23	bdl	bdl	0.15	0.06
Cr_2O_3	bdl	bdl	bdl	bdl	0.04	bdl	bdl	0.09	0.32	0.28	0.13	0.25
NiO_2	0.04	bdl	bdl	bdl	0.05	0.03	bdl	bdl	bdl	bdl	0.06	0.17
ZrO_2	bdl	0.06	bdl	bdl	bdl	bdl	bdl	bdl	bdl	bdl	bdl	bdl
V_2O_3	bdl	bdl	bdl	bdl	bdl	bdl	0.05	0.13	0.15	0.12	0.41	0.20
F	0.06	bdl	bdl	bdl	bdl	0.21	bdl	bdl	0.14	bdl	bdl	bdl
Cl	0.06	0.16	0.14	0.18	0.12	bdl	0.08	0.10	0.05	bdl	0.06	0.07
S	0.04	0.04	0.12	0.23	0.09	bdl	bdl	0.05	bdl	0.09	bdl	bdl
P_2O_5	bdl	bdl	bdl	bdl	bdl	bdl	bdl	0.03	bdl	bdl	bdl	bdl
sum	96.47	94.62	95.70	97.81	95.52	94.82	94.68	95.71	96.53	96.70	96.83	96.82
Normalized at 23 oxygens												
Si	6.67	6.28	6.04	6.14	6.23	6.22	6.14	6.25	6.19	6.20	6.21	6.21
^{IV}Al	1.33	1.72	1.96	1.86	1.77	1.78	1.86	1.75	1.81	1.80	1.79	1.79
^{VI}Al	0.80	0.76	0.91	1.01	0.84	0.99	1.00	0.68	0.56	0.52	0.49	0.47
Ti	0.01	0.16	0.09	0.06	0.04	0.03	0.00	0.07	0.21	0.26	0.26	0.28
Cr	0.00	0.00	0.00	0.00	0.00	0.00	0.00	0.01	0.04	0.03	0.02	0.03
Fe^{3+}	0.00	0.00	0.28	0.00	0.26	0.12	0.10	0.20	0.06	0.00	0.00	0.00
Fe^{2+}	1.03	1.37	1.16	1.24	1.15	1.30	1.32	1.32	1.21	1.25	1.25	1.24
Mn	0.03	0.03	0.06	0.06	0.04	0.02	0.04	0.03	0.01	0.02	0.01	0.03
Mg	3.24	2.72	2.70	2.78	2.83	2.69	2.69	2.80	3.01	2.98	3.02	2.99
Ca	1.84	1.91	1.90	1.85	1.91	1.88	1.88	1.93	1.93	1.92	1.94	1.93
Na	0.53	0.64	0.60	0.69	0.59	0.58	0.71	0.61	0.63	0.63	0.65	0.66
K	0.04	0.09	0.09	0.07	0.08	0.06	0.08	0.14	0.11	0.11	0.11	0.12
Ba	0.00	0.00	0.00	0.00	0.00	0.00	0.00	0.02	0.01	0.02	0.01	0.00
Sr	0.02	0.00	0.00	0.00	0.01	0.00	0.00	0.02	0.00	0.00	0.01	0.01
Cr	0.00	0.00	0.00	0.00	0.00	0.00	0.00	0.01	0.04	0.03	0.02	0.03
Zr	0.00	0.00	0.00	0.00	0.00	0.00	0.00	0.00	0.00	0.00	0.00	0.00
F	0.00	0.00	0.00	0.00	0.00	0.01	0.00	0.00	0.01	0.00	0.00	0.00
Cl	0.00	0.00	0.00	0.01	0.00	0.00	0.00	0.00	0.00	0.00	0.00	0.00
S	0.00	0.00	0.00	0.01	0.00	0.00	0.00	0.00	0.00	0.00	0.00	0.00
OH	0.99	0.99	0.99	0.99	0.99	0.99	1.00	1.00	0.99	1.00	1.00	1.00
sum	16.54	16.69	16.78	16.75	16.76	16.69	16.82	16.84	16.81	16.77	16.78	16.78
$^{B}(Ca+Na)$	2.00	2.00	2.00	2.00	2.00	2.00	2.00	2.00	2.00	2.00	2.00	2.00
^{B}Ca	1.84	1.91	1.90	1.85	1.91	1.88	1.88	1.93	1.93	1.92	1.94	1.93
$^{A}(Na+K)$	0.43	0.64	0.59	0.60	0.60	0.53	0.66	0.70	0.67	0.67	0.71	0.70
^{A}Ca	0.00	0.00	0.00	0.00	0.00	0.00	0.00	0.00	0.00	0.00	0.00	0.00
$Mg/(Mg+Fe^{2+}) = X_{Mg}$	0.76	0.67	0.70	0.69	0.71	0.67	0.67	0.68	0.71	0.70	0.71	0.71
(Mg, Fe^{2+}, Mn, Li)	4.30	4.12	3.92	4.08	4.02	4.02	4.05	4.15	4.23	4.24	4.28	4.26
$^{IV}Al/^{IV}Al$	1.67	2.26	2.16	1.84	2.11	1.79	1.86	2.56	3.24	3.47	3.65	3.81

Tab. 4) (continued)

	1Bis-1	1Bis-1	1Bis-1	UA 50 4 21	UA 50 4 21	UA 50 4 21	JH1 19	JH1 19	JH1 19	AAS1-203	UA50-3-10	KG23c C2 26	KG23c C2 26	UA50-4-21	UA50-4-21
	PG-1	PG-1	PG-1	PG-1	PG-1	PG-1	PG-2	PG-2	PG-2	PG-3	SPG-1	SPG-2	SPG-2	PG-1	PG-1
	42.89	40.84	40.65	39.20	39.39	44.56	41.52	41.99	41.38	41.50	41.20	39.23	41.78	56.76	51.54
	0.14	0.09	0.09	3.82	4.07	2.80	2.07	1.80	2.31	2.36	2.25	2.58	1.20	0.28	0.23
	17.45	18.18	18.56	13.27	12.88	12.62	11.91	10.13	11.52	10.59	11.73	11.74	10.00	3.62	17.10
	11.40	10.42	10.26	12.25	12.25	9.91	16.92	15.34	14.75	14.80	15.90	20.80	20.26	10.25	10.67
	0.19	0.23	0.17	0.27	0.17	0.19	0.27	0.36	0.11	0.29	0.19	0.49	0.31	0.15	0.26
	12.91	11.96	11.94	13.29	12.44	14.51	10.13	11.42	11.32	11.51	10.50	7.41	7.85	22.08	10.73
	11.13	11.60	11.90	11.34	11.89	12.44	11.31	11.30	11.39	11.19	11.32	11.34	11.24	0.82	2.28
	2.65	2.65	2.31	3.04	2.38	2.10	2.03	1.60	1.84	1.74	1.80	1.52	1.48	0.22	0.23
	0.36	0.33	0.34	1.16	0.90	0.35	0.58	1.39	1.50	1.51	1.04	1.63	1.39	0.37	0.95
	bdl	bdl	0.13	bdl	bdl	0.05	bdl	0.16	bdl	0.43	bdl	0.13	0.04	0.05	bdl
	bdl	0.08	0.16	bdl	0.19	bdl	bdl	0.17	0.13	0.18	0.07	0.26	0.10	bdl	bdl
	0.07	bdl	0.07	bdl	bdl	0.74	bdl	bdl	bdl	bdl	bdl	bdl	bdl	bdl	bdl
	0.22	0.05	bdl	bdl	0.07	0.21	bdl	bdl	bdl	bdl	bdl	bdl	bdl	bdl	bdl
	bdl	bdl	bdl	0.33	bdl	bdl	bdl	bdl	bdl	bdl	bdl	bdl	bdl	bdl	bdl
	bdl	0.05	bdl	bdl	bdl	0.08	bdl	bdl	bdl	bdl	bdl	bdl	bdl	bdl	bdl
	0.11	bdl	0.10	bdl	0.04	bdl	0.11	0.22	0.47	0.18	0.29	0.22	0.19	bdl	0.09
	0.09	0.15	0.18	bdl	bdl	bdl	bdl	0.10	0.14	0.08	0.08	0.04	0.04	0.13	bdl
	bdl	0.11	bdl	0.05	0.15	bdl	bdl	0.09	0.09	0.08	0.05	bdl	0.09	bdl	0.03
	0.05	0.08	0.08	bdl	bdl	bdl	bdl	bdl	bdl	bdl	bdl	bdl	bdl	bdl	bdl
	99.66	96.82	96.96	98.01	96.82	100.55	96.86	96.07	96.95	96.44	96.91	97.39	95.97	94.73	94.13
	6.14	6.02	5.99	5.85	5.95	6.32	6.32	6.46	6.31	6.36	6.31	6.15	6.56	7.99	7.31
	1.86	1.98	2.01	2.15	2.05	1.68	1.68	1.54	1.69	1.64	1.69	1.85	1.44	0.01	0.69
	1.09	1.18	1.21	0.19	0.24	0.43	0.45	0.30	0.38	0.28	0.43	0.31	0.42	0.60	2.17
	0.02	0.01	0.01	0.43	0.46	0.30	0.24	0.21	0.26	0.27	0.26	0.30	0.14	0.03	0.02
	0.01	0.00	0.01	0.00	0.00	0.08	0.00	0.00	0.00	0.00	0.00	0.00	0.00	0.00	0.00
	0.00	0.00	0.06	0.00	0.03	0.00	0.06	0.08	0.00	0.00	0.02	0.20	0.00	0.00	0.00
	1.37	1.29	1.20	1.53	1.52	1.18	2.09	1.89	1.88	1.90	2.02	2.53	2.66	1.21	1.27
	0.02	0.03	0.02	0.03	0.02	0.02	0.03	0.05	0.01	0.04	0.02	0.07	0.04	0.02	0.03
	2.76	2.63	2.62	2.96	2.80	3.07	2.30	2.62	2.57	2.63	2.40	1.73	1.84	4.64	2.27
	1.71	1.83	1.88	1.81	1.92	1.89	1.84	1.86	1.86	1.84	1.86	1.90	1.89	0.12	0.35
	0.74	0.76	0.66	0.88	0.70	0.58	0.60	0.48	0.54	0.52	0.53	0.46	0.45	0.06	0.06
	0.07	0.06	0.06	0.22	0.17	0.06	0.11	0.27	0.29	0.30	0.20	0.33	0.28	0.07	0.17
	0.00	0.00	0.01	0.00	0.00	0.00	0.00	0.01	0.00	0.03	0.00	0.01	0.00	0.00	0.00
	0.00	0.01	0.01	0.00	0.02	0.00	0.00	0.02	0.01	0.02	0.01	0.02	0.01	0.00	0.00
	0.01	0.00	0.01	0.00	0.00	0.08	0.00	0.00	0.00	0.00	0.00	0.00	0.00	0.00	0.00
	0.00	0.00	0.00	0.03	0.00	0.00	0.00	0.00	0.00	0.00	0.00	0.00	0.00	0.00	0.00
	0.01	0.00	0.01	0.00	0.00	0.00	0.01	0.01	0.02	0.01	0.02	0.01	0.01	0.00	0.00
	0.00	0.00	0.01	0.00	0.00	0.00	0.00	0.00	0.00	0.00	0.00	0.00	0.00	0.00	0.00
	0.00	0.00	0.00	0.00	0.00	0.00	0.00	0.00	0.00	0.00	0.00	0.00	0.00	0.00	0.00
	0.99	0.99	0.99	1.00	0.99	1.00	0.99	0.98	0.97	0.99	0.98	0.99	0.99	1.00	0.99
	16.77	16.80	16.76	17.08	16.88	16.69	16.73	16.79	16.81	16.81	16.74	16.86	16.73	15.74	15.35
	2.00	2.00	2.00	2.00	2.00	2.00	2.00	2.00	2.00	2.00	2.00	2.00	2.00	0.18	0.41
	1.71	1.83	1.88	1.81	1.92	1.89	1.84	1.86	1.86	1.84	1.86	1.90	1.89	0.12	0.35
	0.51	0.66	0.61	0.91	0.81	0.53	0.56	0.63	0.71	0.67	0.60	0.71	0.63	0.07	0.17
	0.00	0.00	0.00	0.00	0.00	0.00	0.00	0.00	0.00	0.00	0.00	0.00	0.00	0.00	0.00
	0.67	0.67	0.69	0.66	0.65	0.72	0.52	0.58	0.58	0.58	0.54	0.41	0.41	0.79	0.64
	4.14	3.94	3.84	4.52	4.34	4.27	4.42	4.56	4.47	4.57	4.44	4.32	4.54	5.86	3.57
	1.71	1.67	1.67	11.60	8.59	3.94	3.70	5.15	4.52	5.86	3.98	5.92	3.45	0.01	0.32

Tab. 4) (continued)

	SEG6-4	SEG6-4	SEG6-4	SEG6-4	SEG6-4	SEG6-4	SEG6-4	SEG6-4	SEG6-4	SEG6-4	SEG6-4	SEG6-4
	PG-1	PG-1	PG-1	PG-1	PG-1	PG-1	PG-1	PG-1	PG-1	PG-1	PG-1	PG-1
SiO_2	53.51	52.79	54.94	53.88	54.65	51.46	51.85	51.47	53.35	54.14	53.70	54.35
TiO_2	0.34	bdl	0.06	0.15	bdl	0.26	0.29	0.25	bdl	bdl	bdl	bdl
Al_2O_3	1.35	0.80	0.69	0.72	0.93	1.02	0.99	1.29	0.95	0.67	0.58	1.76
FeO	22.08	22.88	23.22	23.04	23.05	26.54	25.39	25.57	22.76	23.24	23.38	21.58
MnO	0.59	0.78	0.89	0.80	0.51	0.76	0.69	0.72	0.80	0.79	0.80	0.56
MgO	16.39	16.61	18.00	17.71	18.01	18.47	18.69	18.95	17.21	17.44	17.14	17.31
CaO	3.42	1.62	0.89	1.10	1.67	1.78	2.21	1.87	1.97	1.33	1.17	1.15
Na_2O	0.20	0.16	0.12	0.09	0.14	0.12	0.12	0.06	0.19	0.09	0.09	0.03
K_2O	0.04	bdl	bdl	bdl	bdl	bdl	bdl	bdl	0.06	0.08	bdl	0.07
BaO	bdl	bdl	bdl	bdl	0.14	0.07	bdl	0.03	bdl	0.12	bdl	bdl
SrO	bdl	0.21	bdl	0.18	0.10	0.29	0.16	0.14	0.29	0.11	0.28	0.11
Cr_2O_3	0.05	bdl	bdl	0.07	0.06	bdl	bdl	0.09	bdl	0.06	bdl	bdl
NiO_2	0.04	bdl	0.11	bdl	bdl	0.13	0.03	bdl	0.17	bdl	bdl	0.08
ZrO_2	bdl	bdl	bdl	bdl	bdl	bdl	bdl	bdl	bdl	bdl	bdl	bdl
V_2O_3	bdl	0.14	bdl	bdl	0.04	0.07	bdl	0.07	bdl	bdl	bdl	0.03
F	bdl	bdl	bdl	bdl	bdl	bdl	bdl	bdl	bdl	bdl	bdl	bdl
Cl	0.04	bdl	bdl	bdl	bdl	bdl	bdl	bdl	bdl	bdl	bdl	0.04
S	0.08	0.06	bdl	bdl	0.05	bdl	0.08	0.10	bdl	bdl	bdl	bdl
P_2O_5	bdl	0.03	bdl	0.06	bdl	0.17	0.10	bdl	0.14	bdl	bdl	bdl
sum	98.14	96.07	98.94	97.80	99.38	101.13	100.60	100.62	97.89	98.06	97.14	97.10
Normalized at 23 oxygens												
Si	7.83	7.91	7.93	7.89	7.87	7.50	7.54	7.49	7.85	7.92	7.93	7.93
^{IV}Al	0.17	0.09	0.07	0.11	0.13	0.18	0.17	0.22	0.15	0.08	0.07	0.07
^{VI}Al	0.06	0.05	0.05	0.01	0.03	0.00	0.00	0.00	0.02	0.03	0.03	0.24
Ti	0.04	0.00	0.01	0.02	0.00	0.03	0.03	0.03	0.00	0.00	0.00	0.00
Cr	0.01	0.00	0.00	0.01	0.01	0.00	0.00	0.01	0.00	0.01	0.00	0.00
Fe^{3+}	0.00	0.00	0.00	0.04	0.04	1.07	0.98	1.07	0.10	0.00	0.01	0.00
Fe^{2+}	2.70	2.87	2.80	2.78	2.74	2.17	2.11	2.04	2.70	2.84	2.87	2.63
Mn	0.07	0.10	0.11	0.10	0.06	0.09	0.08	0.09	0.10	0.10	0.10	0.07
Mg	3.57	3.71	3.87	3.87	3.87	4.02	4.05	4.11	3.78	3.80	3.77	3.77
Ca	0.54	0.26	0.14	0.17	0.26	0.28	0.34	0.29	0.31	0.21	0.19	0.18
Na	0.06	0.05	0.03	0.03	0.04	0.03	0.03	0.02	0.05	0.03	0.03	0.01
K	0.01	0.00	0.00	0.00	0.00	0.00	0.00	0.00	0.01	0.01	0.00	0.01
Ba	0.00	0.00	0.00	0.00	0.01	0.00	0.00	0.00	0.00	0.01	0.00	0.00
Sr	0.00	0.02	0.00	0.02	0.01	0.02	0.01	0.01	0.02	0.01	0.02	0.01
Cr	0.01	0.00	0.00	0.01	0.01	0.00	0.00	0.01	0.00	0.01	0.00	0.00
Zr	0.00	0.00	0.00	0.00	0.00	0.00	0.00	0.00	0.00	0.00	0.00	0.00
F	0.00	0.00	0.00	0.00	0.00	0.00	0.00	0.00	0.00	0.00	0.00	0.00
Cl	0.00	0.00	0.00	0.00	0.00	0.00	0.00	0.00	0.00	0.00	0.00	0.00
S	0.00	0.00	0.00	0.00	0.00	0.00	0.00	0.00	0.00	0.00	0.00	0.00
OH	1.00	1.00	1.00	1.00	1.00	1.00	1.00	1.00	1.00	1.00	1.00	1.00
sum	16.06	16.05	16.02	16.05	16.07	16.40	16.36	16.39	16.10	16.05	16.03	15.92
^{B}(Ca+Na)	0.59	0.31	0.17	0.20	0.30	0.31	0.38	0.31	0.36	0.23	0.21	0.19
^{B}Ca	0.54	0.26	0.14	0.17	0.26	0.28	0.34	0.29	0.31	0.21	0.19	0.18
^{A}(Na+K)	0.01	0.00	0.00	0.00	0.00	0.00	0.00	0.00	0.01	0.01	0.00	0.01
^{A}Ca	0.00	0.00	0.00	0.00	0.00	0.00	0.00	0.00	0.00	0.00	0.00	0.00
$Mg/(Mg+Fe^{2+}) = X_{Mg}$	0.57	0.56	0.58	0.58	0.59	0.65	0.66	0.67	0.58	0.57	0.57	0.59
(Mg, Fe^{2+}, Mn, Li)	6.35	6.67	6.79	6.74	6.67	6.28	6.25	6.24	6.58	6.74	6.75	6.47
$^{IV}Al/^{IV}Al$	2.96	1.95	1.31	7.55	3.87	0.00	0.00	0.00	8.16	2.73	2.06	0.28

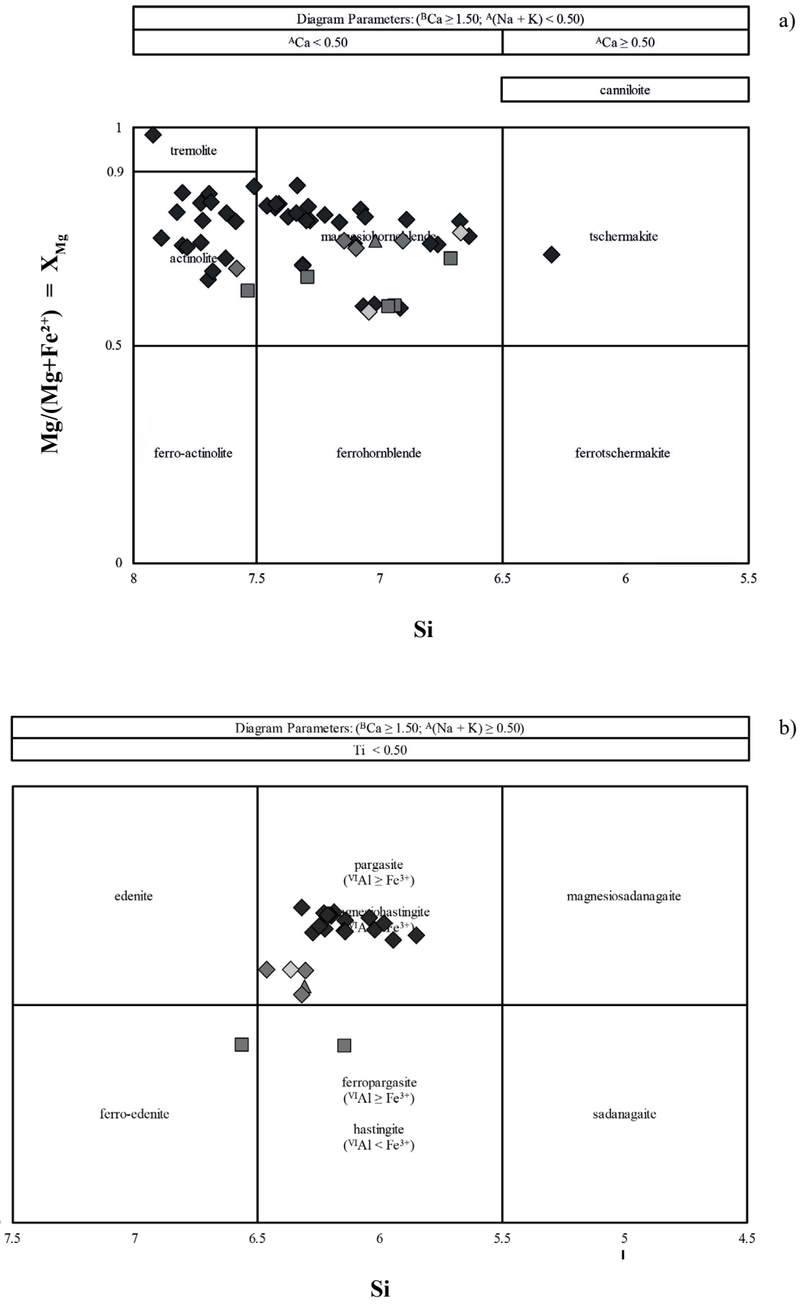

Fig. 11) Classification diagrams Si (in apfu) versus $Mg/(Mg+Fe^{2+}) = X_{Mg}$ of the Ca-amphiboles: a) and b). Black rhombus, PT-Dioritic Gnesiss Inclusion; dark grey rhombus, PT-Granodioritic Gnesiss Inclusions; light grey rhombus, PT-Granitic Gnesiss Inclusions; dark grey square, PT-Granodioritic Gnesiss + Basalt Inclusions; dark grey triangle, PT-Granodioritic Gnesiss + Limestone Inclusions; highlighted marker, CG-1.

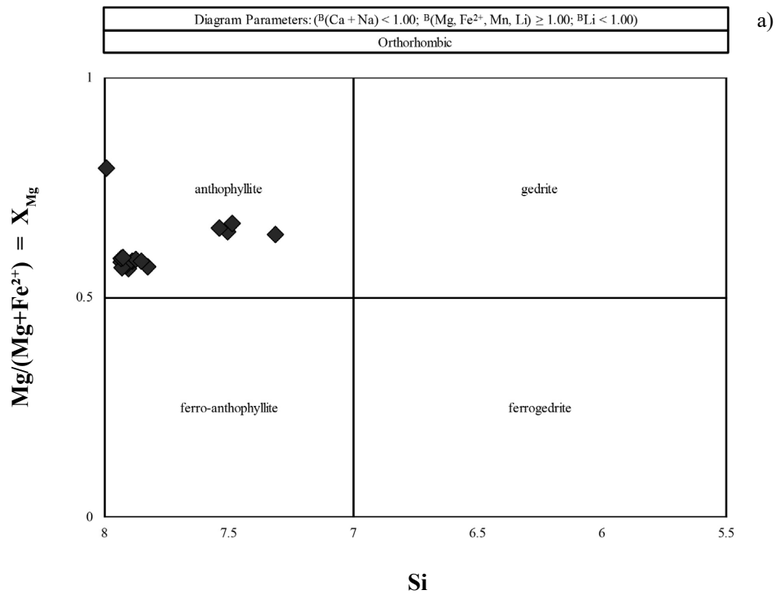

a)

Fig. 12) Classification diagrams Si (in apfu) versus $Mg/(Mg+Fe^{2+}) = X_M$ of the (Mg, Fe^{2+}, Mn, Li)-amphiboles. Black rhombus, PT-Dioritic Gnesiss Inclusion; dark grey rhombus, PT-Granodioritic Gnesiss Inclusions; light grey rhombus, PT-Granitic Gnesiss Inclusions; white rhombus, PT-Tonalitic Gnesiss Inclusions; dark grey square, PT-Granodioritic Gnesiss + Basalt Inclusions; dark grey triangle, PT-Granodioritic Gnesiss + Limestone Inclusions; highlighted marker, CG-1.

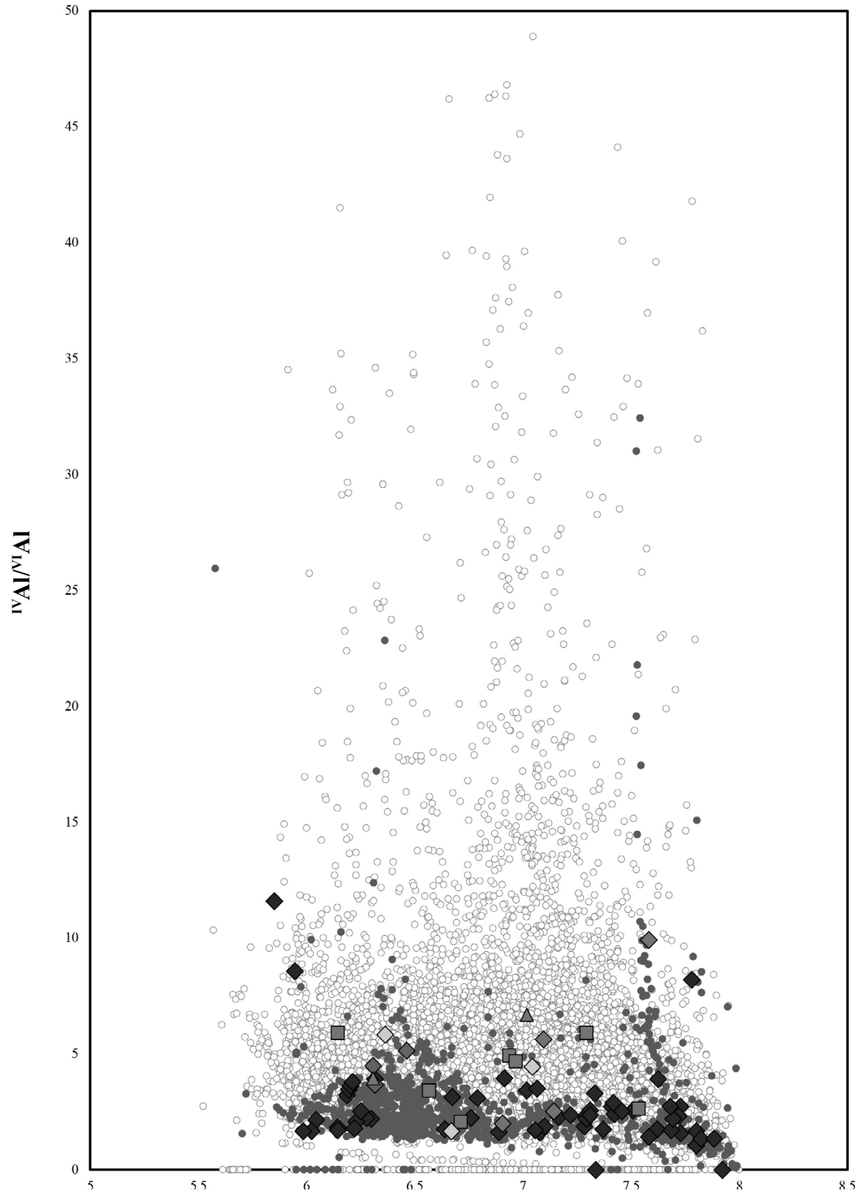

Fig. 13) Binary diagram Si (in apfu) versus $^{IV}Al/^{VI}Al$ in anphibole. Black rhombus, PT-Dioritic Gnesiss Inclusion; dark grey rhombus, PT-Granodioritic Gnesiss Inclusions; light grey rhombus, PT-Granitic Gnesiss Inclusions; dark grey square, PT-Granodioritic Gnesiss + Basalt Inclusions; dark grey triangle, PT-Granodioritic Gnesiss + Limestone Inclusions; white circles, Igneous amphibole; dark gray circles, Metamorphic amphibole. The eds data of the last two diagram elements come from the GEOROC database.

PG - Granodioritic Gneiss Inclusions (PT-2)

The petrographic group under analysis turns out to be the most widespread in the different ceramic productions; indeed, most of the ceramic samples from different archaeological sites fall under it.

The inclusions have an amount that fluctuates around an average of 45.07 %, however, in some samples it decreases sharply to average values around 24.41 % (1C-1, 3A-1, 3Bis-1 and 3D-1) (Tab. 2). The shape of the inclusions is both elongated and equidimensional, and they show a variable degree of rounding from angular to sub-rounded. Whereas their spatial distribution is between the two limits close-spaced and single-spaced, tending to the open-spaced limit only in samples characterized by the previously mentioned decrease of inclusions amount (Quinn, 2022).

There are two size families in this petrographic group, the largest falling in the coarse silt (4-5 Φ) with a mean average size of 4.87 Φ and the second lying in the middle silt (5-6 Φ) with a respective mean average size of 5.02 Φ (AAS1-174, 1E-1, 3-1, 3A-2, JAG-1928, KG23c-C2-13 and 3A-1) (Tab. 2). The size distribution is described by a type of sorting very well-sorted with mean value of 0.02 and type of skewness nearly symmetrical for samples 3-1, 3A-2, KG-23-A1-2 and KG23c-C3-3 (-0.08, -0.08 and -0.07) and coarse skewness, with mean value of -0.14, for the others (Folk, 1974; Folk and Ward, 1957; Friedmann, 1961) (Fig. 3; Tab. 2).

The porosity consists of vugh (micro-meso, occasionally mega) and planar voids (micro-meso, occasionally mega) and its amount, with an average value of 19.14 %, increases significantly in samples 1D-1, 3Bis-1, 3A-1, 3D-1, JAG-1928 (24. 62 %, 25.11 %, 28.94 % , 29.30 %, 29.67 %) (Tab. 2). I In addition, a significant amount of porosity resulting from the combustion of plant material was observed in sample 3A-2 (20.13%) (Quinn, 2022).

The clay matrix has an average value of 34.84 % from which the values of samples 5-1, 3-1, KG23c-C3-3 and 3A-2 diverge by increase (47.08 %, 52.20 %, 57.07 % and 57.74 %) (Tab. 2).

Generally, activity appears from medium to active going from the core towards the margins. However, the lowering of activity in the core can also affect the margins. The colour manifests itself by proceeding in the same direction from brown to reddish brown or light brown to orangey brown in both cross-polarised and parallel-polarised light. The colour inhomogeneity is not clear, but rather shaded, sometimes almost imperceptible, but with a tendency in some samples to be more defined.

However, there are samples (1A-1, 1D-1, 1E-1, 3-1, 3B-2, 3Bis-1, 5-1, 6-2, AAS1-112, JH1-11, JH1-18, JH1-19, JAG-1928, KG23c-C2-12, UA50-3-10) in which the activity and colouration together with the characteristics of colour inhomogeneity are different. In fact, the body is inactive with much more defined inhomogeneity ranging from grey to orange-red from the core to the margins.

The mineralogical phases both loose and aggregated in the lithics, which modes are expressed in Tab. 2, and the structures recognized in the latter can be traced to a granodioritic gneiss.

It should be noted that in samples UA50-2-2, UA50-2-4, UA50-3-5, UA50-4-26, UA50-2-1, UA50-2-3, UA50-3-6 and UA50-3-11 the decrease in the amount of amphiboles and pyroxenes is less pronounced, almost reminiscent of a granodioritic mineralogical assemblage tending towards monzodioritic (Tab.2).
However, although the occurrences of amphiboles, pyroxenes and epidote decrease significantly in relation to those of the previous petrographic group, the observations concerning these mineralogical phases are still equivalent.

In lithics, with an abundance of ~10-20% (Terry and Chilingar, 1955), granoblastic and recrystallized quartz structures with irregular edges formed due to bulging caused by grain edge migration are readable (Spray, 1969; Winter, J.D., 2001). Occasionally within quartz crystals in lithics there is an onset of dislocation migration that divides the grain into two undeformed subgrains whose edges appear less pronounced in thin section (Spray, 1969; Winter, J.D., 2001). Furthermore, in lithics, mineralogical phases with a more developed axis may be isoriented (Spray, 1969; Winter, J.D., 2001). Among the structures within individual mineralogical phases, we find in the plagioclase deformed albite gemination coupled partially with that of the pericline, whereas the microcline may exhibit deformed and/or incomplete gridiron gemination and portions replaced by orthoclase. However, there also exists the occasion where orthoclase is the host phase of the microcline (Spray, 1969; Winter, J.D., 2001).

SPG - Granodioritic gneiss + limestone inclusion (SPG-1)

Only three samples belong to this sub-petrographic group: UA50-3-10, UA50-4-19 and UA50-4-25.

The inclusions (60.08 %, 50.76% and 56.43%; UA50-3-10, UA50-4-19 and UA50-4-25) (Tab. 2) are both elongated and equidimensional in shape and have a higher degree of rounding that varies from sub-angular to rounded, minor angular (Quinn, 2022).

They show a spatial distribution between the two limits close-spaced and single-spaced (Quinn, 2022), mean average size of 4.87 Φ and a size distribution described by a type of sorting like very well-sorted (0.01, 0.03 and 0.02; UA 50 3 10, UA 50 4 19 and UA 50 4 25) and a type of skewness coarse skewed (-0.15, -0.13 and -0.15; UA50-3-10, UA50-4-19 and UA50-4-25) (Folk, 1974; Folk and Ward, 1957; Friedmann, 1961) (Fig.3, Tab. 2)
The porosity (19,89 %, 14,29% and 19,12 %; UA 50 3 10, UA 50 4 19 and UA 50 4 25) (Tab. 2) consist mainly of planar voids (micro-meso, secondarily mega) respect to vughs (micro-meso, secondarily mega) (Quinn, 2022).

The clay matrix (20.03 %, 34.94 % and 24.46 %; UA50-3-10, UA50-4-19 and UA50-4-25) (Tab. 2) has an optical activity that varies, moving from the core to the margins, from inactive to active. Only in sample UA50-3-10 the core, although moderately active, also shows strong activity (Quinn, 2022).

In terms of colouration, both in plane polarized light and crossed polars, samples UA50-4-19 and UA50-4-25 are black-brown in the core and red-brown along the margins, whereas sample UA50-3-10 is brown in the core and red-brown along the margins. Inhomogeneities in the colouration are blurred (Quinn, 2022).

With the addition of limestone lithics (4.58 %, 9.86 % and 4.51 %; UA50-3-10, UA50-4-19 and UA50-4-25) (Tab. 2) (Fig. 15, a-b), which characterize this petrographic group, all the features described for the granodioritic gneiss inclusion petrographic group occur.

SPG - Granodioritic gneiss + basalt inclusion (SPG-2)

This petrographic group includes three samples: KG23c-C2-26, KG23-D3-17, and KG23-D8-13. Moreover, sample KG23-D3-17, which was not subjected to QEM-SCAN analysis, has similar characteristics to sample KG23-D8-13.

The inclusions have an amount around ~ 45-50 % for all samples (48,66% and 46,75%; KG23c-C2-26 and KG23-D8-13), both elongated and equidimensional shape and a degree of rounding varying from angular to rounded (Tab. 2) (Terry and Chilingar, 1955; Quinn, 2022).

They show have a spatial distribution between the two limits close-spaced and single-spaced (Quinn, 2022), average size of 5.03 Φ (KG23c-C2-26) and 4.96 Φ (KG23-D8-13) and a size distribution described by a type of sorting very well-sorted with mean values of 0 (-0.01 and 0.01; KG23c-C2-26 and KG23-D8-13) and a type of skewness coarse skewed with mean values of -0.15 (-0.17 and -0.14; KG23c-C2-26 and KG23-D8-13) (Folk, 1974; Folk and Ward, 1957; Friedmann, 1961) (Fig. 3; Tab, 2).

The porosity, with abundance around ~ 15-20 % (20.70 % and 18.46 %; KG23c-C2-26 and KG23-D8-13), consists mainly of planar voids (micro-meso) and secondary to vughs (micro-meso, subordinately mega) (Tab. 2) (Terry and Chilingar, 1955; Quinn, 2022).

The clay matrix has an abundance around ~30-35 % (30.58 % and 34.74 %; KG23c-C2-26 and KG23-D8-13) (Tab. 2) (Terry and Chilingar, 1955; Quinn, 2022). The KG23-C2-26 and KG-D3-17 samples show inactive matrix while KG23-D3-13 sample active one. All samples can be have matrix portion whit moderate optical activity.

In terms of colouration, the matrix results entirely red-brown both in plane polarized light and crossed polars for all samples (Quinn, 2022).

With the addition of inclusions, lithics and loose mineralogical phase, derive from-disintegration of basalt (Tab. 2), which characterize this petrographic group, all the features described for the granodioritic gneiss inclusion petrographic group occur.

It is possible to distinguish two types of basalt lithics (~10-15%) (Terry and Chilingar, 1955), the first is characterized by a mineralogical assemblage consisting of pyroxene and plagioclase, the latter included in pyroxene according to a ophitic structure (Fig. 15, c-d). The second type of lithics, on the other hand, is being characterized by a porphyritic, hypocrystalline and intersertal structure, has a mineralogical assemblage consisting of plagioclase, pyroxene, olivine, which often has indigsitic edges, and magnetite (Fig. 15, e-f). The mineralogical assemblage is evaluated on background paste fragments of basalt, in fact on a few occasions phenocrysts can be observed; mainly pyroxenes and feldspars (Fig. 15, e-f). Most of the pyroxenes that were phenocrysts in the basalt are part of the loose fraction, evidence of which is the large size of these inclusions. The chemistry of pyroxenes derived from the disintegration of basalts shows high values in the $^{4}Al/^{6}Al$ ratio (Fig.7; Tab.3) ((Deer, Howie and Zussman, 1997a)

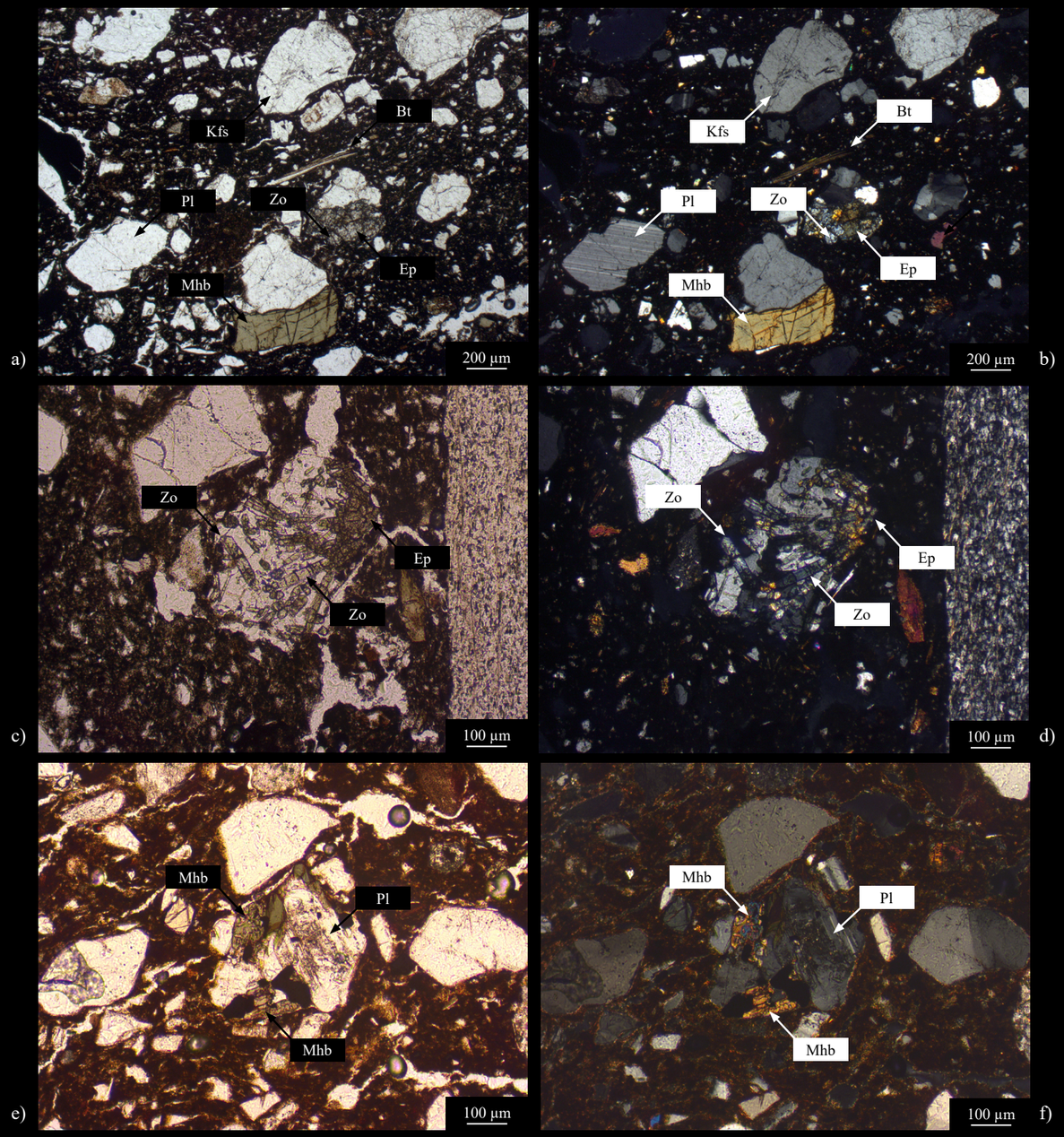

Fig. 14) 1A-1; Lithics and loose mineralogical phases resulting from the disintegration of granodioritic gneiss: a) and b), respectively plane polarized light and crossed polar view microphotographs. 3B-2; Granodioritic geniss lithic consisting of zoisite, epidote, and quartz arranged in an irregular granoblastic structure: c) and d), respectively plane polarized light and crossed polar view microphotographs. KG23c-D3-13; Granodioritic lithic geniss consisting of magnesiohornblende, plagioclase and quartz arranged in an irregular granoblastic structure Mineral abbreviation (Whitney and Evans, 2010): Bt, biotite; Ep, epidote; Kfs, K-feldspar; Mhb, magnesiohornblende; Pl, plagioclase; Zo, zoisite.

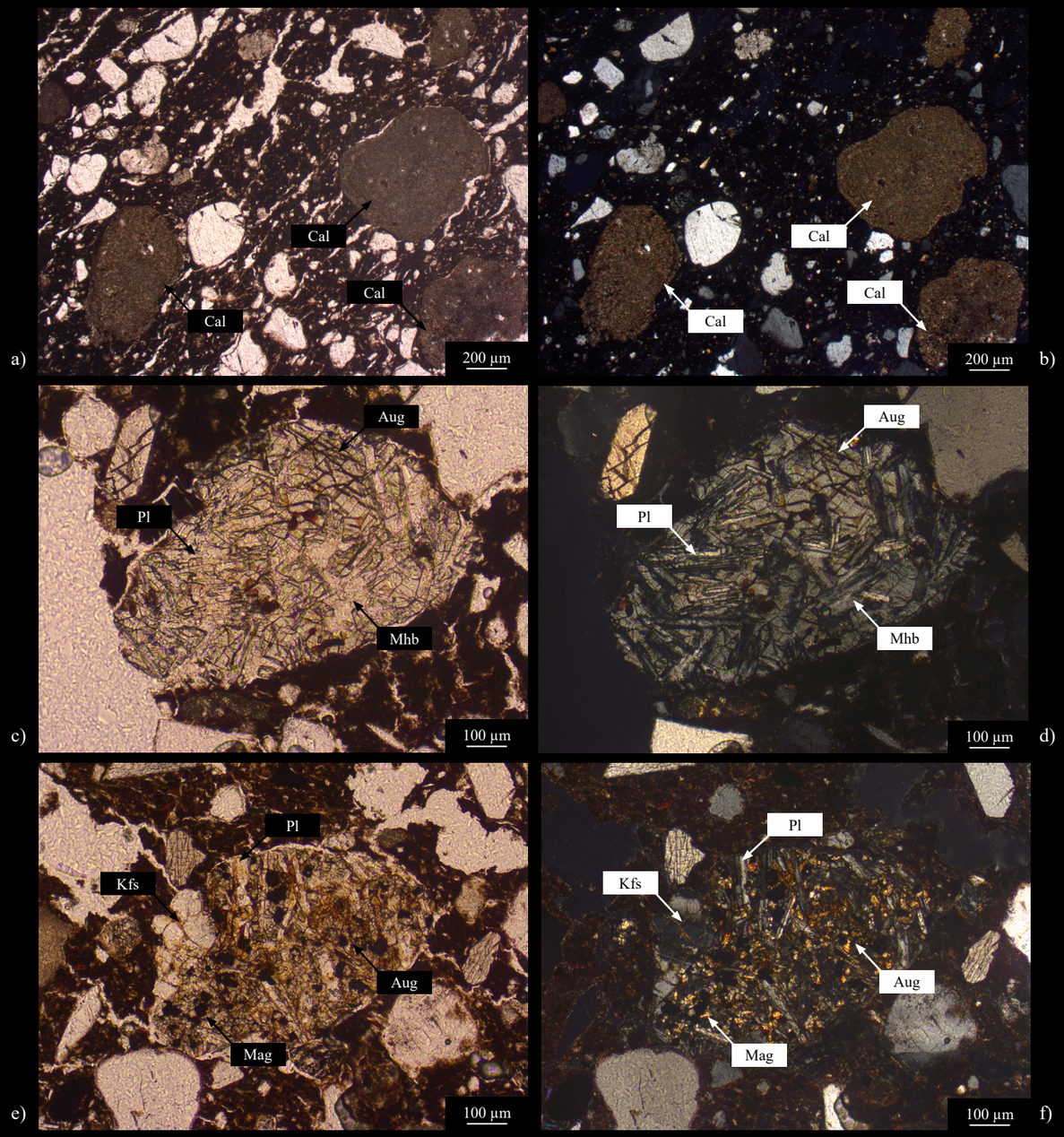

Fig. 15) UA50-4-19; Limestone lithics in addition to lithics and loose mineralogical phases resulting from the disaggregation of granodioritic gneiss: a) and b), respectively plane polarized light and crossed polar view microphotographs. KG23c-D3-17; Basalt lithic exhibiting ophitic structure consisting of plagioclase crystals immersed in one of augite: c) and d), respectively plane polarized light and crossed polar view microphotographs. KG23c-D3-17; Basalt lithic exhibiting a porphyritic structure consisting of a K-feldspar immersed in a ground paste composed of plagioclase, augite and magnetite. e) and f), respectively plane polarized light and crossed polar view microphotographs. Mineral abbreviation (Whitney and Evans, 2010): Aug, augite; Cal, calcite; Kfs, K-feldspar; Mhb, magnesiohornblende; Pl, plagioclase;

PT - Granite gneiss inclusion (PG-3)

This group consist of four samples: AAS1-28, AAS1-157, ASS1-201 and ASS1-203.

The inclusions, 44.24% in avarage amount, (46.80 %, 39.92 %, 48.02 % and 42.24 %; AAS1-28, AAS1-157, ASS1-201 and ASS1-203) (Tab. 2) are predominantly elongated in shape, but also equidimensional and have a degree of rounding varies from angular

They show a spatial distribution between the two limits close-spaced and single-spaced (Quinn, 2022), mean average size of 4.78 Φ and a size distribution described by a type of sorting very well-sorted with mean values of 0.03 (0.03, 0.03, 0.03 and 0.02; AAS1-28, AAS1-157, ASS1-201 and ASS1-203) and a type of skewness coarse skewed with mean values of -0.13 (-0.10, -0.11, -0.15 and -0.16; AAS1-28, AAS1-157, ASS1-201 and ASS1-203) (Folk, 1974; Folk and Ward, 1957; Friedmann, 1961) (Fig. 3; Tab. 2).

The porosity consists mainly of vughs (micro-mega) and rarely of planar voids (micro-meso) (Quinn, 2022). Its average amount is 15.44 % (13.04 %, 17.94 % and 15.34 %; AAS1-28, , ASS1-157 and ASS1-201) excluding the sample ASS1-203 due to its significantly higher amount of 25.01% (Tab. 2).

The clay matrix (40.16 %, 42.14 %, 36.65 % and 32.75 %; AAS1-28, AAS1-157, ASS1-201 and ASS1-203) has an optical moderately active in the core, while, along its margins it is moderately active and secondarily active. Only sample AAS1-28 has a fully active body (Quinn, 2022).

The matrices show, both in plane polarized light and crossed polars, inhomogeneous blurred colouration from the core to the margins: from brown to red-brown for samples ASS1-201 and ASS1-28 and from brown to yellow-brown for samples AAS1-203 and AAS1-157 (Quinn, 2022).

The mineralogical phases both loose and aggregated in the lithics, which modes are expressed in Tab. 2., and the structures recognized in the latter can be traced to a granitic gneiss (Fig. 16, a-d). In this petrographic group (Tab. 2), the content of mica as inclusion increases (Fig. 16, a-d), ranging from an amount of about 4.00% to 5.66% for samples AAS1 201 and AAS1 203 respectively (Tab. 2). Epidote and amphiboles is rarely observed (Tab. 2), but the observation on these phases are still the same as in the previous petrographic groups.

In the fragments of the granite gneiss (~15-20%) (Terry and Chilingar, 1955), a granoblastic texture characterized by irregular triple points, recrystallized quartz with irregular boundaries formed by migration of grain boundaries by bulging and isoriented elongated quartz crystal can be observed (Spray, 1969; Winter, 2001) (Tab. 16, e-d). Occasionally, there is within quartz crystals in lithic an onset of dislocation migration that divides the grain into two unstrained subgrains whose edges appear less pronounced in thin section (Spray, 1969; Winter, 2001). The plagioclases when show albite twinning, the latter can be distorted in flame twinning and coupled partially with pericline one, while, the microcline can be showing a

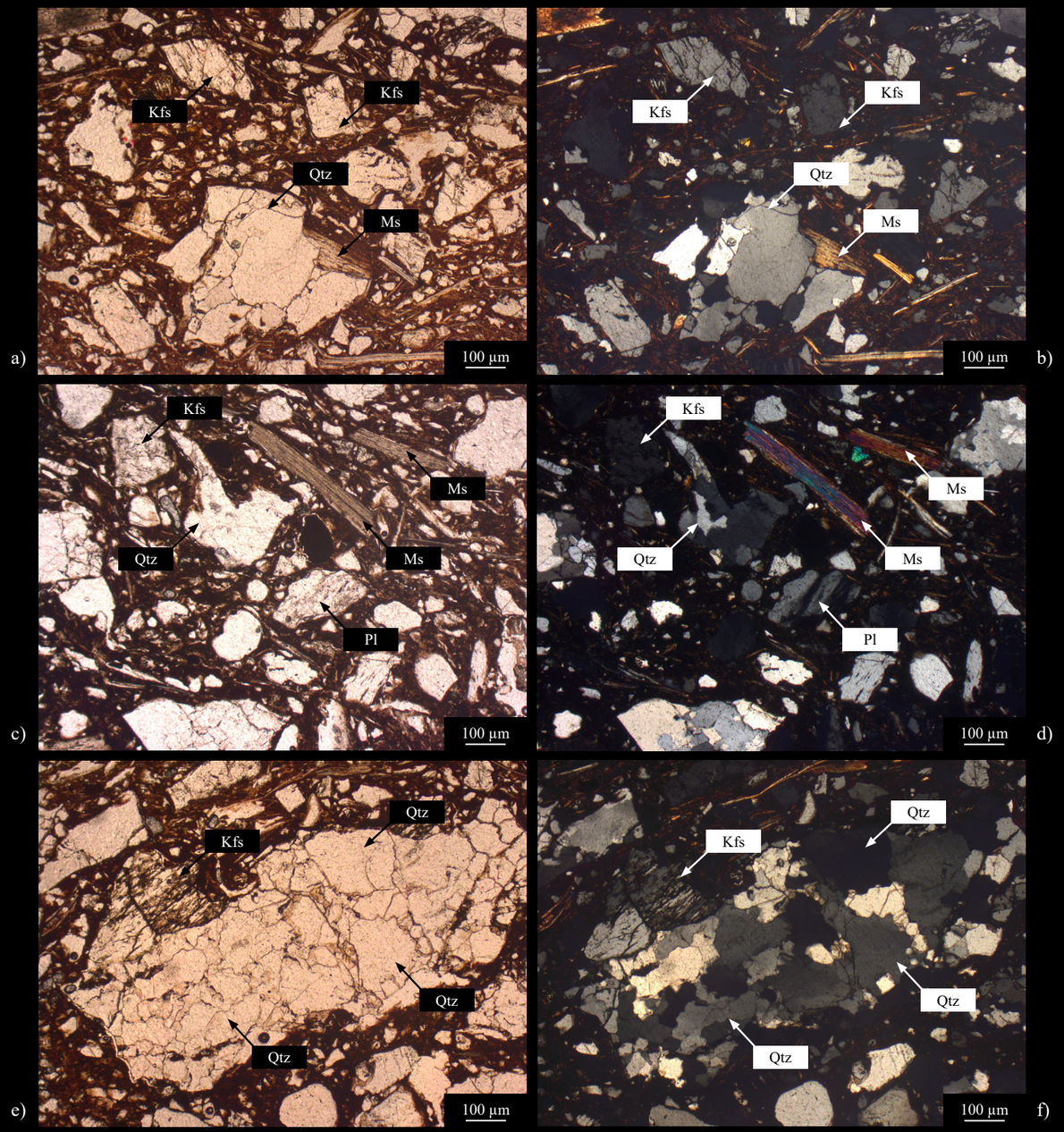

Fig. 16) AAS1-201; Lithics and loose mineralogical phases resulting from the disintegration of a granitic gneiss, an irregular granoblastic structure can be observed in lithics: a,c) and b,d), respectively plane polarized light and crossed polar view microphotographs. AAS-201; Isoriented elongated quartz crystals: e) and f), respectively plane polarized light and crossed polar view microphotographs. Mineral abbreviation (Whitney and Evans, 2010): Kfs, K-feldspar; Ms, muscovite; Pl, plagioclase; Qtz, quartz.

deformed and/or incomplete gridiron twinning and portion replaced by orthoclase. However, there also exists the occasion where orthoclase is the host phase of the microcline (Spray, 1969; Winter, J.D., 2001).

PT - Tonalitic gneiss inclusions (PG-4)

The ceramic sample 4Bis-1 is the only sample belonging to this petrographic group.

The inclusions (51.07 %) (Tab. 2) have both elongated and equidimensional shape and a degree of rounding varying from very-angular to sub-rounded, rarely rounded (Quinn, 2022). They show a spatial distribution between the two limits close-spaced and single-spaced (Quinn, 2022), average size of 4.73 Φ and a size distribution described by a type of sorting very well-sorted (0.03) and a type of skewness coarse skewed (-0.14) (Folk, 1974; Folk and Ward, 1957; Friedmann, 1961) (Fig. 3; Tab.2)

The porosity (10.6 %) (Tab. 2) consists mainly of vughs (micro-meso) and rarely to planar voids (micro-meso) (Quinn, 2022).

The clay matrix (38.35 %) (Tab. 2) has an optical inactivity in the core, while, along its margins it is moderately active and secondarily active (Quinn, 2022). The colouration of the matrix is, both in plane polarized light and crossed polars, dark brown in the core and light brown along the margins. Inhomogeneities in the colouration are blurred (Quinn, 2022).

The mineralogical phases both loose and aggregated in the lithics, which modes are expressed in Tab. 2., and the structures recognized in the latter can be traced to a tonalitic gneiss (Fig. 17). Indeed, it is very rare to observe pyroxene, amphibole, epidote and zoisite, but the observation on these phases are still the same as in the previous petrographic groups.

In the tonalitic gneiss lithics (15-20%) (Terry and Chilingar, 1955) it is possible to observe the granoblastic texture (Fig. 17, c-f) and recrystallized quartz with irregular boundaries, formed by grain boundary migration by bulging (Fig. 17, c-d) (Spray, 1969; Winter, 2001). Occasionally within quartz crystals, an onset of dislocation migration can be observed that divides the grain into two unstrained subgrains whose edges appear less pronounced in thin section (Spray, 1969; Winter, 2001) (Fig. 17, e-f). Additionally, when the plagioclase show albite twinning the latter can be distorted in flame twinning (Spray, 1969; Winter, 2001).

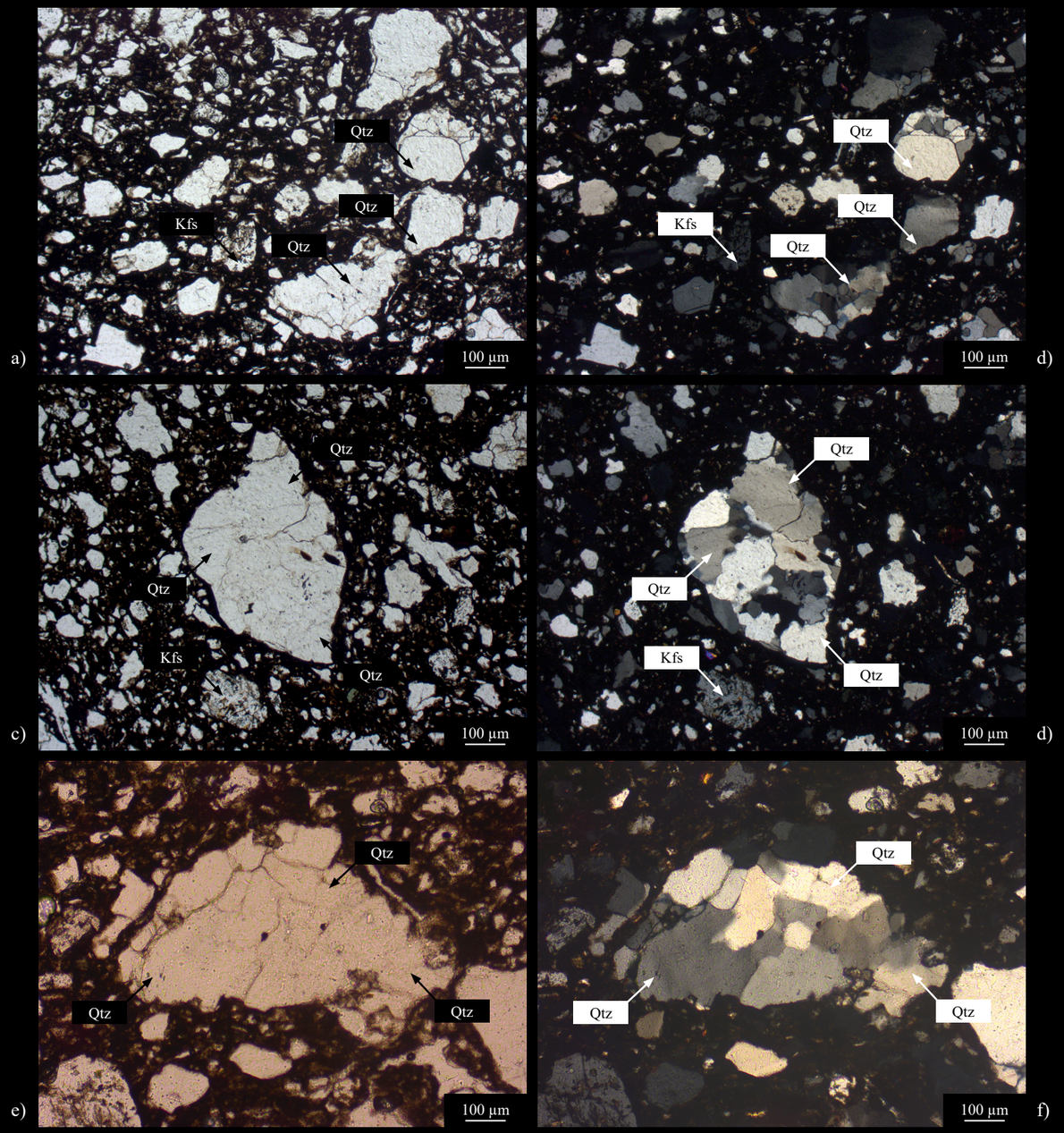

Fig. 17) 4Bis-1; Lithics and loose mineralogical phases resulting from the disintegration of a tonalitic gneiss: a) and b), 4Bis-1; respectively plane polarized light and crossed polar view microphotographs. Granoblastic texture and recrystallized quartz with irregular boundaries, formed by grain boundary migration by bulging c) and d), respectively plane polarized light and crossed polar view microphotographs. 4Bis-1; Onset of dislocation migration within quartz crystals divides the grain into two unstrained subgrains whose edges appear less pronounced in thin section: e) and f), respectively plane polarized light and crossed polar view microphotographs. Mineral abbreviation (Whitney and Evans, 2010): Kfs, K-feldspar; Qtz, quartz.

5.2. Chemistry and isotope geochemistry

The dendrogram, resulting from the processing of the chemical data (Tab.5) through cluster analysis (Fig. 18), performing the cut highlighted by the dotted red line (Fig. 18), yielded a division of the sampling into 15 clusters. The cut was performed to maximise the exclusion of agglomerations whose occurrence would be forced by the agglomerative methodology applied and at the same time of those deemed unrealistic considering previous observations. For the cluster analysis to return a significant and resolving result, it was carried out by simultaneously considering both major and trace elements. Attributes were excluded if, when assessing the associated uncertainty, they were found to have values too close to or below the detection limit or had a large measurement lack that made them unrepresentative for the entire sampling. Below are the excluded attributes: MnO, Ta, Th, U, S, Pr, Nd, Sm and Yb.

The reason for the origin of each identified cluster has to be explained and to do it clearly and in detail was done as previously explained in Materials and Methods, since, by employing a PCA, the result of the cluster analysis is only partially observable and consequently partially interpretable (Fig.).
In fact, the difference between the chemical groups that the method used in this case study allows us to observe and interpret are, using a PCA instead, in some cases difficult to study and sometimes unidentifiable. Thus, where the difference between the chemical groups lies is slight, PCA does not allow the visualisation of the latter obliterating and homogenising them. Differences, these, which instead take on a certain relevance in a case study such as this.

Please note that the following treatment refers to standardised chemical data considering major oxides and trace elements simultaneously.
There are two main chemical groups (CG), called CG-4 and CG-10, which diverge from each other due to a differeant concentration of SiO_2, resulting higher in the CG-4 group (Fig. no.). The high samples number of the two groups makes their chemistry the major contributor to the definition of the chemistry mean during standardization of the data (Tab.). This makes these groups the closest to 0 and the groups from which the rest diverge. Thus, for each divergent i-th group, the set of major oxides and trace elements which, as explained in materials and methods, assume values justifying their origin is given. Positive divergent values are given before negative ones and separated from the latter by a semicolon. In addition, the sum of the positive and the one of wnegative values define the maximum distance of the i-th group with respect to 0. In the description of each i-th group, two types of attributes were identified according to their contribution in imposing distance between the i-th group and 0. Those providing a higher contribution are marked with an *. The above description follows:

CG-1) TiO_2*, Al_2O_3, Fe_2O_3*, MgO*, CaO*, Sr, Cr, Sc*, V*, Co*; SiO_2*, K_2O, P_2O_5 Rb*, Y, Zr, Nb*, Ba, Hf, La, Ce (Fig. 20)

CG-2) Al_2O_3, Fe_2O_3, MgO*, CaO*, Cr*, Ni*, Sc*, V, Cu*; SiO_2*, TiO_2, Na_2O, K_2O*, Rb*, Y, Zr, Nb, Ba, Hf, Pb, La, Ce (Fig. 21)

CG-3) TiO_2, CaO, Y, Zr*, Hf*; Rb (Fig. 22)

CG-5) CaO*, Y, Co, La; Al_2O_3*, Na_2O, K_2O, Rb, Ba, Zn, Ga (Fig. 23)

CG-6) SiO_2, Na_2O, P_2O_5*, Sr, Y, Sc, Cl; TiO_2*, Fe_2O_3, MgO*, K2O, Rb*, Zr, Nb*, Cr, Ni, Co, Cu, Zn*, Ga, Hf, Pb, F*, Le, La (Fig. 24)

CG-7) SiO_2, TiO_2, CaO, Zr, Hf; Al_2O_3, Fe_2O_3, Rb, Zn (Fig. 25)

CG-8) TiO_2*, Fe_2O_3, Nb, Cr*, Ni, Co, V*, Cl; Al_2O_3, Na_2O, Rb, Sr, Ba, Pb (Fig. 26)

CG-9) SiO_2, Cl**; CaO, Ba (Fig. 27)

CG-11) Fe_2O_3, P_2O_5*, Y*, Nb, Cr, Zn*, Ga, Hf, Pb, F, La, Ce; SiO_2, MgO, CaO, Sr, Sc, V, Cu (Fig. 28)

CG-12) Al_2O_3, Fe_2O_3, MgO, Y, Nb, Ni, Zn; SiO_2, Na_2O (Fig. 29)

CG-13) Al_2O_3*, K_2O*, Rb*, Ga, Pb; TiO_2*, Fe_2O_3, MgO*, CaO, NaO, Y, Ni, Sc, V, Co, Cu, Zn* (Fig. 30)

CG-14) Na_2O, K_2O, Ba, Ga, Pb, La, Ce; TiO_2, Fe_2O_3, Y, V, Sc (Fig. 31)

CG-15) La, Ce; Cr, Ni (Fig. 32)

These sums above mentioned are graphed in appropriate binary diagrams to make the distance between the i-th group and 0 visualisable; diagrams representing different angles of observations of the system that otherwise could not be described in its entirety.
Since these sums include both trace elements and major oxides, it was decided to prefer the use of diagrams constructed on standardised data so as not to obliterate the weight of the trace elements due to the value of the major oxides present in the sum and which are transformed into ppm for coherence (Fig. 32).
However, the treatment is on standardised data with a parallelism with non-standardised data, demonstrating the goodness of using the first type of data. This is possible considering the sums where only major oxides or trace elements are present, as in this case the trend between standardised and non-standardised data must be coherent if standardisation does not distort the data; and so it turns out. (Fig. 32).

The division imposed by this cluster analysis mirrors that resulting described in petrography e microchemical observation, imposing a division of the samples belonging to the PG granodioritic gneiss inclusion by site of origin. It also happens that groups whose majority of samples are referable to a specific archaeological site may include some samples associated with different sites.

Lastly, crucial information in the study of the firing conditions of artefacts is the calcium oxide concentration. The latter exceeds values of 6 wt. % only in the samples: SEG-6-4 (6.52 wt. %), UA50-4-21 (7.08 wt. %), 1Bis-1 (7.04 wt. %), UA50-3-10 (7.34 wt. %), UA50-4-19 (12.41 wt. %) and UA50-4-25 (6.01 wt. %) (Tab. 5).

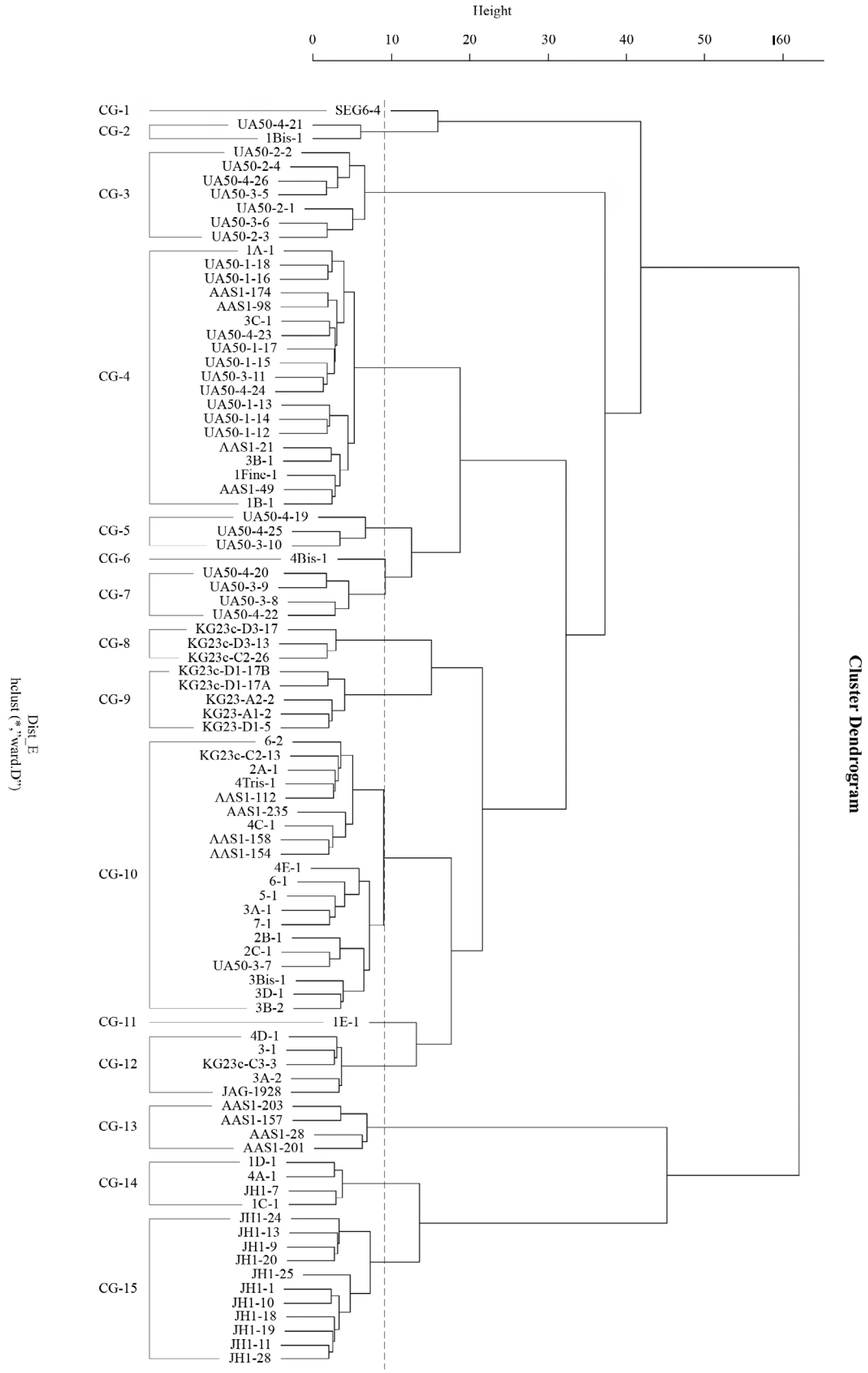

Fig.18) Cluster dendogram showing the partition into 15 chemical groups considering the chemical attributes of the sampling; the latter partition took advantage of a euclidean distance function elaborated by a ward.D. hierarchical agglomerative method. In dashed lines, the cut that led to the birth of the 15 groups just mentioned is visible.

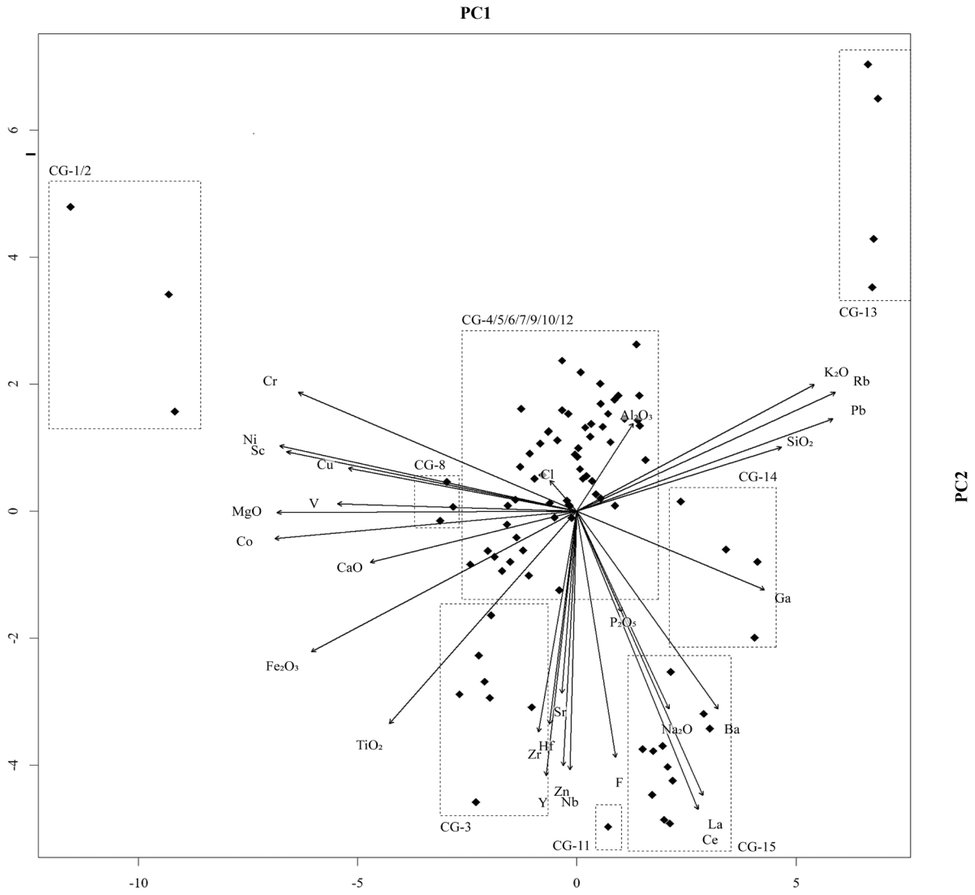

Tab. 19) PCA biplot about chemical atributes of the sampling. In the dashed boxes are the samples of the chemical group(s) marking them

Tab. 5) Major oxide (in wt.%) and trace element (in ppm) data of the sampling.

Sample	Site	Petrographic Group	Chemical Group	SiO_2	TiO_2	Al_2O_3	Fe_2O_3	MgO	CaO	Na_2O	K_2O	P_2O_5	Rb	Sr	Y	Zr	Nb	Ba	Cr	Ni	Sc	V	Co	Cu	Zn	Ga	Hf	Pb	F	Cl	La	Ce
SEG-6-4	SEG6	PG-1	CG-1	52.95	2.11	17.84	13.86	3.95	6.52	1.41	0.69	0.19	8	511	15	79	6	418	172	58	35	523	39	32	99	19	2	5	594	92	10	20
1Bis-1	SEG6	PG-1	CG-2	53.25	0.90	21.14	8.85	5.84	7.04	0.94	0.84	0.72	12	435	20	131	7	613	336	146	43	160	47	72	61	17	4	7	697	496	20	36
UA50-4-21	UA50	PG-1	CG-2	55.58	0.83	17.34	8.53	7.95	7.08	0.84	1.28	0.11	14	450	19	122	8	410	611	169	36	173	47	87	68	14	3	7	629	68	15	25
UA50-2-1	UA50	PG-2	CG-3	63.37	1.27	14.69	8.67	2.76	3.97	2.09	2.39	0.24	29	307	42	449	12	814	113	55	23	167	24	31	112	18	11	12	834	494	35	71
UA50-2-2	UA50	PG-2	CG-3	64.23	1.85	14.38	8.27	2.79	4.30	1.68	1.69	0.26	29	434	35	765	17	679	167	71	19	168	21	35	87	18	18	10	808	274	29	62
UA50-2-3	UA50	PG-2	CG-3	64.06	1.49	14.41	8.07	3.06	4.01	1.63	2.33	0.37	29	476	34	414	13	836	154	86	20	163	26	33	98	17	10	8	1024	162	23	53
UA50-2-4	UA50	PG-2	CG-3	64.75	1.70	14.88	7.83	2.82	3.94	1.42	1.85	0.35	26	412	31	518	15	653	145	77	18	156	23	38	91	16	13	17	730	80	22	40
UA50-3-5	UA50	PG-2	CG-3	63.76	1.63	14.13	8.07	2.91	5.01	1.78	1.80	0.34	26	494	35	570	14	838	156	74	19	176	25	36	92	17	14	8	727	200	21	47
UA50-4-26	UA50	PG-2	CG-3	64.78	1.63	13.93	8.01	2.87	4.51	1.86	1.66	0.23	24	448	32	557	14	696	146	75	18	168	23	38	88	18	14	11	671	144	28	56
UA50-3-6	UA50	PG-2	CG-3	64.77	1.52	14.14	7.81	2.64	4.69	1.84	1.74	0.29	27	499	34	442	13	845	161	77	20	160	26	35	88	17	11	10	955	115	30	61
1Fine-1	SEG7	PG-2	CG-4	66.91	1.04	14.65	6.60	2.71	2.86	1.73	2.54	0.55	42	379	27	191	11	712	144	82	14	133	21	43	80	15	5	13	900	79	28	50
1A-1	K2	PG-2	CG-4	66.38	0.95	15.83	6.38	2.12	2.65	2.00	2.90	0.34	52	405	27	198	11	1006	103	56	17	123	20	34	88	19	6	14	617	158	28	52
1B-1	SEG7	PG-2	CG-4	67.78	0.92	14.74	6.86	2.30	2.80	1.75	2.05	0.33	49	417	29	170	10	930	129	63	20	139	22	44	88	19	5	12	989	34	30	60
3B-1	SEG14	PG-2	CG-4	66.24	1.06	15.90	7.40	1.85	2.52	1.69	2.21	0.72	45	437	28	189	12	835	158	68	19	158	18	37	74	17	5	11	771	26	22	39
3C-1	SEG56	PG-2	CG-4	67.13	0.96	15.28	6.96	2.26	2.44	1.51	2.88	0.17	51	442	23	159	9	959	138	57	14	131	18	39	96	17	4	11	778	24	26	47
AAS1-174	ASS1	PG-2	CG-4	68.36	0.87	14.07	6.77	2.61	2.90	1.55	2.18	0.16	58	388	28	152	10	702	105	49	16	120	23	43	101	16	4	12	806	65	26	54
UA50-1-12	UA50	PG-2	CG-4	66.68	1.01	14.64	7.04	2.60	2.83	1.56	2.89	0.33	51	431	28	210	10	633	142	67	19	156	19	59	80	17	6	14	814	104	19	40
UA50-1-13	UA50	PG-2	CG-4	68.00	0.97	14.47	6.86	2.36	2.52	1.50	2.82	0.13	52	405	24	184	10	614	145	65	18	164	24	51	75	15	5	12	722	46	22	37
UA50-1-14	UA50	PG-2	CG-4	66.05	1.04	14.65	6.97	3.07	3.57	1.50	2.57	0.17	48	433	26	194	11	602	139	68	18	146	23	54	81	16	5	11	876	38	26	50
UA50-1-15	UA50	PG-2	CG-4	67.80	0.87	14.27	6.73	2.28	2.97	1.74	2.74	0.19	51	469	26	179	9	683	121	58	19	143	21	44	78	17	5	12	784	62	27	55
UA50-1-16	UA50	PG-2	CG-4	65.96	0.91	15.27	6.92	2.61	2.72	1.64	3.22	0.32	58	438	27	169	10	792	127	63	19	137	24	44	99	16	5	12	706	72	27	57
UA50-1-18	UA50	PG-2	CG-4	65.78	0.89	15.15	7.15	2.43	2.97	1.82	3.02	0.33	56	388	28	166	9	754	125	63	19	137	21	29	92	17	5	14	721	77	25	45
UA50-3-11	UA50	PG-2	CG-4	69.31	0.93	14.09	6.17	2.06	2.49	1.75	2.59	0.22	49	431	26	184	10	652	135	61	17	134	19	41	77	16	5	12	699	70	23	51
UA50-4-23	UA50	PG-2	CG-4	67.81	0.84	14.81	6.74	2.23	2.56	1.89	2.52	0.22	50	371	23	137	9	677	110	60	14	140	17	34	87	18	4	11	704	42	26	50
UA50-4-24	UA50	PG-2	CG-4	68.41	0.93	14.18	6.21	2.09	3.04	1.77	2.63	0.34	53	434	28	181	9	690	141	58	17	137	17	35	80	16	5	14	740	85	22	37
AAS1-21	ASS1	PG-2	CG-4	68.45	1.14	14.09	7.32	2.06	2.65	1.66	2.02	0.22	47	408	25	175	11	728	160	67	16	152	15	38	84	18	5	10	704	47	20	45
AAS1-49	ASS1	PG-2	CG-4	66.60	0.93	14.26	7.28	2.71	3.27	1.76	1.76	0.49	48	448	27	171	11	751	129	60	17	150	19	34	85	17	5	15	859	577	25	56
AAS1-98	ASS1	PG-2	CG-4	68.19	0.82	14.11	6.81	2.30	3.04	1.48	2.46	0.34	57	435	28	157	9	802	109	52	18	148	20	43	99	17	5	11	764	97	19	36
UA50-1-17	UA50	PG-2	CG-4	69.39	0.96	14.11	6.26	2.05	2.38	1.48	2.91	0.12	52	430	21	173	11	645	130	52	14	138	14	39	71	16	5	14	661	68	21	32
UA50-3-10	UA50	SPG-1	CG-5	68.18	1.42	11.16	6.50	2.41	7.34	1.10	1.19	0.22	25	412	34	294	11	473	143	69	16	169	25	34	72	13	8	12	863	68	30	56
UA50-4-19	UA50	SPG-1	CG-5	60.73	1.10	12.21	7.19	2.80	12.4	0.82	2.00	0.26	38	461	38	221	13	631	138	75	11	163	27	35	79	17	6	11	759	57	35	53
UA50-4-25	UA50	SPG-1	CG-5	70.40	1.01	11.15	6.11	2.24	6.01	0.91	1.44	0.30	34	269	34	217	11	515	132	66	14	133	25	33	74	15	6	14	931	142	36	75
4Bis-1	ES2	PG-4	CG-6	69.66	0.68	14.81	5.39	0.96	3.14	2.03	1.37	1.51	10	555	38	149	7	819	87	28	21	145	9	13	59	14	4	6	425	217	17	30
UA50-3-8	UA50	PG-2	CG-7	67.77	1.27	14.02	6.01	2.27	4.59	1.79	1.66	0.24	32	475	26	271	11	582	104	56	13	135	21	31	69	18	7	13	529	112	25	42
UA50-3-9	UA50	PG-2	CG-7	67.18	1.34	14.13	6.51	2.21	4.70	1.59	1.72	0.20	33	432	26	250	10	618	151	84	17	147	20	37	75	15	7	8	758	53	23	47
UA50-4-20	UA50	PG-2	CG-7	67.13	1.31	13.85	6.40	2.08	5.13	1.66	1.78	0.27	34	433	28	256	11	623	127	83	15	142	24	34	72	17	7	9	670	84	17	35
UA50-4-22	UA50	PG-2	CG-7	68.73	1.30	14.15	5.41	1.73	3.52	2.14	2.38	0.27	36	464	23	248	9	723	87	47	14	126	16	18	71	15	7	11	424	94	21	42
KG23c-C2-26	KG23c	SPG-2	CG-8	67.57	1.67	12.59	8.20	2.48	3.05	1.35	2.42	0.17	30	376	25	193	14	494	271	88	20	190	28	43	92	16	5	8	675	913	30	54
KG23c-D3-13	KG23c	SPG-2	CG-8	66.13	1.66	13.28	8.54	2.64	2.81	1.31	2.86	0.27	35	359	28	191	15	476	251	88	21	200	33	40	91	18	5	9	718	823	28	63
KG23c-D3-17	KG23c	SPG-2	CG-8	66.12	1.78	13.76	8.76	2.69	3.05	1.33	1.82	0.23	30	369	28	208	17	489	249	95	16	211	25	48	92	17	6	10	640	406	25	52
KG23-A1-2	KG23	PG-2	CG-9	66.39	0.93	15.02	6.74	2.94	2.34	1.56	3.29	0.30	53	381	28	156	12	608	119	64	22	140	20	40	92	17	4	12	644	1251	19	41
KG23-A2-2	KG23	PG-2	CG-9	65.70	1.06	15.42	7.30	2.77	2.91	1.50	2.61	0.20	51	405	28	194	12	645	148	64	18	150	21	33	95	18	6	13	590	1763	22	42
KG23c-D1-17A	KG23	PG-2	CG-9	66.46	1.08	14.95	7.35	2.50	2.47	1.70	2.59	0.27	50	356	28	194	13	560	155	67	16	152	17	40	108	17	5	12	693	2546	25	49
KG23c-D1-17B	KG23	PG-2	CG-9	66.06	1.14	15.00	7.39	2.69	2.35	1.71	2.81	0.21	48	360	30	205	12	632	159	62	20	166	21	33	130	17	6	13	586	2596	21	44
KG23-D1-5	KG23	PG-2	CG-9	67.23	0.92	15.02	6.54	2.59	2.07	1.61	3.26	0.23	55	349	26	160	11	534	120	62	19	141	16	47	119	17	4	12	680	1831	20	48
2A-1	JAG1	PG-2	CG-10	64.32	1.14	15.41	7.79	2.77	3.11	1.51	2.98	0.54	52	416	34	200	13	717	145	66	19	146	23	33	109	19	5	13	762	101	26	53
2B-1	SEG19	PG-2	CG-10	66.70	1.08	14.78	7.18	2.26	2.64	1.46	2.97	0.47	47	365	27	174	10	789	265	88	19	149	33	40	88	14	5	15	843	76	27	49
2C-1	SEG7	PG-2	CG-10	65.92	1.03	15.86	7.74	2.17	2.44	1.37	2.78	0.21	47	374	28	179	10	1103	142	75	22	153	30	40	86	17	5	12	855	44	22	45
3A-1	SEG7	PG-2	CG-10	63.81	1.07	16.45	8.13	2.33	2.72	1.27	3.06	0.47	59	455	31	181	12	1148	161	69	22	153	24	52	120	18	5	12	856	197	27	55
3B-2	SEG7	PG-2	CG-10	66.21	1.00	15.79	7.25	2.22	2.66	1.59	2.04	0.62	48	492	26	198	11	1659	146	66	19	130	19	33	90	17	5	11	757	69	23	42
3D-1	SEG7	PG-2	CG-10	64.83	1.03	17.09	6.65	2.20	2.95	1.74	2.63	0.40	47	411	26	213	12	1177	134	75	16	136	23	47	110	20	6	18	827	26	29	54

Tab. 5) (continued)

Sample	Site	Petrographic Group	Chemical Group	SiO_2	TiO_2	Al_2O_3	Fe_2O_3	MgO	CaO	Na2O	K2O	P_2O_5
4E-1	SEG7	PG-2	CG-10	61.15	1.18	20.66	8.55	1.76	2.61	0.95	1.72	0.97
4Tris-1	JAG1	PG-2	CG-10	64.84	1.06	16.66	7.87	2.57	2.41	1.65	2.26	0.30
6-1	EG4	PG-2	CG-10	62.97	1.05	16.81	8.36	2.28	3.00	1.37	2.95	0.52
6-2	JAG1	PG-2	CG-10	65.89	1.00	15.62	7.12	2.94	2.51	1.63	2.53	0.31
3Bis-1	SEG7	PG-2	CG-10	64.05	1.35	16.46	6.91	2.45	3.93	2.25	1.61	0.49
4C-1	SEG7	PG-2	CG-10	64.28	1.09	16.07	7.80	2.72	3.06	1.45	2.82	0.32
5-1	GEG23	PG-2	CG-10	60.70	1.10	16.73	8.45	3.16	5.16	1.24	2.43	0.47
7-1	GEG23	PG-2	CG-10	61.58	1.23	16.66	8.63	2.90	3.48	1.13	3.45	0.44
KG23c-C2-13	KG23	PG-2	CG-10	66.70	1.07	15.36	7.14	2.35	2.51	1.63	2.52	0.33
AAS1-154	ASS1	PG-2	CG-10	66.12	0.98	14.74	7.43	2.64	3.22	1.44	2.62	0.27
AAS1-158	ASS1	PG-2	CG-10	65.18	1.05	15.04	7.83	2.73	3.89	1.44	2.05	0.28
UA50-3-7	UA50	PG-2	CG-10	65.36	1.13	15.40	7.91	2.41	2.71	1.39	2.93	0.24
AAS1-112	ASS1	PG-2	CG-10	64.58	0.99	15.46	8.15	2.59	3.20	1.84	2.06	0.63
AAS1-235	ASS1	PG-2	CG-10	62.56	0.99	14.83	7.77	2.48	4.80	1.45	2.26	0.56
1E-1	JAG1	PG-2	CG-11	60.85	1.20	16.44	8.53	1.78	2.53	1.76	2.51	3.90
3-1	JAG1	PG-2	CG-12	59.88	1.11	16.91	9.32	3.34	3.50	1.21	3.31	0.87
3A-2	JAG1	PG-2	CG-12	59.87	1.22	17.82	9.42	3.28	2.85	1.10	3.35	0.57
4D-1	JAG1	PG-2	CG-12	59.98	1.21	16.64	8.87	3.18	3.85	1.19	3.49	1.03
JAG-1928	JAG1	PG-2	CG-12	61.29	1.27	17.03	9.14	2.90	3.31	1.40	2.56	0.53
KG23c-C3-3	KG23	PG-2	CG-12	60.52	1.17	17.84	9.33	3.22	2.55	1.05	3.42	0.37
AAS1-157	ASS1	PG-3	CG-13	65.15	0.54	19.93	4.93	0.90	1.58	0.92	5.72	0.09
AAS1-201	ASS1	PG-3	CG-13	65.10	0.54	19.93	3.61	0.66	2.39	0.59	5.19	1.56
AAS1-203	ASS1	PG-3	CG-13	65.73	0.55	21.58	3.74	0.66	1.34	0.63	5.21	0.23
AAS1-28	ASS1	PG-3	CG-13	67.90	0.54	19.42	3.61	0.91	1.63	1.18	4.28	0.20
1C-1	K2	PG-2	CG-14	65.19	0.84	16.47	5.61	2.06	2.89	2.07	3.55	0.71
1D-1	K2	PG-2	CG-14	66.27	0.87	15.78	5.67	2.14	3.18	2.07	3.05	0.51
4A-1	K2	PG-2	CG-14	66.16	0.90	15.31	5.47	2.73	2.91	2.01	3.55	0.51
JH1-7	JH1	PG-2	CG-14	66.79	0.90	16.02	5.40	1.58	3.21	2.08	2.94	0.57
JH1-1	JH1	PG-2	CG-15	64.86	1.11	16.29	7.54	2.48	2.43	1.94	2.49	0.40
JH1-10	JH1	PG-2	CG-15	63.71	1.22	16.49	7.79	2.32	3.00	2.15	2.34	0.39
JH1-11	JH1	PG-2	CG-15	62.66	1.38	16.42	8.12	2.36	3.36	2.07	2.58	0.55
JH1-13	JH1	PG-2	CG-15	64.34	1.34	15.12	7.62	2.41	3.34	1.96	2.66	0.55
JH1-19	JH1	PG-2	CG-15	62.60	1.41	16.36	8.33	2.38	3.01	2.03	2.83	0.51
JH1-20	JH1	PG-2	CG-15	65.68	1.08	15.45	6.71	2.20	3.15	2.16	2.53	0.53
JH1-24	JH1	PG-2	CG-15	66.62	1.16	15.43	6.77	1.86	3.07	1.99	2.20	0.37
JH1-18	JH1	PG-2	CG-15	63.00	1.20	17.49	7.86	2.16	3.10	1.95	2.22	0.48
JH1-28	JH1	PG-2	CG-15	63.63	1.14	16.45	7.83	2.54	3.04	1.75	2.72	0.37
JH1-25	JH1	PG-2	CG-15	64.95	1.05	15.37	7.64	2.80	3.02	1.43	2.57	0.53
JH1-9	JH1	PG-2	CG-15	63.99	1.44	15.58	7.51	2.14	3.38	2.14	2.50	0.74

Rb	Sr	Y	Zr	Nb	Ba	Cr	Ni	Se	V	Co	Cu	Zn	Ga	Hf	Pb	F	Cl	La	Ce
27	425	29	221	12	1096	125	104	20	175	23	52	102	21	6	14	718	40	25	52
56	340	29	189	11	605	141	71	19	144	25	48	110	20	5	10	577	41	24	43
49	563	30	187	13	1806	172	88	25	157	29	50	101	18	5	12	962	99	24	48
63	313	34	189	16	605	123	66	19	139	19	36	103	18	5	11	736	605	19	41
33	540	31	266	12	1244	123	65	17	143	24	36	84	18	7	12	660	44	25	49
53	460	29	193	12	704	150	73	18	146	22	61	110	17	5	12	673	51	27	59
58	429	31	188	14	1289	142	81	19	154	22	54	114	18	5	13	875	93	25	50
52	433	32	187	13	1060	178	80	25	156	24	51	124	17	5	14	700	150	27	57
54	351	30	203	12	583	150	59	16	150	19	36	107	18	6	12	413	555	25	49
60	394	31	170	10	983	123	63	15	138	20	56	113	17	5	11	834	65	25	54
60	367	32	188	12	978	127	62	15	142	23	54	113	19	5	14	663	85	28	58
51	445	29	195	12	767	148	76	23	154	30	45	108	19	5	13	906	32	23	43
62	424	31	168	12	896	123	61	16	174	20	48	107	20	5	10	692	137	22	50
63	568	31	173	11	732	127	59	20	165	21	47	117	19	4	13	822	130	23	42
50	306	42	253	18	861	155	71	16	133	29	27	185	22	7	14	1095	216	40	80
63	373	35	200	15	772	151	78	23	154	28	61	167	20	6	12	630	736	29	60
64	393	37	189	15	655	154	86	16	191	30	64	141	21	5	14	965	134	26	58
54	430	36	218	14	878	167	78	19	161	24	37	142	20	6	13	761	457	28	55
65	347	38	208	15	690	162	77	25	175	25	59	131	23	6	15	665	102	29	61
58	360	35	182	14	700	160	83	20	177	26	50	136	21	5	11	817	960	33	51
131	257	17	108	9	373	116	42	12	116	11	23	39	25	4	36	499	69	16	30
86	451	20	127	9	1079	67	39	13	70	14	16	54	23	4	34	651	202	26	46
98	241	17	137	10	973	82	33	11	113	14	18	33	28	4	34	517	94	10	22
106	300	24	205	9	638	83	26	8	86	6	16	44	23	6	18	802	55	27	55
62	443	22	242	9	1177	82	45	8	103	16	32	129	22	6	19	839	520	45	80
57	477	24	216	11	1238	96	54	14	105	17	23	92	22	6	18	675	70	43	81
52	439	24	202	10	1207	130	70	10	111	22	43	86	21	6	17	734	277	39	76
58	508	23	261	11	1718	89	37	12	93	15	33	116	21	7	16	990	69	45	79
57	411	30	210	13	989	70	38	16	129	24	30	136	21	6	15	919	91	50	91
53	483	34	249	14	1328	77	39	18	126	23	34	128	21	7	15	1083	273	45	90
52	511	33	245	15	1032	73	48	15	132	19	34	144	22	6	13	910	92	56	105
52	575	32	249	13	1919	71	44	13	130	20	25	134	19	6	13	926	776	40	80
59	480	35	245	15	1077	76	47	15	145	23	37	153	23	6	16	911	79	43	86
52	570	29	245	13	1289	61	36	12	119	20	31	116	21	6	16	1024	94	45	85
43	628	29	255	14	1678	67	38	14	123	12	24	93	19	7	15	877	64	50	90
43	497	34	278	15	1438	76	49	14	127	22	35	136	25	7	14	1075	78	55	97
53	572	34	229	15	1303	74	45	14	136	19	36	139	22	6	16	911	95	56	97
56	470	33	206	13	1785	69	46	16	110	22	41	141	21	6	15	1215	152	60	110
45	596	32	289	13	1823	59	42	14	128	24	35	122	21	7	17	1029	94	54	91

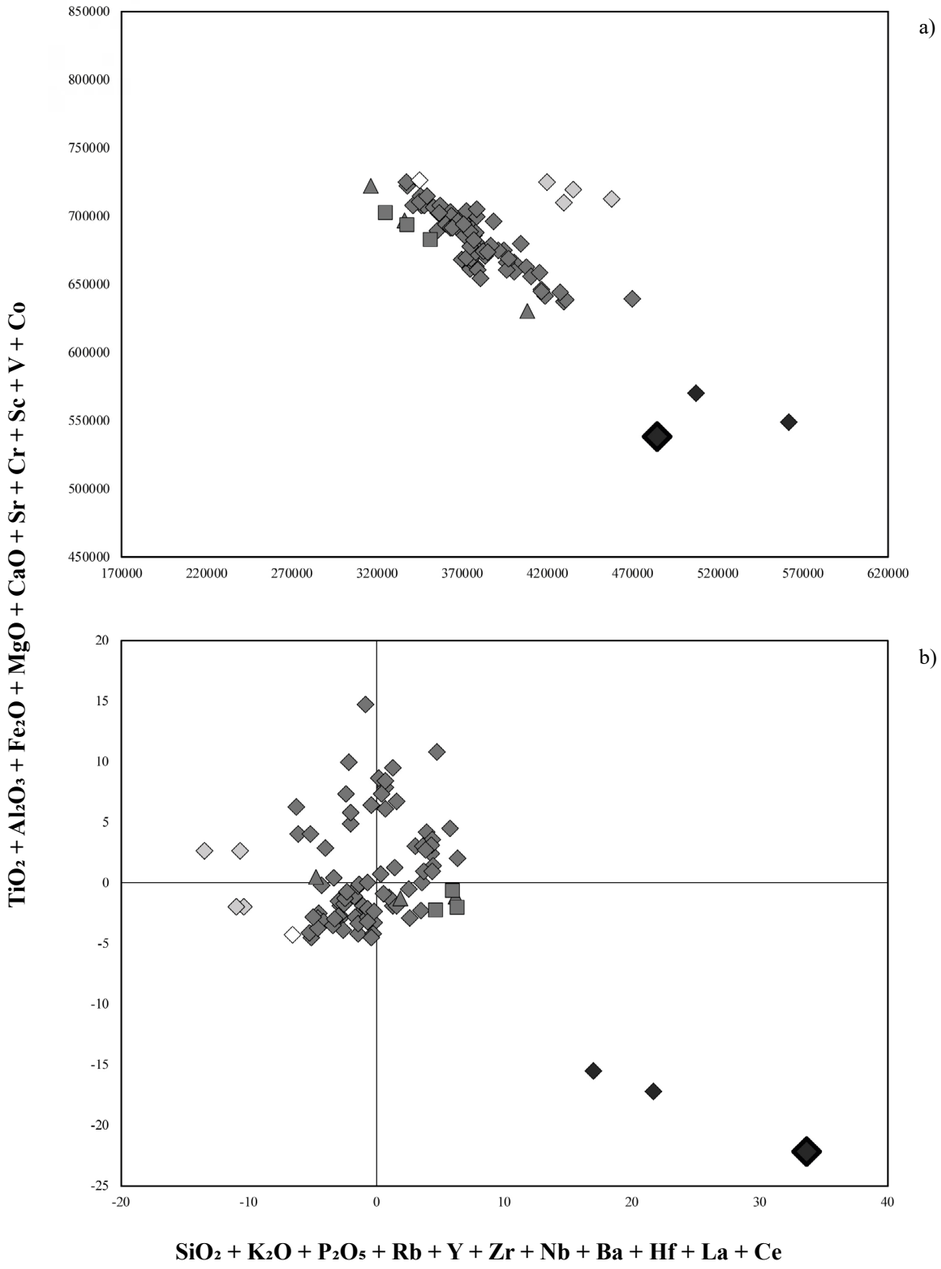

Fig. 20) Binary diagrams of CG-1 chemical data: a), ppm data; b), standardised data. Black rhombus, PT-Dioritic gnesiss inclusion; dark grey rhombus, PT-Granodioritic gnesiss inclusions; light grey rhombus, PT-Granitic gnesiss inclusions; white rhombus, PT-Tonalitic gnesiss inclusions; dark grey square, PT-Granodioritic gnesiss + basalt inclusions; dark grey triangle, PT-Granodioritic gnesiss + limestone inclusions; highlighted marker, CG-1.

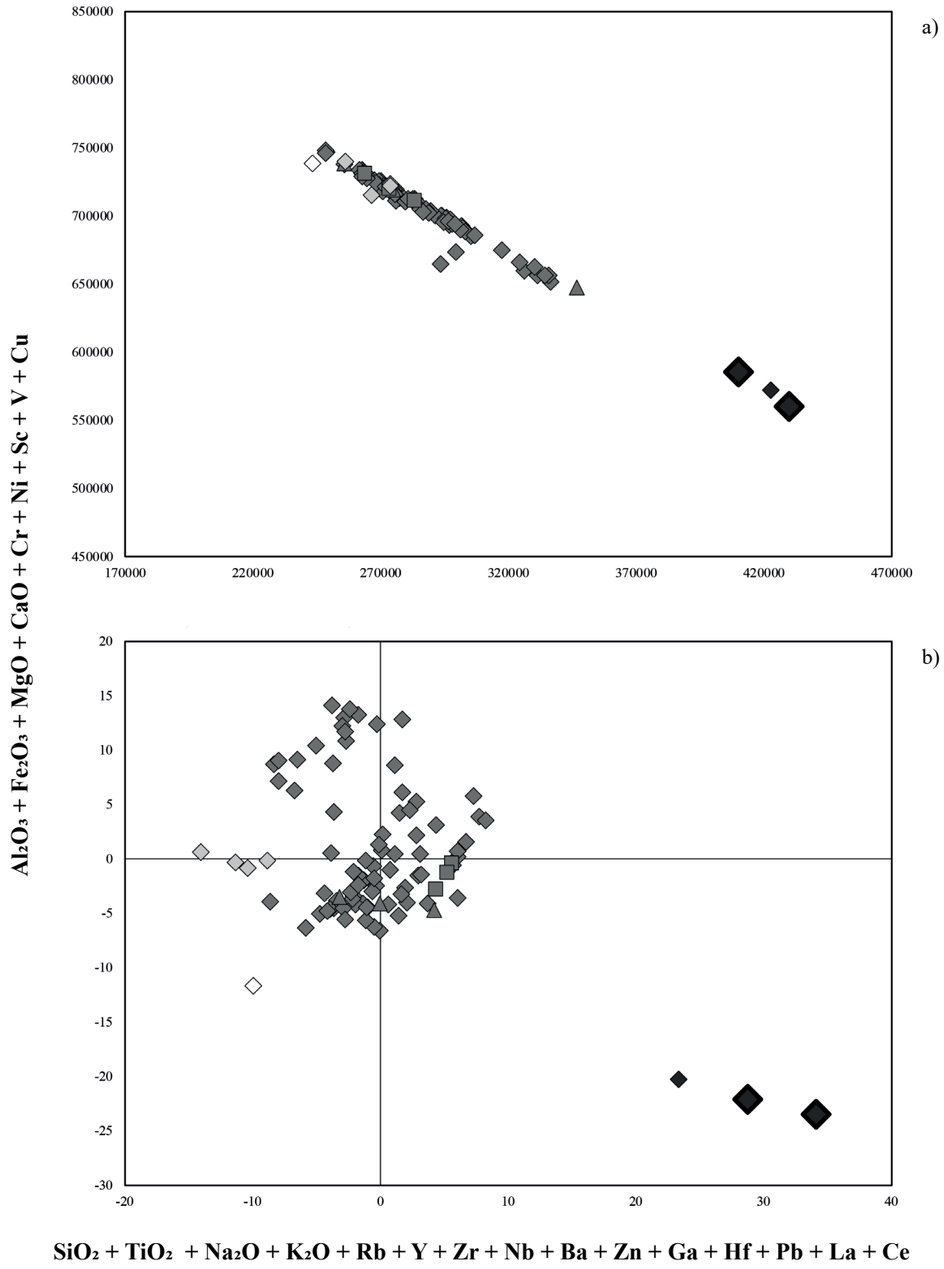

Fig. 21) Binary diagrams of CG-2 chemical data: a), ppm data; b), standardised data. Black rhombus, PT-Dioritic gnesiss inclusion; dark grey rhombus, PT-Granodioritic gnesiss inclusions; light grey rhombus, PT-Granitic gnesiss inclusions; white rhombus, PT-Tonalitic gnesiss inclusions; dark grey square, PT-Granodioritic gnesiss + basalt inclusions; dark grey triangle, PT-Granodioritic gnesiss + limestone inclusions; highlighted marker, CG-2.

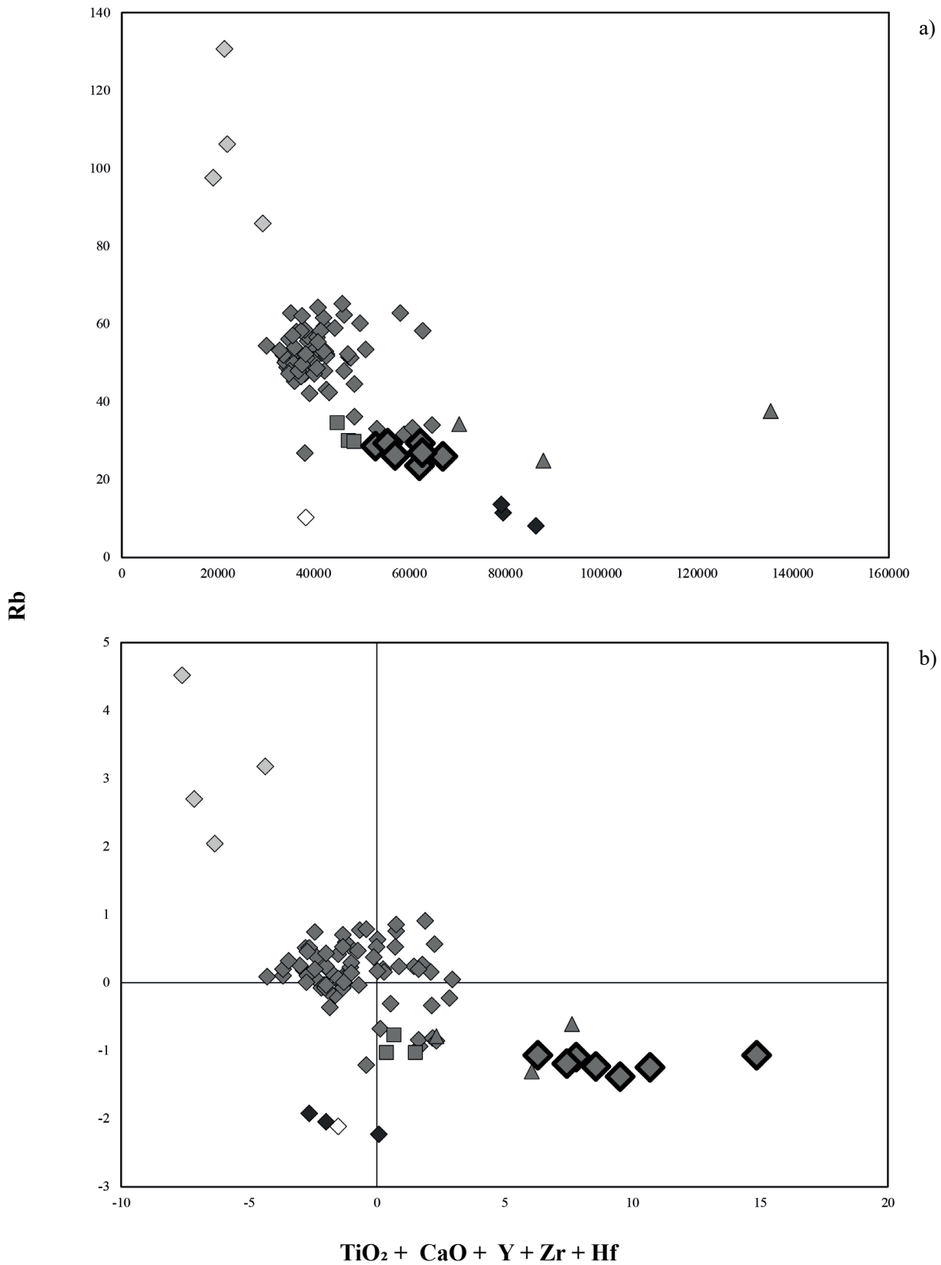

Fig. 22) Binary diagrams of CG-3 chemical data: a), ppm data; b), standardised data. Black rhombus, PT-Dioritic gnesiss inclusion; dark grey rhombus, PT-Granodioritic gnesiss inclusions; light grey rhombus, PT-Granitic gnesiss inclusions; white rhombus, PT-Tonalitic gnesiss inclusions; dark grey square, PT-Granodioritic gnesiss + basalt inclusions; dark grey triangle, PT-Granodioritic gnesiss + limestone inclusions; highlighted marker, CG-3.

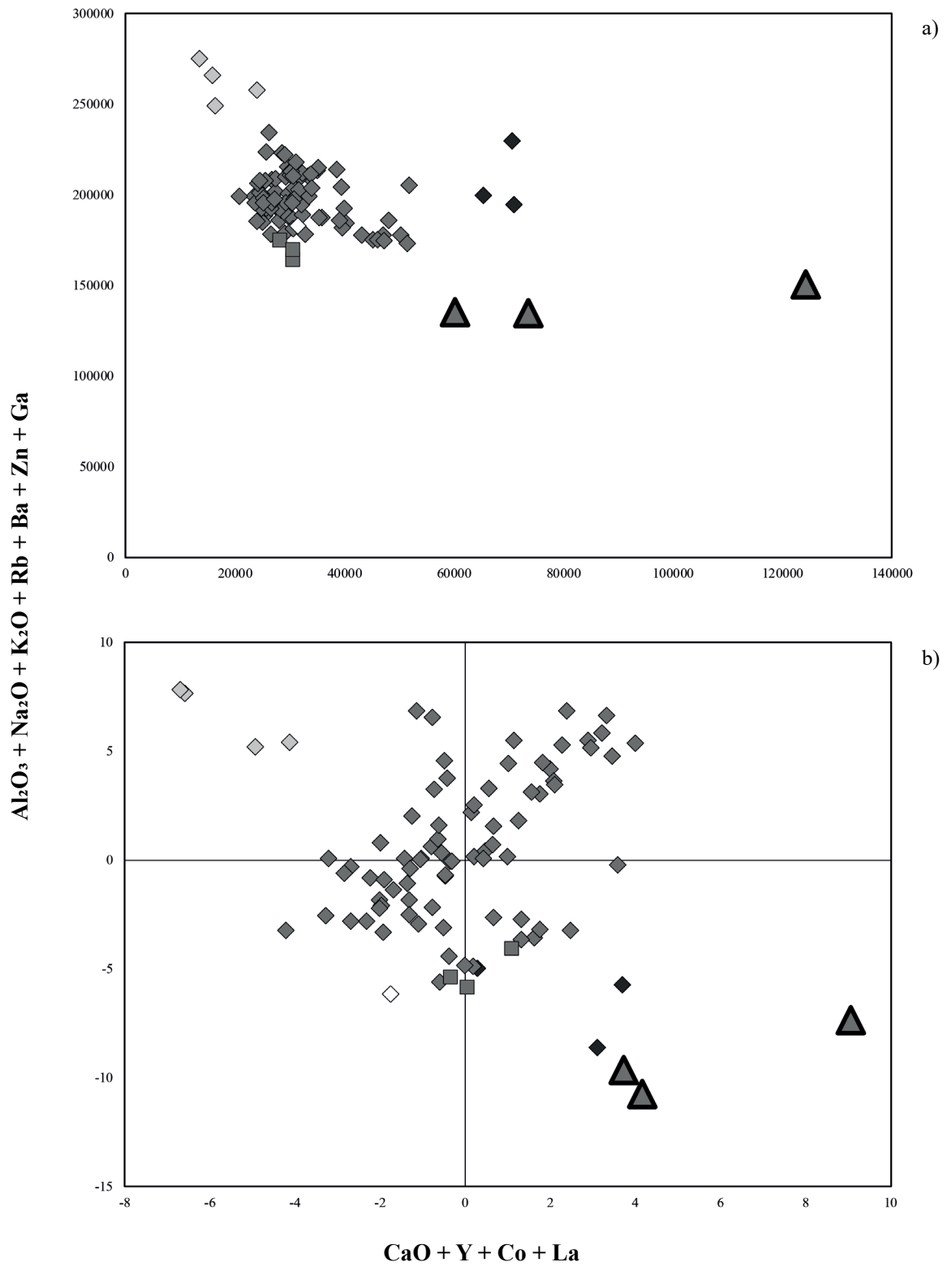

Fig. 23) Binary diagrams of CG-5 chemical data: a), ppm data; b), standardised data. Black rhombus, PT-Dioritic gnesiss inclusion; dark grey rhombus, PT-Granodioritic gnesiss inclusions; light grey rhombus, PT-Granitic gnesiss inclusions; white rhombus, PT-Tonalitic gnesiss inclusions; dark grey square, PT-Granodioritic gnesiss + basalt inclusions; dark grey triangle, PT-Granodioritic gnesiss + limestone inclusions; highlighted marker, CG-5.

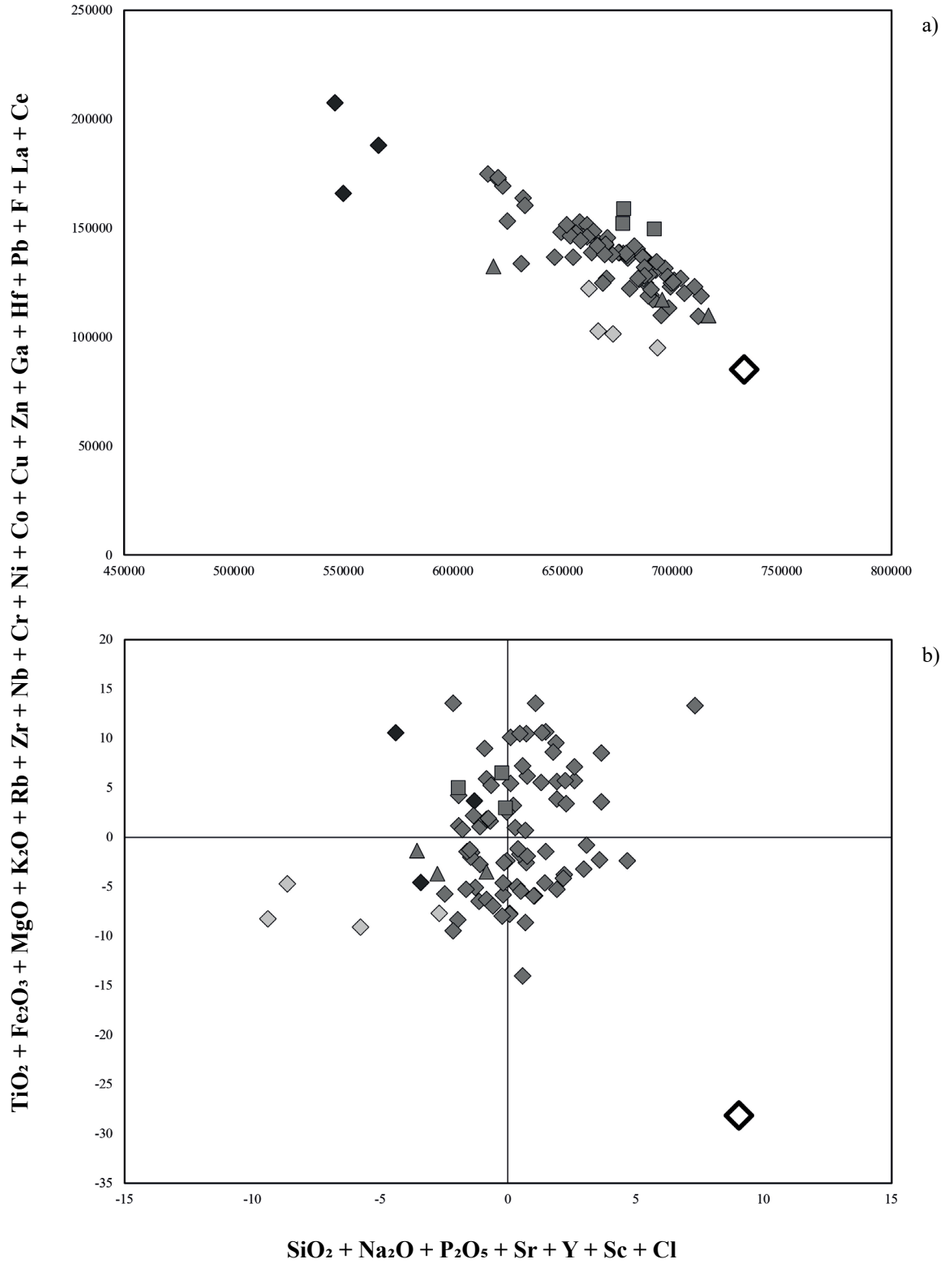

Fig. 24) Binary diagrams of CG-6 chemical data: a), ppm data; b), standardised data. Black rhombus, PT-Dioritic gnesiss inclusion; dark grey rhombus, PT-Granodioritic gnesiss inclusions; light grey rhombus, PT-Granitic gnesiss inclusions; white rhombus, PT-Tonalitic gnesiss inclusions; dark grey square, PT-Granodioritic gnesiss + basalt inclusions; dark grey triangle, PT-Granodioritic gnesiss + limestone inclusions; highlighted marker, CG-6.

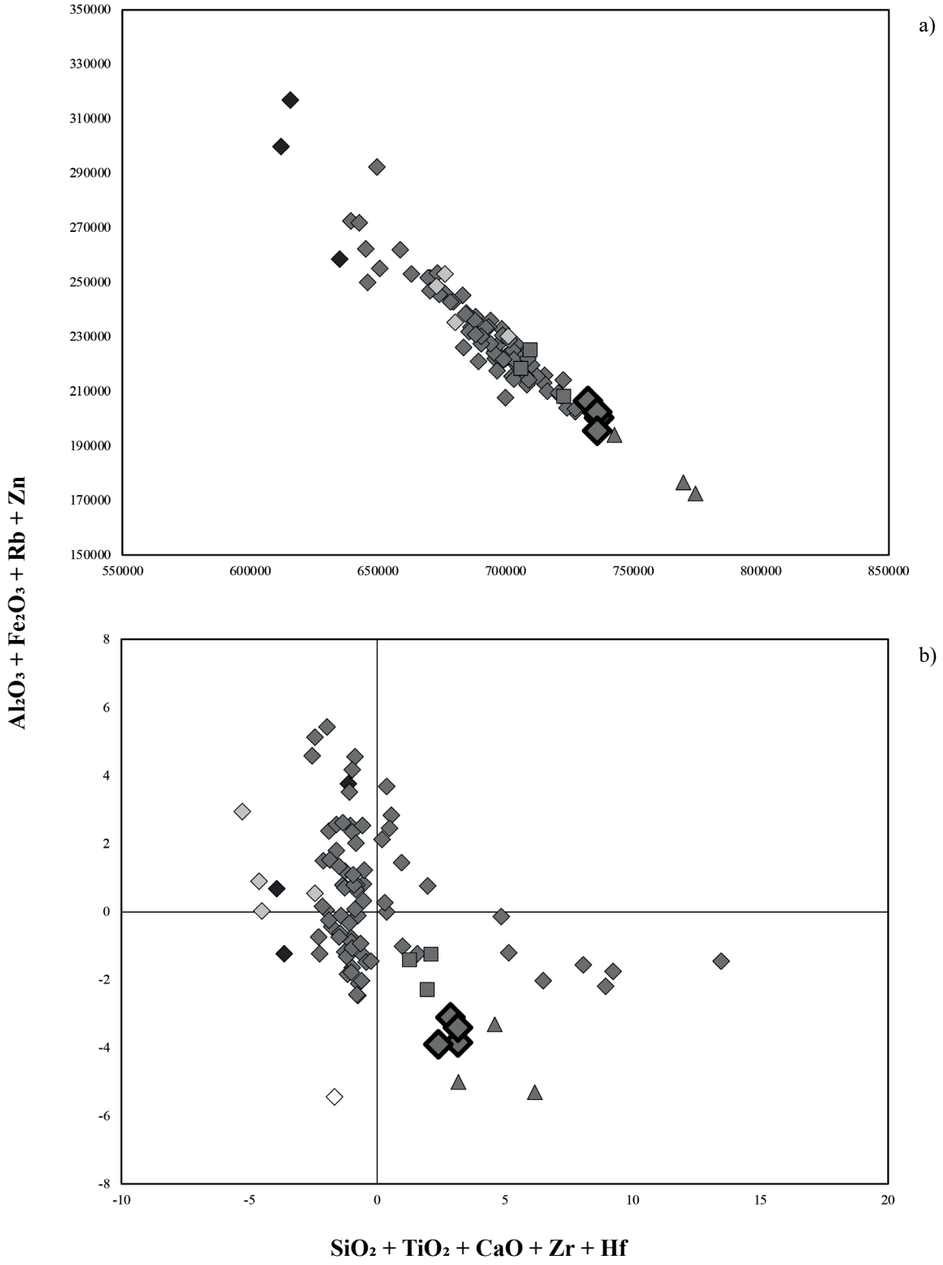

Fig. 25) Binary diagrams of CG-7 chemical data: a), ppm data; b), standardised data. Black rhombus, PT-Dioritic gnesiss inclusion; dark grey rhombus, PT-Granodioritic gnesiss inclusions; light grey rhombus, PT-Granitic gnesiss inclusions; white rhombus, PT-Tonalitic gnesiss inclusions; dark grey square, PT-Granodioritic gnesiss + basalt inclusions; dark grey triangle, PT-Granodioritic gnesiss + limestone inclusions; highlighted marker, CG-7.

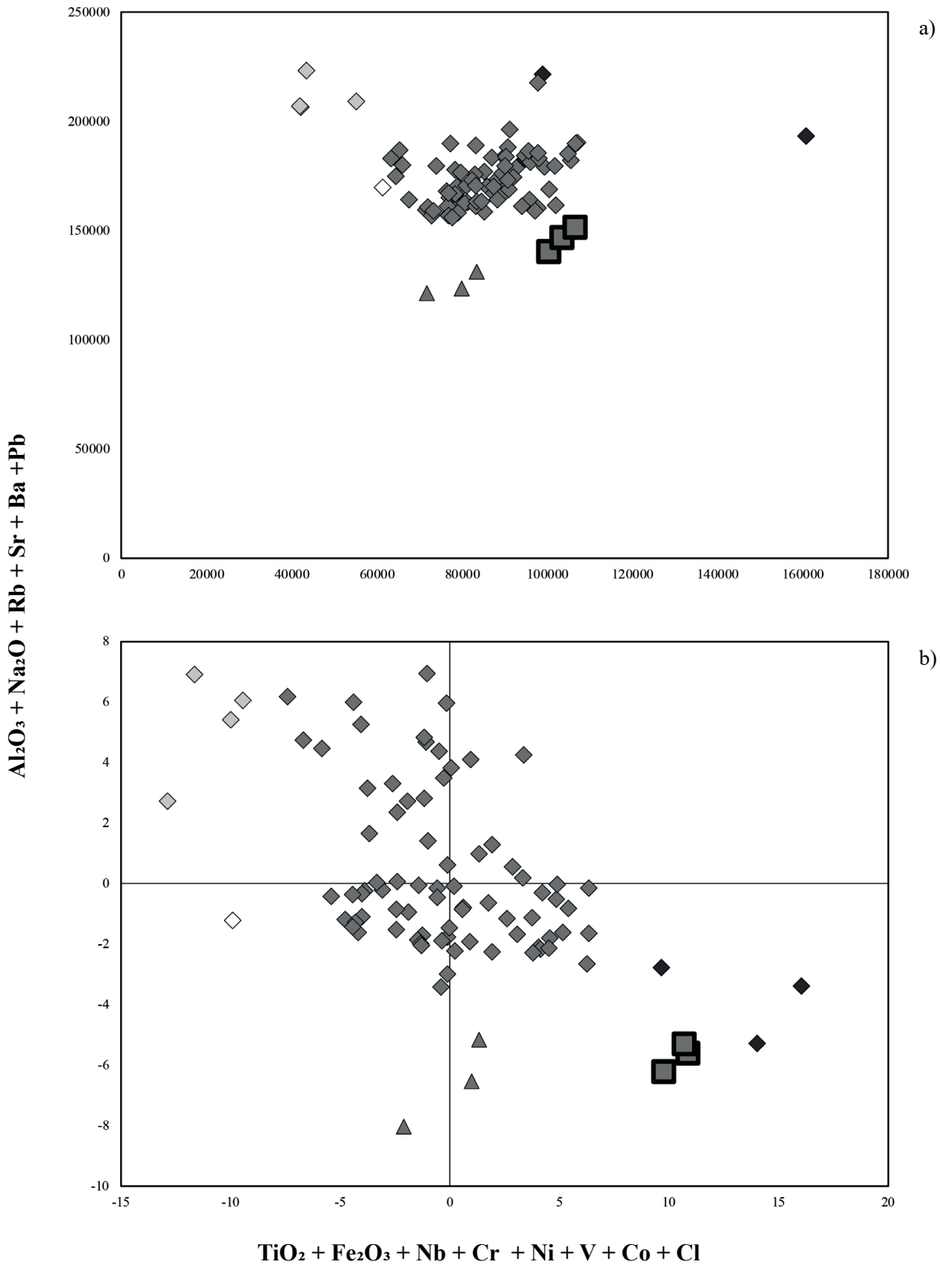

Fig. 26) Binary diagrams of CG-8 chemical data: a), ppm data; b), standardised data. Black rhombus, PT-Dioritic gnesiss inclusion; dark grey rhombus, PT-Granodioritic gnesiss inclusions; light grey rhombus, PT-Granitic gnesiss inclusions; white rhombus, PT-Tonalitic gnesiss inclusions; dark grey square, PT-Granodioritic gnesiss + basalt inclusions; dark grey triangle, PT-Granodioritic gnesiss + limestone inclusions; highlighted marker, CG-8.

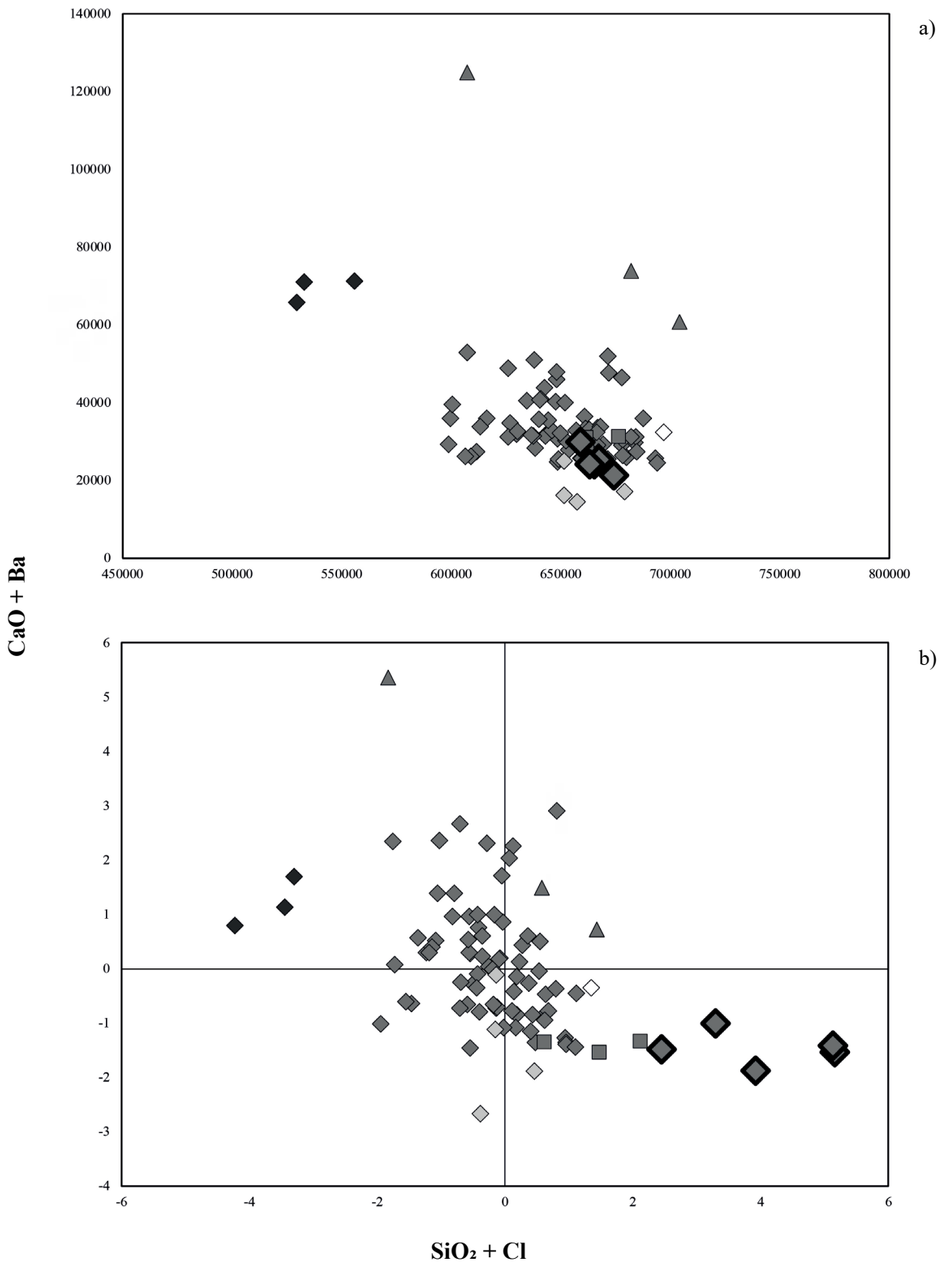

Fig. 27) Binary diagrams of CG-9 chemical data: a), ppm data; b), standardised data. Black rhombus, PT-Dioritic gnesiss inclusion; dark grey rhombus, PT-Granodioritic gnesiss inclusions; light grey rhombus, PT-Granitic gnesiss inclusions; white rhombus, PT-Tonalitic gnesiss inclusions; dark grey square, PT-Granodioritic gnesiss + basalt inclusions; dark grey triangle, PT-Granodioritic gnesiss + limestone inclusions; highlighted marker, CG-9.

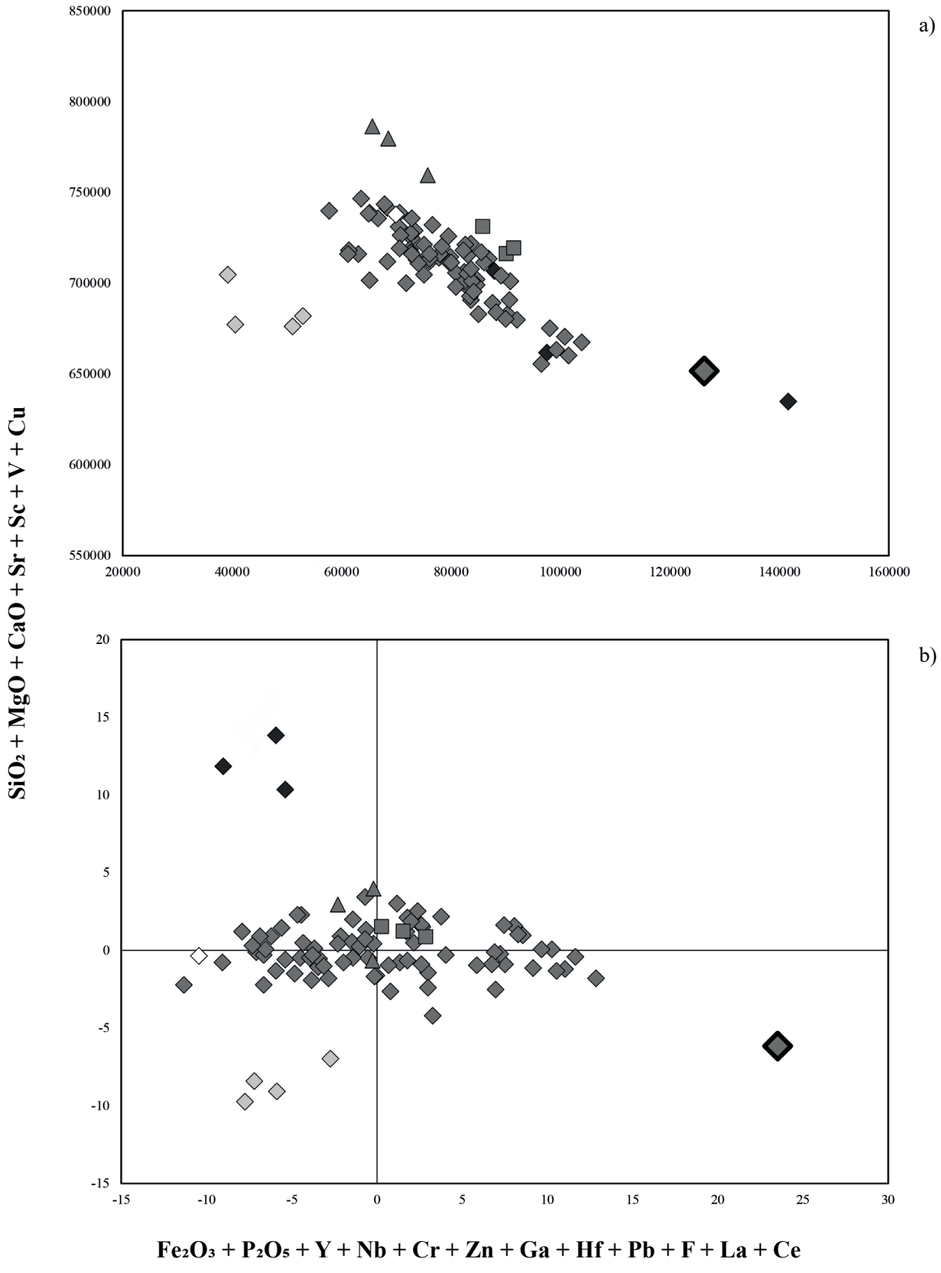

Fig. 28) Binary diagrams of CG-11 chemical data: a), ppm data; b), standardised data. Black rhombus, PT-Dioritic gnesiss inclusion; dark grey rhombus, PT-Granodioritic gnesiss inclusions; light grey rhombus, PT-Granitic gnesiss inclusions; white rhombus, PT-Tonalitic gnesiss inclusions; dark grey square, PT-Granodioritic gnesiss + basalt inclusions; dark grey triangle, PT-Granodioritic gnesiss + limestone inclusions; highlighted marker, CG-11.

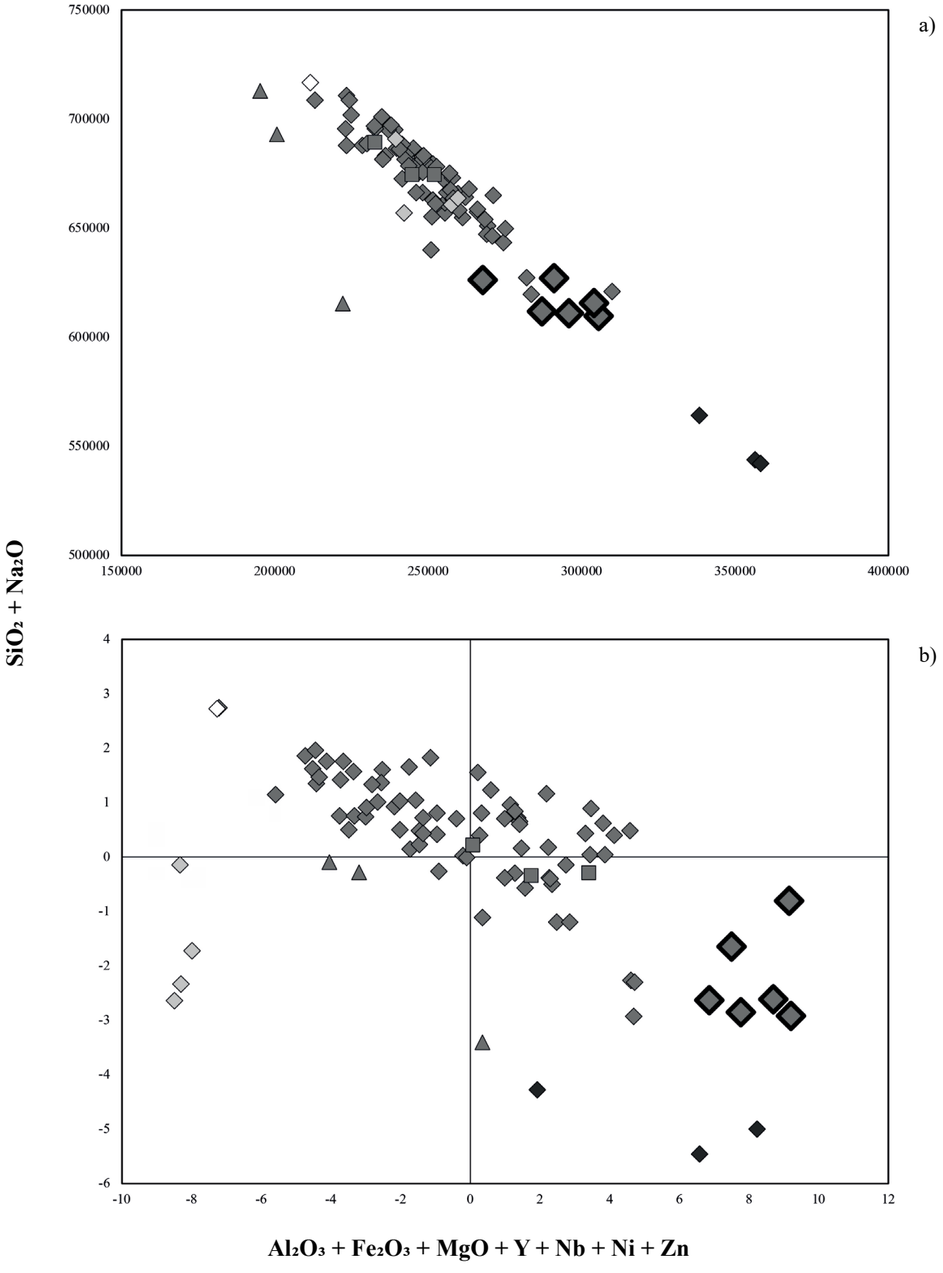

Fig. 29) Binary diagrams of CG-12 chemical data: a), ppm data; b), standardised data. Black rhombus, PT-Dioritic gnesiss inclusion; dark grey rhombus, PT-Granodioritic gnesiss inclusions; light grey rhombus, PT-Granitic gnesiss inclusions; white rhombus, PT-Tonalitic gnesiss inclusions; dark grey square, PT-Granodioritic gnesiss + basalt inclusions; dark grey triangle, PT-Granodioritic gnesiss + limestone inclusions; highlighted marker, CG-12.

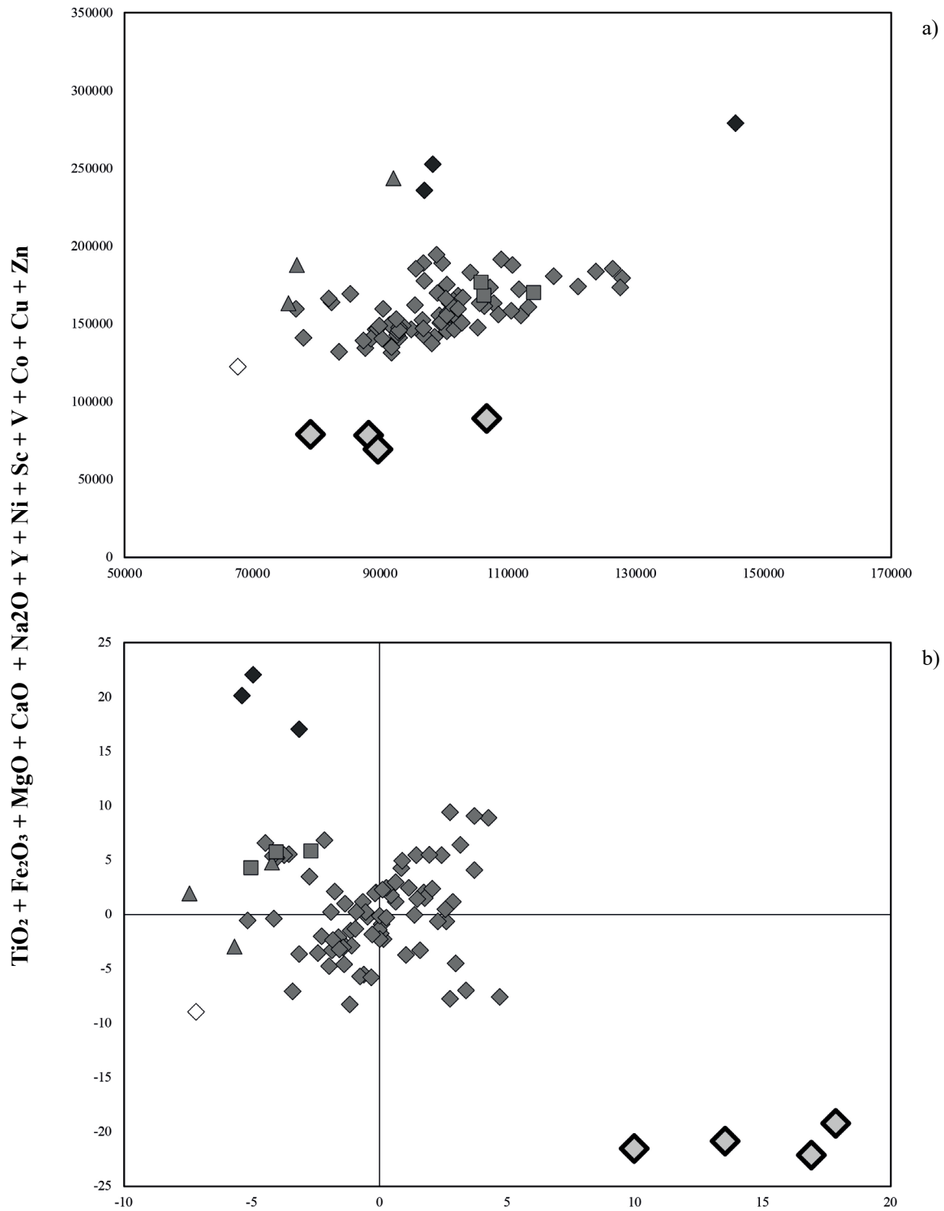

Fig. 30) Binary diagrams of CG-13 chemical data: a), ppm data; b), standardised data. Black rhombus, PT-Dioritic gnesiss inclusion; dark grey rhombus, PT-Granodioritic gnesiss inclusions; light grey rhombus, PT-Granitic gnesiss inclusions; white rhombus, PT-Tonalitic gnesiss inclusions; dark grey square, PT-Granodioritic gnesiss + basalt inclusions; dark grey triangle, PT-Granodioritic gnesiss + limestone inclusions; highlighted marker, CG-13.

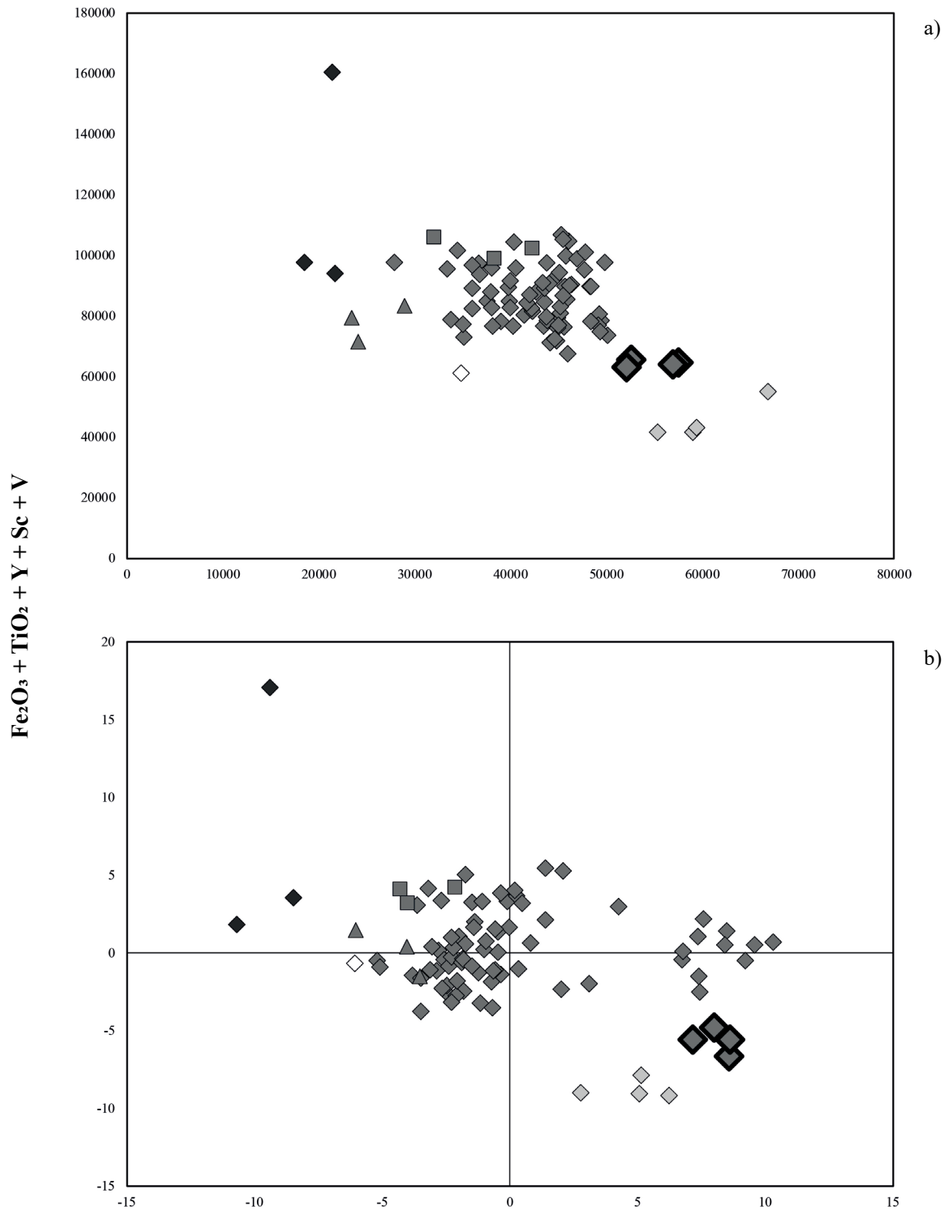

Fig. 31) Binary diagrams of CG-14 chemical data: a), ppm data; b), standardised data. Black rhombus, PT-Dioritic gnesiss inclusion; dark grey rhombus, PT-Granodioritic gnesiss inclusions; light grey rhombus, PT-Granitic gnesiss inclusions; white rhombus, PT-Tonalitic gnesiss inclusions; dark grey square, PT-Granodioritic gnesiss + basalt inclusions; dark grey triangle, PT-Granodioritic gnesiss + limestone inclusions; highlighted marker, CG-14.

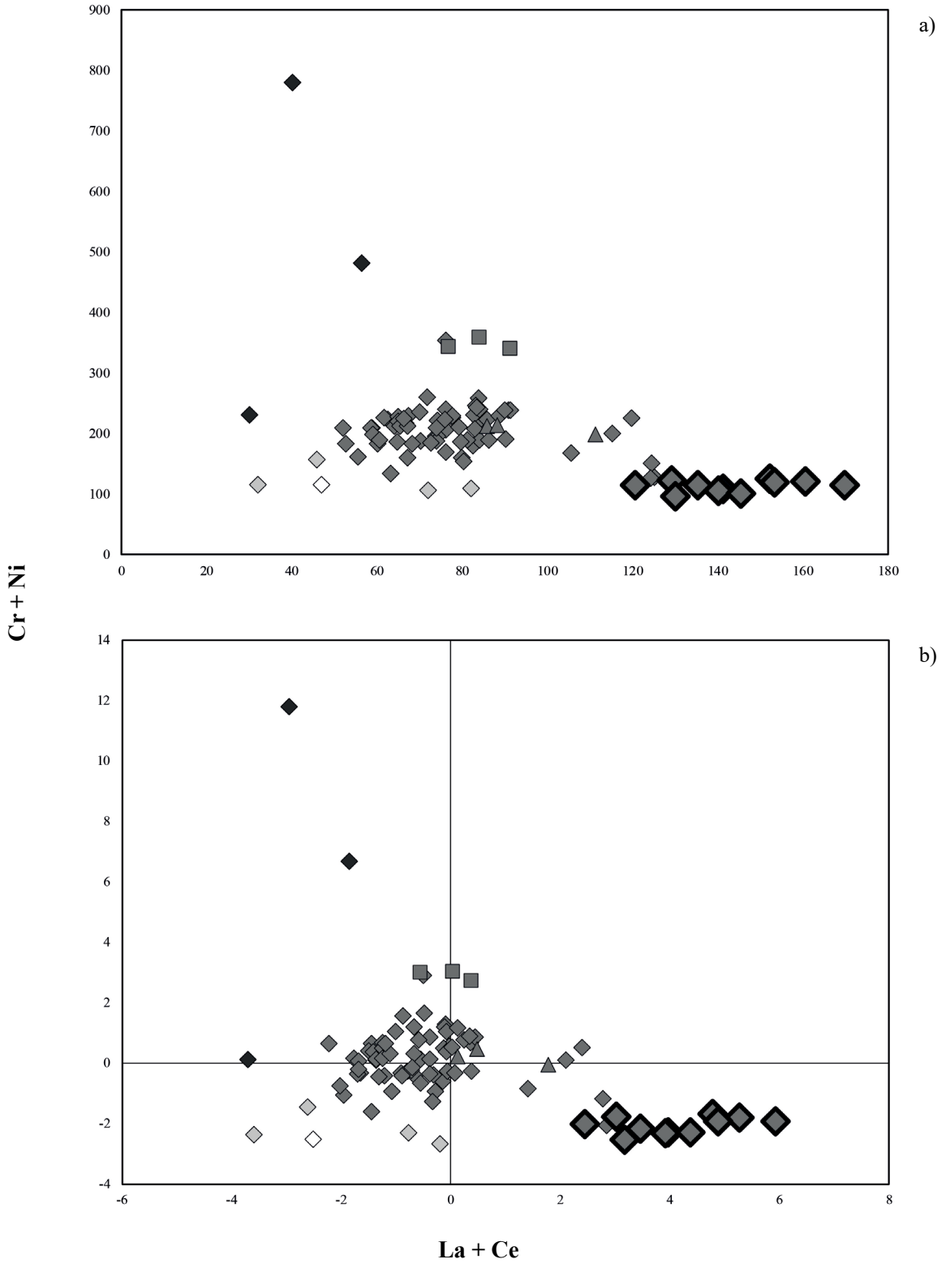

Fig. 32) Binary diagrams of CG-15 chemical data: a), ppm data; b), standardised data. Black rhombus, PT-Dioritic gnesiss inclusion; dark grey rhombus, PT-Granodioritic gnesiss inclusions; light grey rhombus, PT-Granitic gnesiss inclusions; white rhombus, PT-Tonalitic gnesiss inclusions; dark grey square, PT-Granodioritic gnesiss + basalt inclusions; dark grey triangle, PT-Granodioritic gnesiss + limestone inclusions; highlighted marker, CG-15.

Of the 90 samples, only a narrow, but at the same time representative selection, was conveniently analysed in order to derive its $^{87}Sr/^{86}Sr$ and $^{143}Nd/^{144}Nd$ isotope ratios. Overall, the samples fall within the ranges of 0.704178 - 0.715227 for $^{87}Sr/^{86}Sr$ and 0.512474 - 0.512735 for $^{143}Nd/^{144}Nd$ (Fig. 34; Tab. 6).

I will consider the granodioritic gneiss inclusion petrographic group as a point of reference in the following description.
Among the samples belonging to the latter petrographic group and those belonging to the dioritic gneiss inclusion one, with the exception of sample SEG6-4 ($^{87}Sr/^{86}Sr$ = 0.704178 and $^{143}Nd/^{144}Nd$ = 0.512654), there is not a real distance defined, but rather a progression of the granodioritic gneiss inclusion petrographic group towards dioritic gneiss inclusion one and therefore towards lower $^{87}Sr/^{86}Sr$ values. Indeed, samples belong to the last petrographic group, together with sample UA50-2-2, which belongs to the first one, show the lower $^{87}Sr/^{86}Sr$ values (Fig. 34; Tab. 6).

A trend towards such values of $^{87}Sr/^{86}Sr$ was also recorded by the granodioritic gneiss with basalt inclusion petrographic subgroup (Fig. 34; Tab. 6), which, however, diverges from the above-mentioned petrographic groups by higher values of $^{143}Nd/^{144}Nd$ (Fig. 34; Tab. 6).

Considering only the samples from the granodioritic gneiss inclusion petrographic group, there are two groups divided by a significant difference in the values of $^{143}Nd/^{144}Nd$ (Fig. 34; Tab. 6). Indeed, the first one, consisting of samples JH1-7, JH1-10 and JH1-11, records lower values than the second, the latter consisting of the remainder excluding sample UA50-2-2 (Fig. 34; Tab. 6).

In the area occupied by the second group also falls sample UA50-4-19 ($^{87}Sr/^{86}Sr$ = 0.707001 and $^{143}Nd/^{144}Nd$ = 0.512571), belonging to the granodioritic gneiss whit limestone inclusion petrographic subgroup (Fig. 34; Tab. 6).

Higher values of $^{143}Nd/^{144}Nd$ characterise the divergence of sample 4Bis-1 ($^{87}Sr/^{86}Sr$ = 0.706641 and $^{143}Nd/^{144}Nd$ = 0.512571), the only constituent of the tonalitic gneiss inclusion petrographic group, from the samples of the granodioritic inclusion petrographic group (Fig. 34; Tab. 6).

Finally, a strong divergence from the rest is characteristic of samples of the granitic gneiss petrographic group in which $^{87}Sr/^{86}Sr$ values increase significantly (Fig. 34; Tab. 6).

Tab. 6) $^{87}Sr/^{86}Sr$ and $^{143}Nd/^{144}Nd$ isotopic ratios data of the selected sampling.

Sample	Site	Petrographic Group	Chemical Group	$^{87}Sr/^{86}Sr$ meas	2σ	$^{143}Nd/^{144}Nd$ meas	2σ
SEG6-4	SEG6	PG-1	CG-1	0.704178	±0.000007	0.512654	±0.000005
UA50-4-21	UA50	PG-1	CG-2	0.704681	±0.000006	0.512512	±0.000005
1Bis-1	SEG6	PG-1	CG-2	0.705062	±0.000007	0.512592	±0.000004
UA50-2-2	UA50	PG-2	CG-3	0.704836	±0.000006	0.512557	±0.000005
UA50-1-15	UA50	PG-2	CG-4	0.706313	±0.000006	0.512581	±0.000005
UA50-4-19	UA50	SPG-1	CG-5	0.707001	±0.000006	0.512571	±0.000004
4Bis-1	ES2	PG-4	CG-6	0.706641	±0.000007	0.512735	±0.000005
KG23c-C2-26	KG23c	SPG-2	CG-8	0.705138	±0.000006	0.512728	±0.000004
KG23c-D3-13	KG23c	SPG-2	CG-8	0.705466	±0.000006	0.512725	±0.000004
AAS1-112	ASS1	PG-2	CG-10	0.706862	±0.000006	0.512588	±0.000004
KG23c-C2-13	KG23	PG-2	CG-10	0.706392	±0.000007	0.512581	±0.000005
JAG-1928	JAG1	PG-2	CG-12	0.707203	±0.000006	0.512564	±0.000004
3-1	JAG1	PG-2	CG-12	0.707405	±0.000006	0.512571	±0.000005
AAS1-203	ASS1	PG-3	CG-13	0.715227	±0.000007	0.512561	±0.000005
AAS1-201	ASS1	PG-3	CG-13	0.710782	±0.000006	0.512712	±0.000004
JH1-7	JH1	PG-2	CG-14	0.706407	±0.000007	0.512474	±0.000004
JH1-10	JH1	PG-2	CG-15	0.705537	±0.000007	0.512505	±0.000005
JH1-11	JH1	PG-2	CG-15	0.705214	±0.000006	0.512503	±0.000005

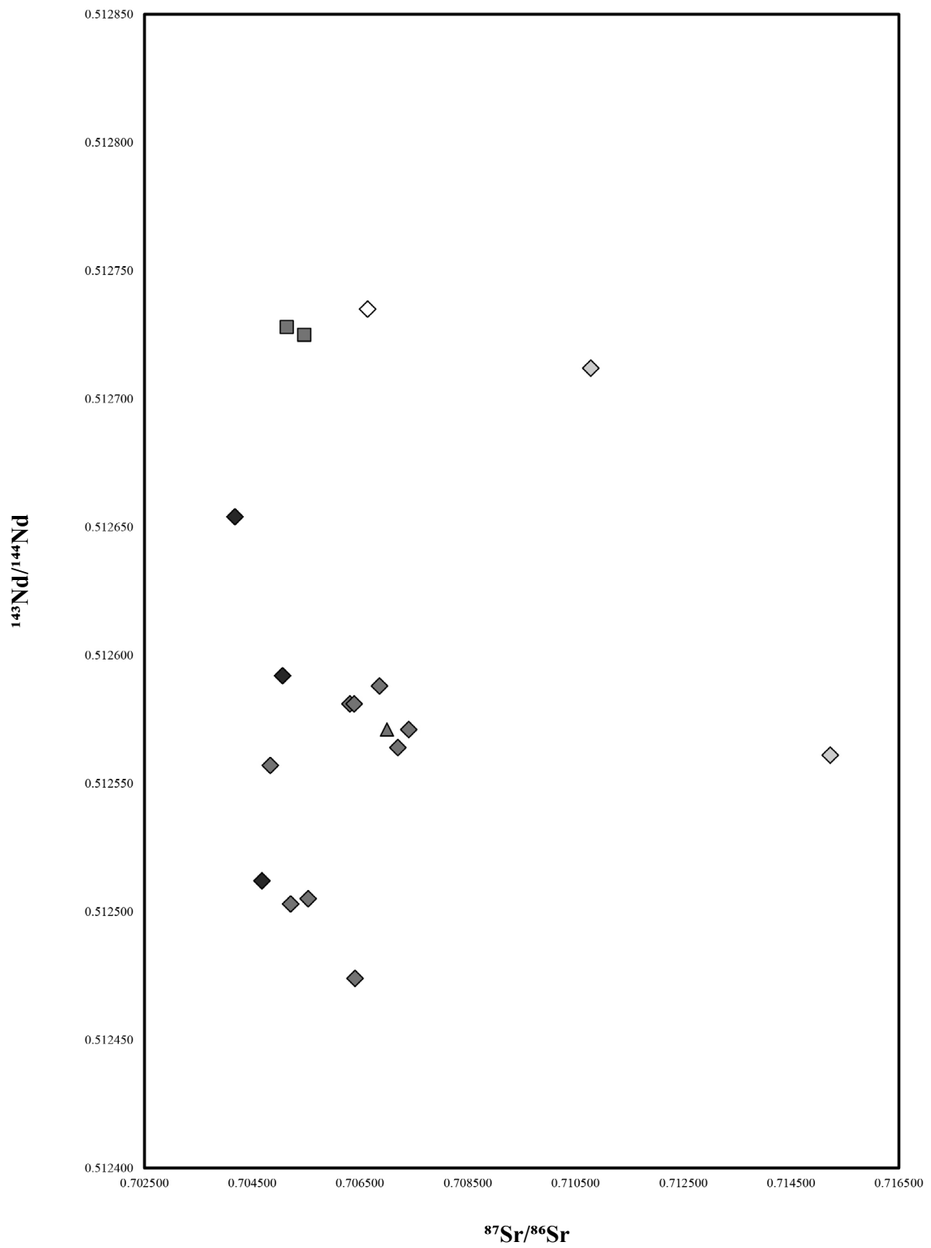

Fig. 34) $^{87}Sr/^{86}Sr$ versus $^{143}Nd/^{144}Nd$ binary diagram: Black rhombus, PT-Dioritic Gnesiss Inclusion; dark grey rhombus, PT-Granodioritic Gnesiss Inclusions; light grey rhombus, PT-Granitic Gnesiss Inclusions; white rhombus, PT-Tonalitic Gnesiss Inclusions; dark grey triangle, PT-Granodioritic Gnesiss + Basalt Inclusions; dark grey square, PT-Granodioritic Gnesiss + Limestone Inclusions.

5.3. Mineralogy and micro-structure

The qualitative mineralogical data of the samples obtained by X-ray powder diffraction, considering the mineralogical phases and the ratios of their relative abundances, strongly reflect the mineralogical variations determined by the firing processes. These variations can obscure the information relating to the raw materials used. For this reason, in studying diffractograms, information that may have been referred to firing processes is first excluded and then treated individually.

Petrographic evidence has shown that phyllosilicates (i.e. illite-muscovite, chlorite) in the ceramic body can fall either in the matrix or the inclusions fraction, in the latter case the amount of such minerals is considered negligible compared to the former. This involves that, in the diffractograms, the peaks referred to phyllosilicates depend almost exclusively on the contribution given by the matrix. Outside of this reasoning are samples AAS1-201 and AAS1-203, in which the amount of phyllosilicates as inclusions is not negligible, thus implying that the intensities of the peaks referring to these minerals also depend on the latter amount.

Only information useful for a provenance study will be discussed for the time being. Therefore, only the peaks referring to the mineralogical phases that occur as inclusions will be considered, as they mostly reflect the origin of the raw materials.

The processing of the qualitative mineralogical data identifies five mineralogical groups (MG) (MG-1, MG-2, MG-3, MG-4, MG-5), which do not provide a classification as defined by the chemical previous ones but reflect a tendency to emphasise petrographic one.

The most common mineralogical assemblage consists of, in decreasing order of relative abundances, quartz, plagioclase, k-feldspars and, in traces, Ca-amphiboles and epidote. The mineralogical group with the above-mentioned assemblage, called MG-1 (Fig.35), includes, with some exceptions, samples belonging to groups CG-10, CG-4, CG-9, CG-12, CG-7, CG-15, CG-14 and CG-11.

The phases present and their relative abundances ratios indicate a granodioritic assemblage, however slight differences can be observed among the samples belonging to this mineralogical group. Indeed, taking as reference the samples of the most populated group, CG-10, except 3Bis-1 and KG23c-C2-13 samples, those of the CG-4 group differ simply by a tendency to possess a quartz peak of higher intensity (Fig. 36). The CG-14 group, excluding sample JH1-7, diverge by a tendency towards increased K-feldspar and plagioclase (Fig. 35), while, samples from the CG -15 group, including sample JH1-7, preserve the ratios of relative abundances unchanged, but record an approximately two-fold increase in intensities (Fig. 35. These latter also showed a general increase in the CG -9 group and in the KG-23c-C2-13 sample, an increase which, however, was not two-fold and to which was added a specific increase in quartz intensities (Fig. 35). Similar behaviour to the CG -9 group samples is possessed by those of the CG-8 group, differing, however, in the occurrence of the reflection referred to clinopyroxenes and the decrease in the intensities referred to plagioclase peaks, which arrive at intensities like those present in the CG -10 group samples (Fig. 35). In the CG -5 samples, the significant difference between them and those of the CG-10 group is the occurrence of the peaks referring to calcite, which is accompanied by a slight decrease in the intensities referring to K-feldspars and plagioclase. Calcite peaks, although possessing much lower intensities, are recorded also in samples AAS1-158 and 5-1; the latter belonging to the CG-10 group. About the CG-7, CG-11 and CG-12 group samples, no differences were recorded. However, there is samples within the MG-1 mineralogical group, specifically in the CG-10 group.

From the MG-1 mineralogical group, which is considered the main one, given the number of samples constituting it, a divergence of the rest can be observed. In the MG-2 group, comprising the CG-3 samples and sample 3Bis-1, there is a clear increase in the intensities of the peaks referring to Ca-amphiboles and a strong decrease in k-feldspar (Fig. 37). This suggests a divergence from a granodioritic assemblage, proper to the MG-1 group, towards a dioritic one.

The intensities of the amphibole reflections increase significantly in the MG-3 group, consisting of the CG-1 and CG-2 samples. This group reflects an completely dioritic assemblage characterised in decreasing order of abundance by: amphibole, quartz, plagioclase and in trace amounts pyroxenes, both orthopyroxene and clinopyroxene, and k-feldspar (Fig. 38). The amphiboles fall mainly into the calcic family to which, in the SEG 6-4 sample, are added those of the Mg-Fe-Mn-Li family. Furthermore, in the latter sample, the intensities referring to epidote increase in contrast to the CG-2 group samples where it is in trace (Fig. 38).

In the GM-4 group, there is a inversion, compared to the GM-1 group, of the relative abundances between k-feldspars and plagioclases, thus defining a mineralogical assemblage characterised in descending order of abundances by: quartz, k-feldspar and plagioclase (Fig. 39). Mineralogical assemblage, the latter, resembling a granitic one. The mica like inclusion is only present in samples AAS1-201 and AAS1-203 (Fig. 39). Moreover, there is the absence of Ca-amphibole reflections with the exception of sample AAS1-157 (Fig. 39).

Finally, sample 4Bis-1, the only constituent of the MG-5 mineralogical group, diverges because it reflects an tonalitic assemblage constituted in decreasing order of abundance by quartz and plagioclase (Fig. 40).

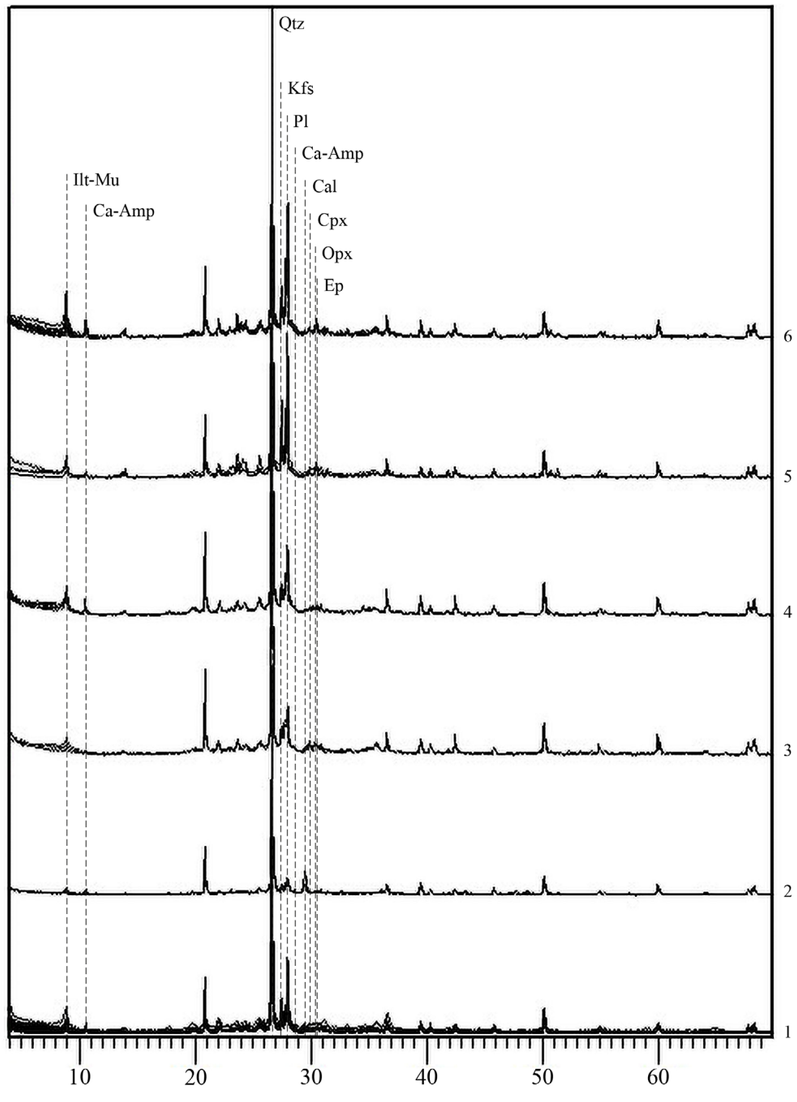

Fig. 35) XRPD patterns of MG-1 group samples: 1, CG-4/CG-7/CG-10/CG-11/CG-12; 2, CG-5; 3, CG-8; 4, CG-9; 5, CG-14; 6, CG-15. Mineral abbreviation (Whitney and Evans, 2010): Ca-Amp, calcic amphibole; Cal, calcite; Cpx, clinopyroxene; Ep, epidote; Ilt-Ms, illtite-muscovite; Kfs, k-feldspar; Opx, orthopyroxene; Pl, plagioclase; Qtz, quartz.

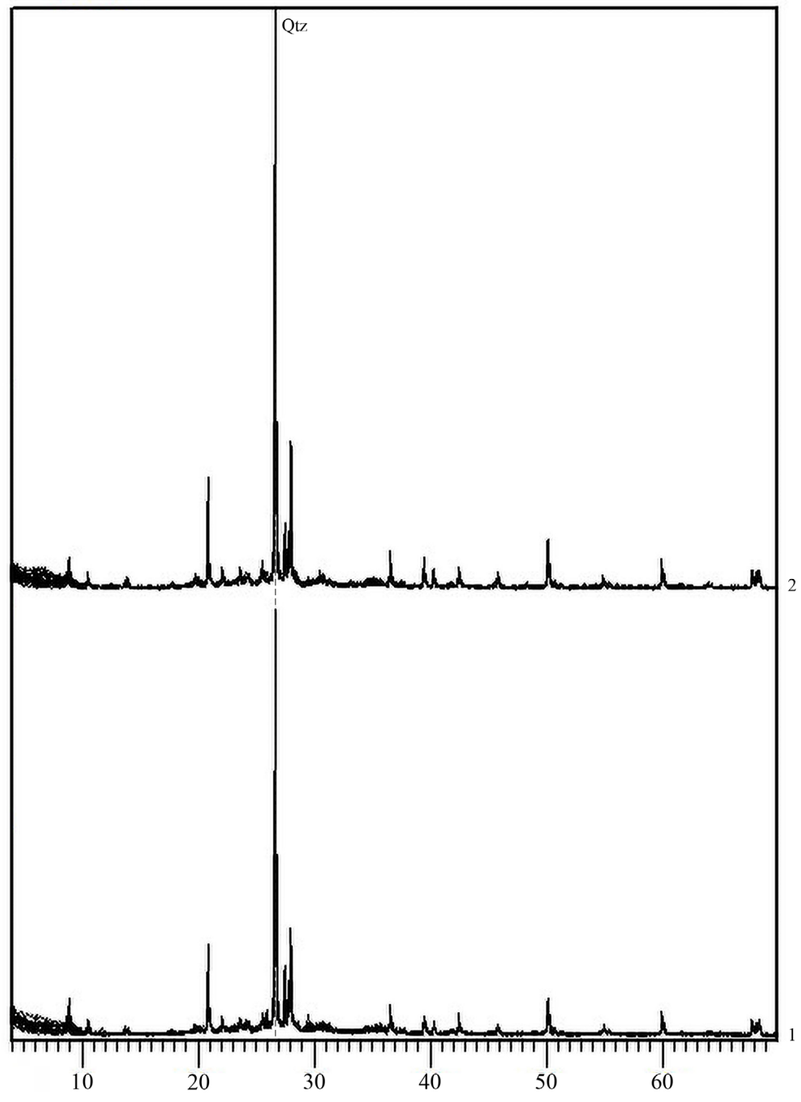

Fig. 36) XRPD patterns of CG-1o versus CG-4 group samples: respectively 1 and 2. Mineral abbreviation (Whitney and Evans, 2010): Qtz, quartz.

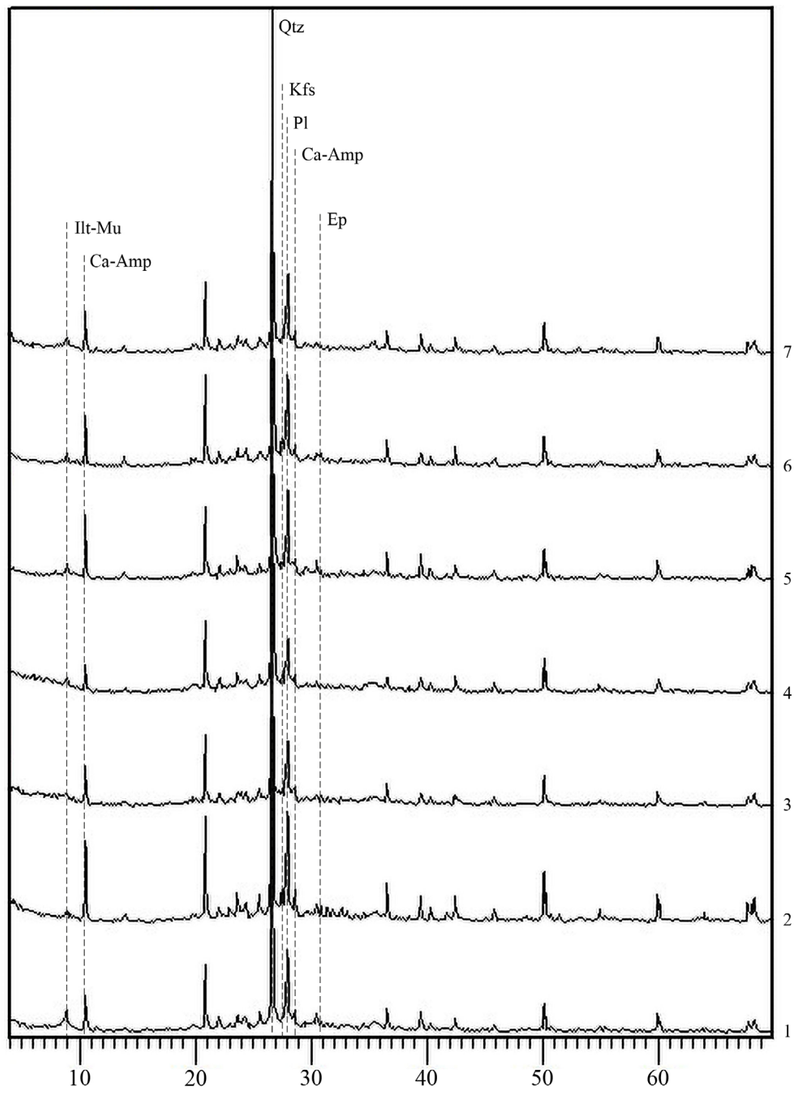

Fig. 37) XRPD patterns of MG-2 group samples: 1, UA50-2-1; 2, UA50-2-2; 3, UA50-2-3; 4, UA50-2-4; 5, UA50-3-5; 6, UA50-3-6; 7, UA50-4-26. Mineral abbreviation (Whitney and Evans, 2010): Ca-Amp, calcic amphibole; Ep, epidote; Ilt-Ms, illtite-muscovite; Kfs, k-feldspar; Pl, plagioclase; Qtz, quartz.

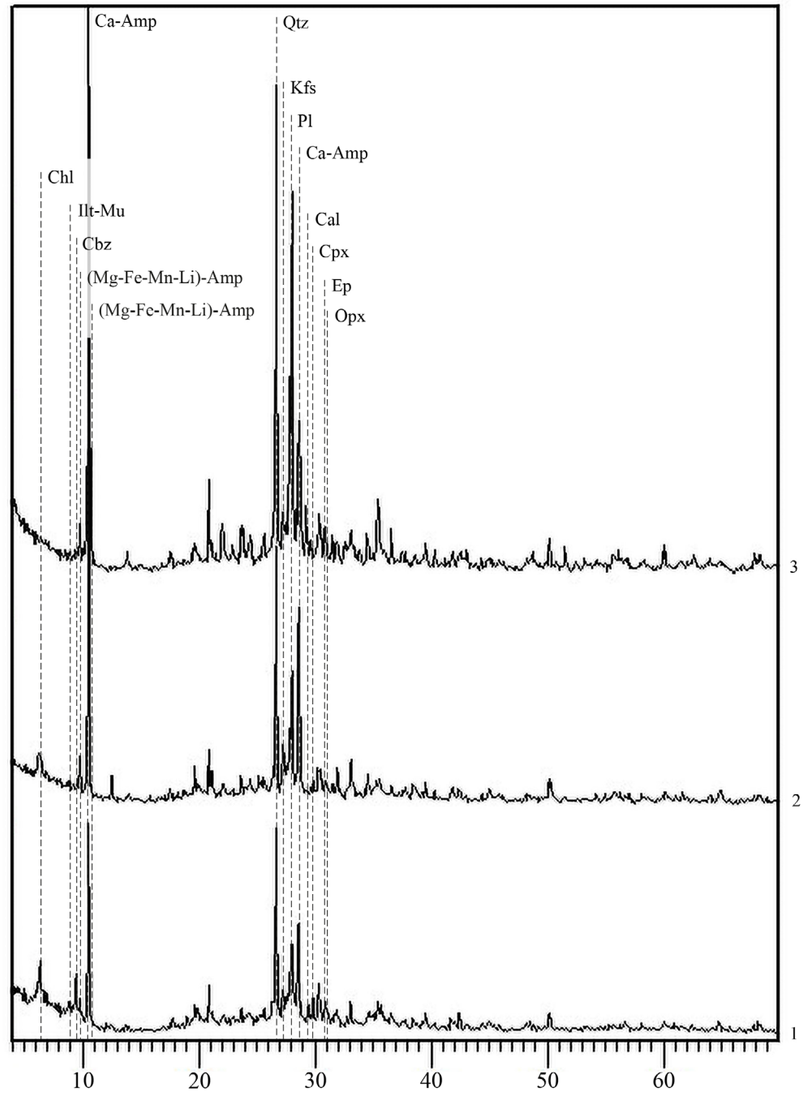

Fig. 38) XRPD patterns of MG-3 group samples: 1, UA50-4-21; 2, 1Bis-1; 3, SEG6-4. Mineral abbreviation (Whitney and Evans, 2010): Ca-Amp, calcic amphibole; Cal, calcite; Cbz, chabazite; Chl, chlorite; Cpx, clinopyroxene; Ep, epidote; Ilt-Ms, illtite-muscovite; Kfs, k-feldspar; (Mg-Fe-Mn-Li)-Amp, Mg-Fe-Mn-Li amphibole; Opx, orthopyroxene; Pl, plagioclase; Qtz, quartz.

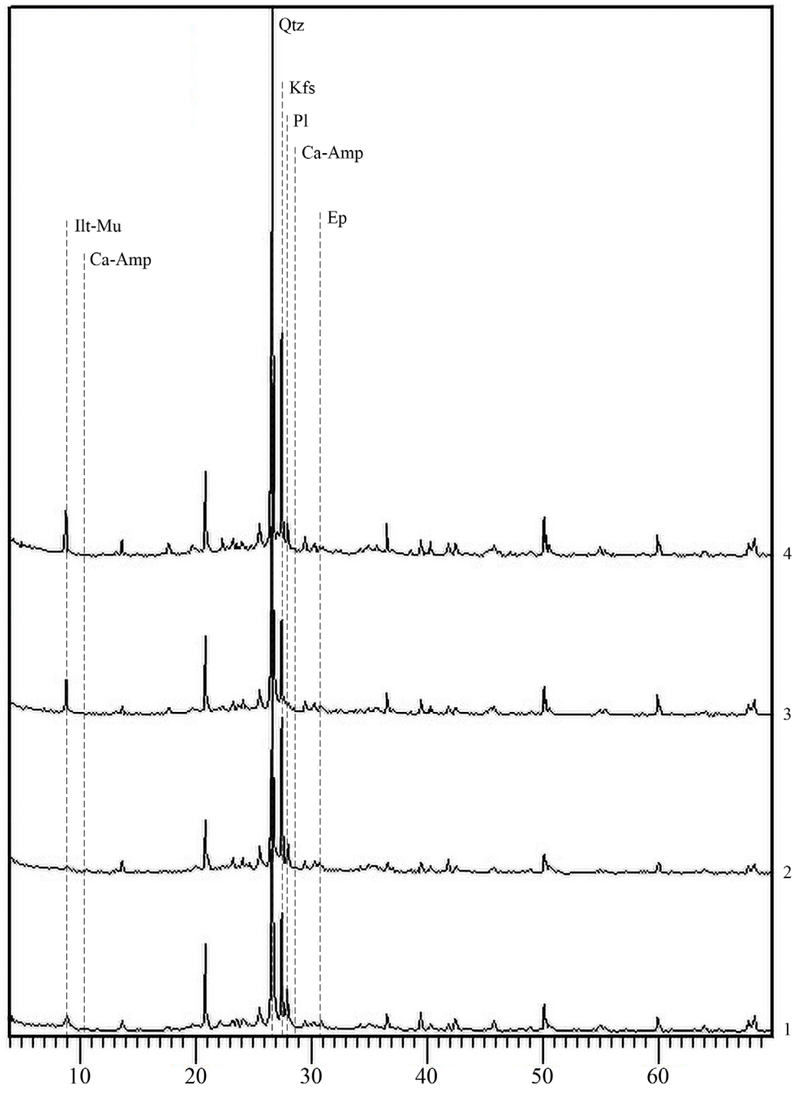

Fig. 39) XRPD patterns of MG-4 group samples: 1, AAS1-28; 2, AAS1-157; 3, AAS1-201; 4, AAS1-203. Mineral abbreviation (Whitney and Evans, 2010): Ca-Amp, calcic amphibole; Ep, epidote; Ilt-Ms, illtite-muscovite; Kfs, k-feldspar; Pl, plagioclase; Qtz, quartz.

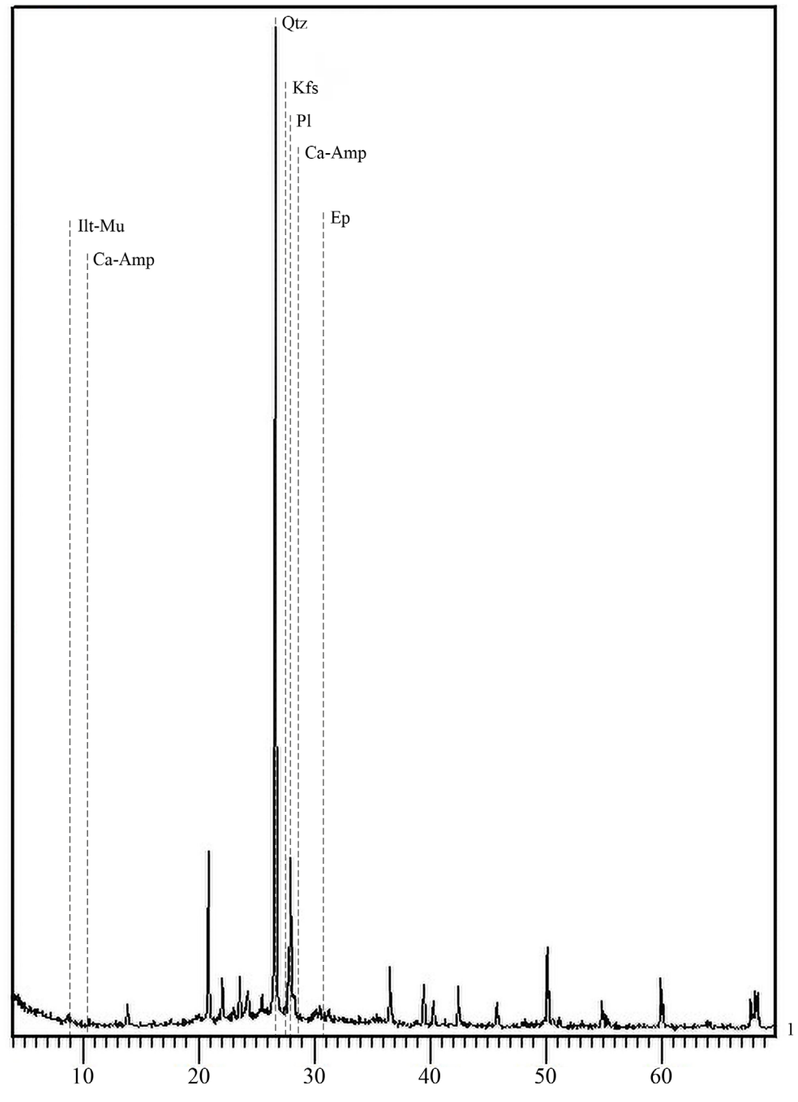

Fig. 40) XRPD pattern of sample 4Bis-1, the only constituent of the MG-5 group. Mineral abbreviation (Whitney and Evans, 2010): Ca-Amp, calcic amphibole; Ep, epidote; Ilt-Ms, illtite-muscovite; Kfs, k-feldspar; Pl, plagioclase; Qtz, quartz.

Mineralogical information strictly correlated with the transformations imparted by the firing process will be processed in a parallelism taking into account the study of microstructure.

In fact, by means of FESEM, an observation of the microstructure in fresh fracture and, consequently, of the possible occurrence of vitrification structures and, if so, of their degree, was carried out. In respect of the representativeness of the entire sampling, this observation was carried out on a selection of samples considered essential in defining the dynamics occurring in the firing process.

Note that the states of vitrification may exhibit the symbol + to indicate a transitional phase between the express vitrification structure and the subsequent one in temperature rise. This transitional phase indicates that in the sample the expressed vitrification structure occurs most frequently than the subsequent one, the latter present with varying degrees of occurrence (Maniatis and Tite, 1981; Maniatis and Tite, 1982). Moreover, it is to be highlighted the possible presence into the main vitrification structure of relict portions of the structure or structures preceding it in temperature decrease.

Furthermore, conscious of the temperature variation at which specific vitrification structures occur on the basis of the nature of the matrix, the non-calcareous (NC) nature of the matrices, specifically an illitic/micaceous nature, is reported. Only in a few samples the calcium oxide amount exceeds 6 wt. % mainly due to the presence of phases, covering the fraction of the inclusions, which trap it; phases such as calcic amphiboles (SEG6-4, UA50-4-21 and 1Bis-1) and calcite (UA50-3-10, UA50-4-19 and UA50-4-25) (Tab. 2; Tab. 5). This implies a non-widespread and non-immediate availability of calcium oxide than if it were trapped in the matrix's mineralogical phases. This condition leads to marking the matrix as unstable calcareous (C*) (Maniatis and Tite, 1981). However, even though in samples SEG 6-4, UA50-4-21 and 1Bis-1 the most significant contribution to the high calcium oxide content comes from calcic amphiboles, it is considered important to also report the secondary contribution from a chloritic component in the matrix in addition to the illitic/micaceous component; especially in sample 1Bis-1 (Tab. 2; Tab. 5).

Lastly, it is to be remembered that the occurrence of one structure rather than another also depends on the firing atmosphere; in fact, in a reducing (R) atmosphere, the occurrence of a specific vitrification structure takes place at temperatures 50°C lower than its occurrence in an oxidising (O) one (Muan, 1957; Naslund, 1976).

Following a description of the recorded vitrification structures regarding the rise in temperature until the maximum temperature, thus initially excluding processes related to the occurrence of dyschromia and therefore the change of atmosphere during firing processes.

Excluding the KG23c-C3-3 and 1C-1 samples, which show no vitrification (NV) (Fig. 41, a; Tab. 7), the first evidence of the effect of temperature on the matrix is recorded in the samples marked with the NV+ structure (Fig. 41, b; Tab. 7) (Maniatis and Tite, 1981; Maniatis and Tite, 1982). The latter is followed, in rising temperature, by the IV vitrification structure, reprsenting an initiation of vitrification. However, to this structure, escluding sample JH1-18, is always assigned the attribute + (Fig. 42; Fig. 43; Tab. 7) (Maniatis and Tite, 1981). From figure 42 to 43, the progressive approach of the IV+ structure to the characteristics of extensive vitrification can be observed. Only in sample AAS1-112 an extensive vitrification (V) is recorded, which also shows a low concentration of fine porosity (fb) (Fig. 44; Tab. 7) (Maniatis and Tite, 1981). The remaining samples show a continuous vitrification which in sample UA50-3-10 is devoid of porosity (Fig. 45; Tab. 7), in some is adorned with high concentrations of a fine porosity (FB) (0.2 - 4 µm diameter) (Fig. 46; Tab. 7), while in the remainder, there is also a medium porosity at low concentrations (mb) (2 - 10 µm diameter) (Fig. 47; Tab. 7) (Maniatis and Tite, 1981). In samples 1A-1, 3-1, 5-1 and JH1-18, which exhibit a CV (FB) vitrification structure, relicts of previous ones such as CV and V are present, and even IV in the case of the first sample (Fig. 48). The samples just reported are those where the presence of a relict structures is most evident.

To point out is the general tendency of higher-grade vitrification structwures, such as continuous vitrification having both fine and medium porosity, to occur more in samples belonging to the latest cultural groups (Tab. 7).

Tab. 7) Cooking conditions: maximum temperature reached and atmosphere. Where the symbol // is present it indicates that the reduced portion of the ceramic body was investigated first and then the oxidized portion.

Time Span (B.C.)	Site	Samples	CaO wt%	Clay type	Vetrification Stage	Firing Temperature (°C)
6000 - 5000	AAS 1	AAS1-201	1.27	NC	NV+ (R) // NV+ (R*)	≤750°C (R) // ≤750°C (R*)
6000 - 5000	AAS 1	AAS1-21	2.61	NC	IV+ (R)	750-850°C
6000 - 5000	AAS 1	AAS1-112	3.15	NC	V (fb) (R) // V (fb) (R*)	800-900 °C (R) // 800 - 900 °C (R*)
5000 - 4000	UA 50	UA 50 3 10	7.02	C*	CV (R*)	850-950°C (R*)
5000 - 4000	UA 50	UA 50 4 19	11.03	C*	NV+ (R*)	≤750°C (R*)
5000 - 4000	UA 50	UA 50 1 16	2.64	NC	IV+ (R) // IV+ (R*)	750-850 °C (R) // 750-850 °C (R*)
5000 - 4000	UA 50	UA 50 2 2	4.23	NC	IV+ (R) // NV+ (O)	750-850 °C (R) // ≤800 °C (O)
5000 - 4000	UA 50	UA 50 4 22	3.48	NC	IV+ (R) // IV (R*)	750-850 °C (R) // 750 -800 °C (R*)
5000 - 4000	UA 50	UA 50 4 21	6.67	C*	NV+ (O)	≤ 800°C (O)
4000 - 3000	KG 23	KG 23c C2 13	2.5	NC	CV (FB) + mb (R) // CV (FB) + mb (R*)	850-950°C (R) // 850-950°C (R)
4000 - 3000	KG 23	KG 23c C3 3	2.55	NC	NV	<750°C
4000 - 3000	KG23	KG 23c D1 17B	2.35	NC	NV+ (R)	≤ 750°C
2700 - 2300	GEG	5-1	5.16	NC	CV (FB) (R) // CV (FB) (R*)	850-950°C (R) // 850-950°C (R*)
2700 - 2300	JAG 1	1E-1	2.53	NC	CV (FB) + (mb) (R) / V (fb) (O)	850-950°C (R) // 850-950°C (O)
2300 - 2000	JH 1	JH1-7	3.07	NC	NV+ (R)	≤ 750°C
2300 - 2000	JH 1	JH1-18	3.1	NC	CV (FB) (R) /CV (FB) (R*)	850 - 950 ° C (R) // 850-950°C (R*)
2300 - 2000	JH 1	JH1-25	3.02	NC	NV+ (R) // NV+ (R*)	≤ 750°C
2300 - 2000	JH 1	JH1-28	3.04	NC	IV (R) // NV+ (O)	750-800°C (R) // ≤800 °C (O)
2300 - 2000	JAG 1	JAG 1928	3.31	NC	CV (FB) + (mb) (R) / V (fb) (O)	850-950°C (R) // 850-950°C (O)
2300 - 2000	SEG 7	3Bis-1	3.93	NC	CV (FB) (R)	850-950°C
2300 - 1800	JAG 1	1C-1	2.89	NC	NV	< 750°C
2000 - 1800	JH 1	JH1-11	3.33	NC	CV (FB) + (mb) (R) // V (fb) (O)	850°-950°C (R) // 850°- 950°C (O)
2000 - 1800	JH 1	JH1-19	3.01	NC	CV (FB) + (mb) (R) // V (fb) + (O)	850°-950°C (R) // 850°- 950°C (O)
2000 - 1800	JAG 1	3-1	3.5	NC	CV (FB) + (mb) (R) / V (fb) (O)	850-950°C (R) // 850-950°C (O)
2000 - 1800	SEG 7	3D-1	2.95	NC	NV+ (R)	≤ 750°C
2000 - 1800	K2	1A-1	2.65	NC	CV (FB) (R) // CV (FB) (R*)	850-950°C (R) // 850-950°C (R*)
2000 - 1800	K2	1D-1	3.18	NC	CV (FB) (R) // CV (FB) (R*)	850-950°C (R) // 850-950°C (R*)
2000 - 1800	ES 2	4Bis-1	2.99	NC	IV+ (R)	750-850°C (R)

NV

a)

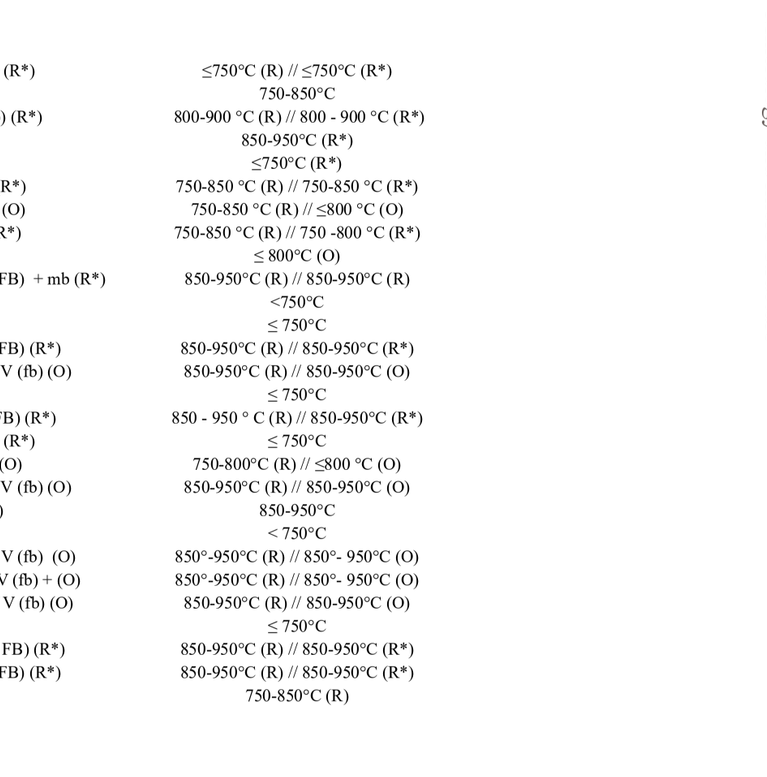

NV+

b)

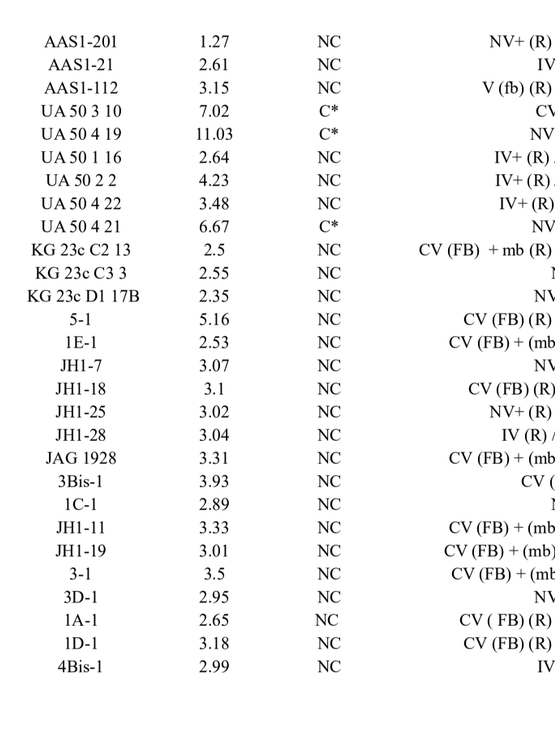

Fig. 41) FESEM microphotographs in fresh fracture. a) No vitrification structure (NV); KG23c-C3-3. b) Intermediate structure (NV+) between the no vitrification (NV) and initial vitrification (IV) ones; UA50-4-21. (Maniatis and Tite, 1981; Maniatis and Tite, 1982)

IV+

a)

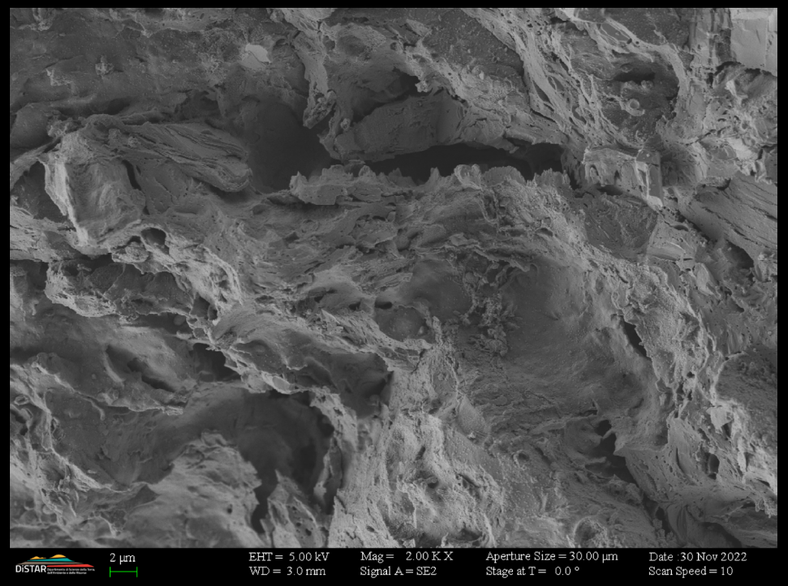

IV+

b)

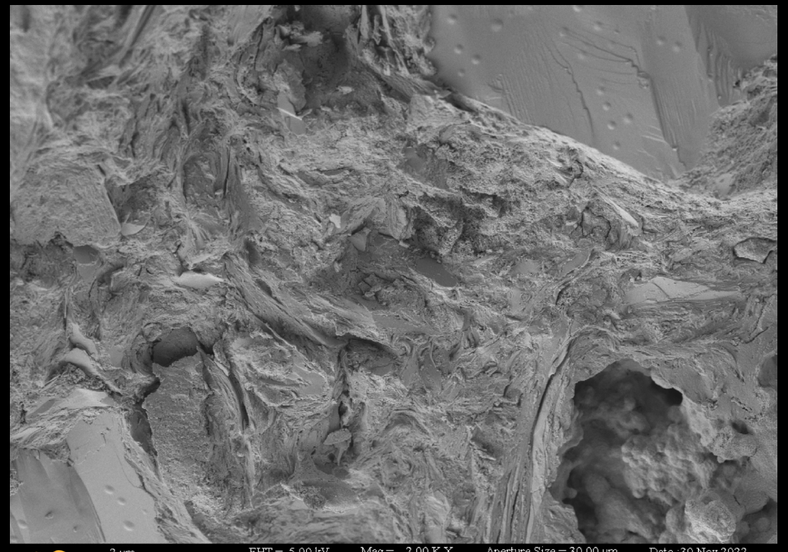

Fig. 42) FESEM microphotographs in fresh fracture. a-b) Intermediate structure (IV+) between the no initial vitrification (IV) and exstensive vitrification (V) ones; UA50-1-16 on the top, 4Bis-1 on the bottom. From the photo on the top to the one on the bottom, the progressive approach of the IV+ structure to the characteristics of extensive vitrification can be observed. (Maniatis and Tite, 1981)

IV+

a)

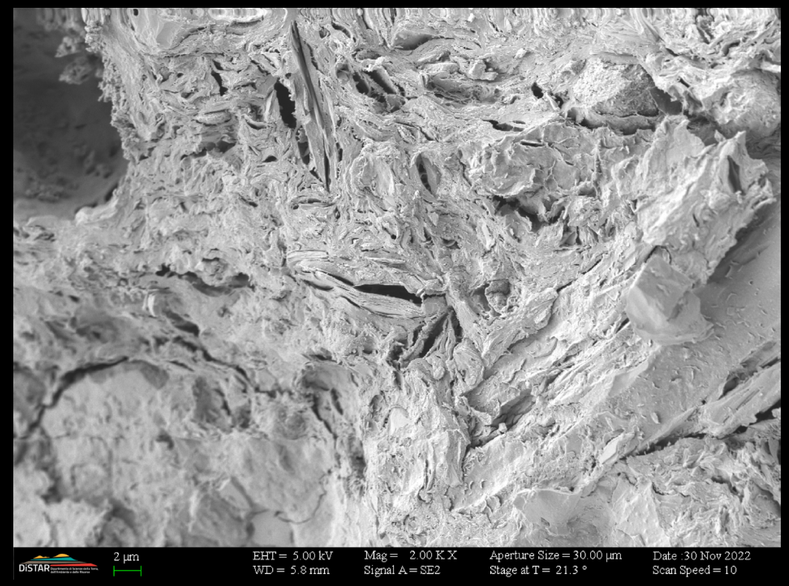

IV+

b)

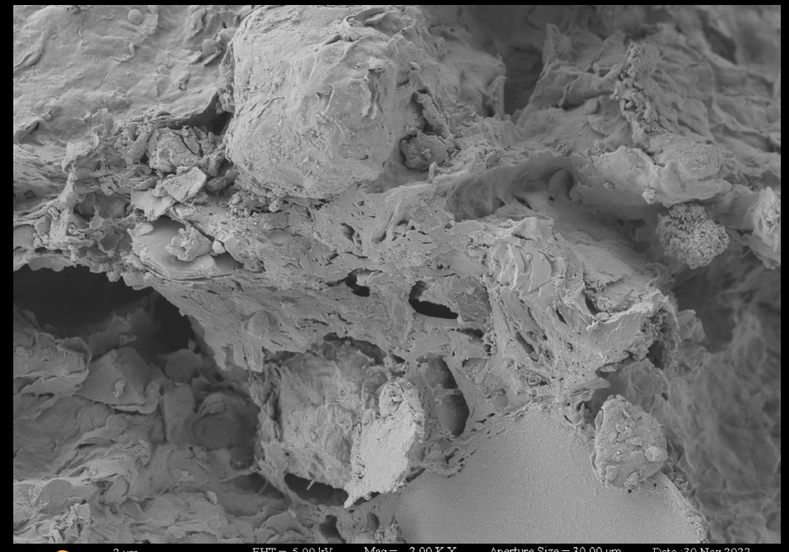

Fig. 43) FESEM microphotographs in fresh fracture. a-b) Intermediate structure (IV+) between the no initial vitrification (IV) and exstensive vitrification (V) ones; UA50-2-2 on the top, UA50-4-22 on the bottom. From the photo on the top to the one on the bottom, the progressive approach of the IV+ structure to the characteristics of extensive vitrification can be observed. (Maniatis and Tite, 1981)

V
(fb)

a)

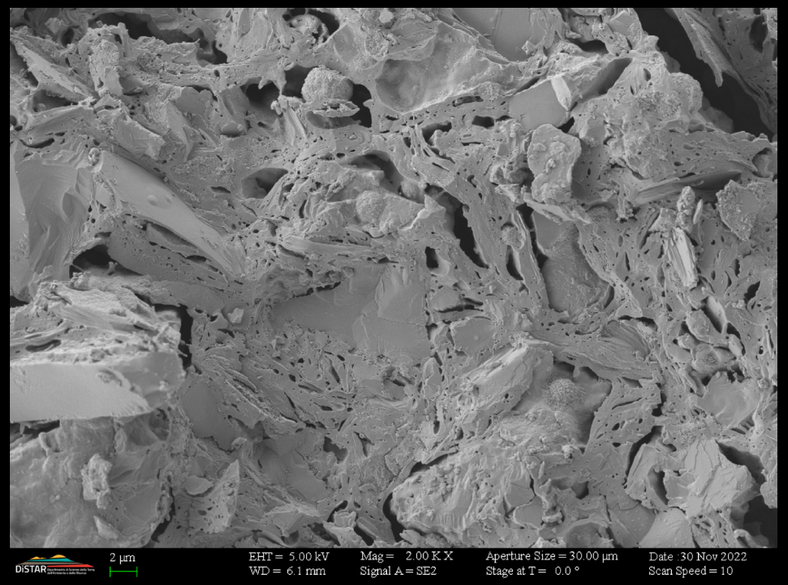

b)

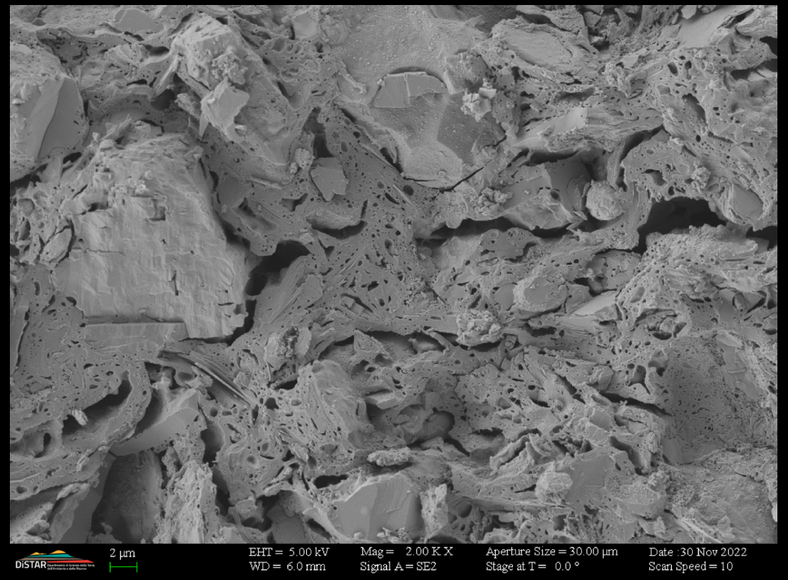

Fig. 44) FESEM microphotographs in fresh fracture. a-b) Exstensive vitrification structure (V) with low concentrations of a fine porosity (fb) (0.2 - 4 µm diameter); AAS1-112 on the top and on the bottom. (Maniatis and Tite, 1981)

CV

a)

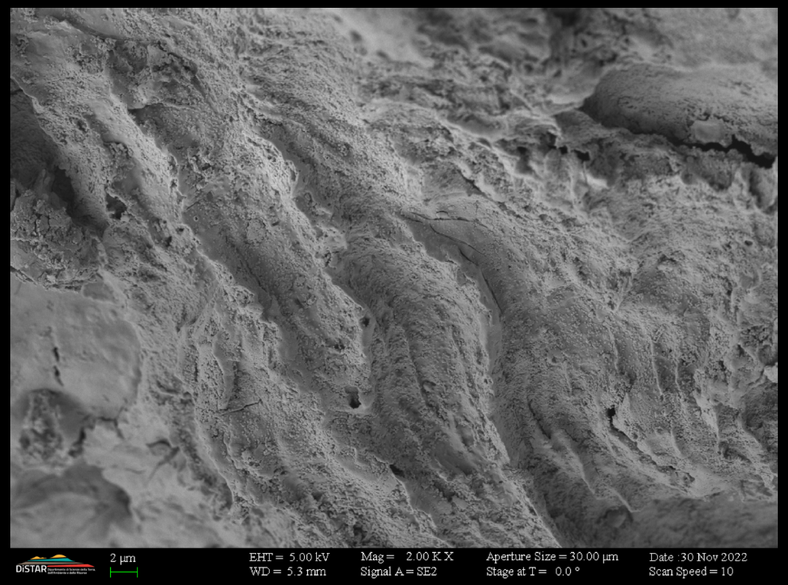

b)

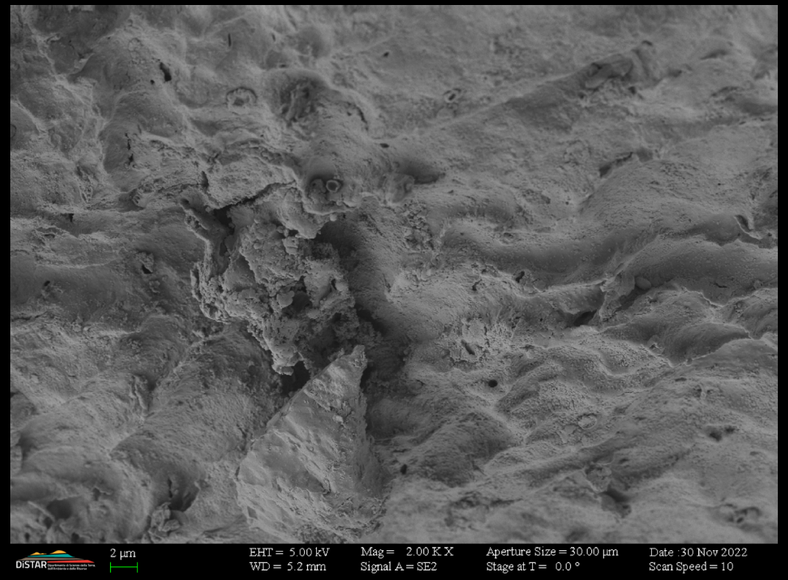

Fig. 45) FESEM microphotographs in fresh fracture. a-b) Continuous vitrification structure (CV); UA50-3-10 on the top and on the bottom. (Maniatis and Tite, 1981)

CV
(FB)

a)

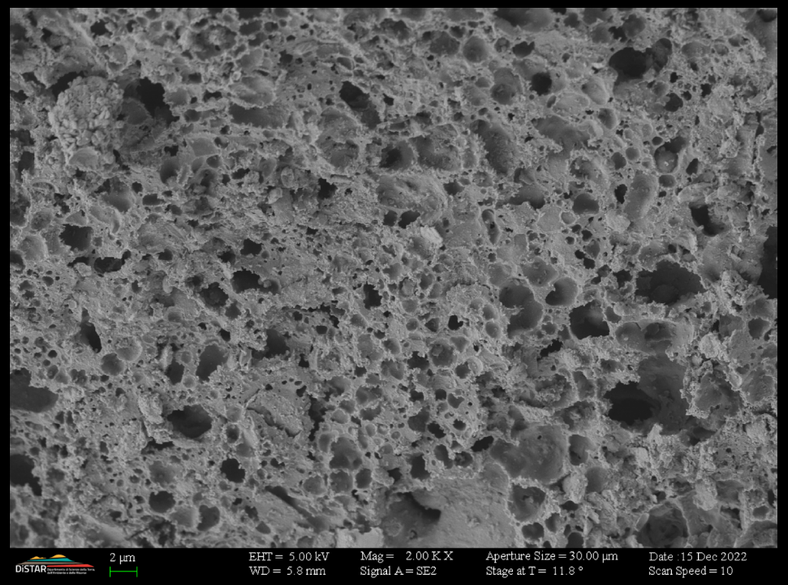

CV
(FB)

b)

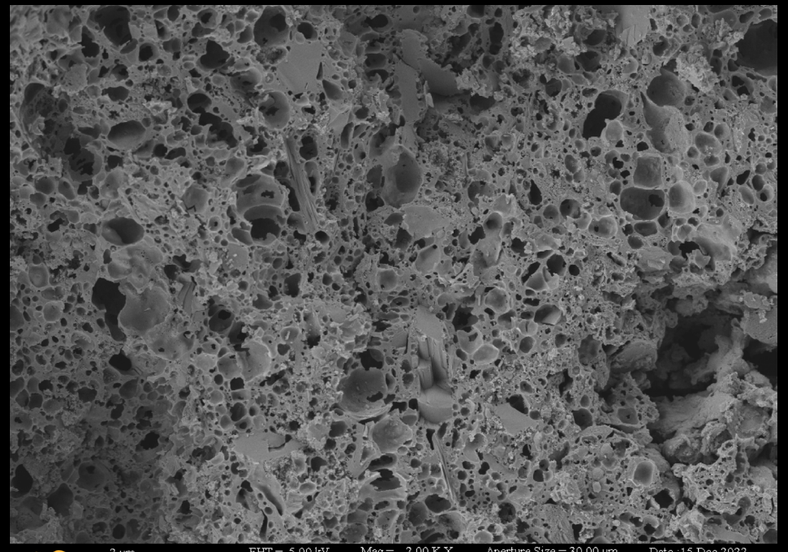

Fig. 46) FESEM microphotographs in fresh fracture. a-b) Continuous vitrification structure (CV) with high concentrations of a fine porosity (FB) (0.2 - 4 µm diameter); 1A-1 on the top, 5-1 on the bottom. (Maniatis and Tite, 1981)

CV
(FB)
+ mb

a)

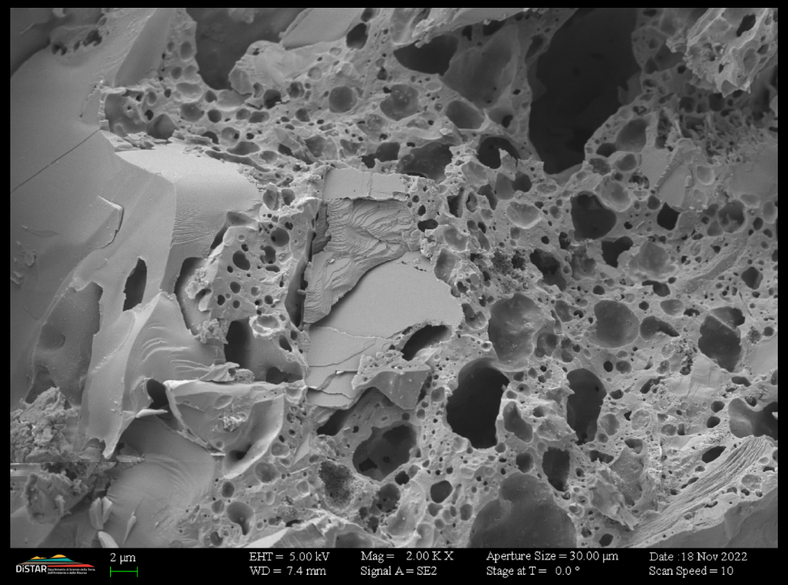

CV
(FB)
+ mb

b)

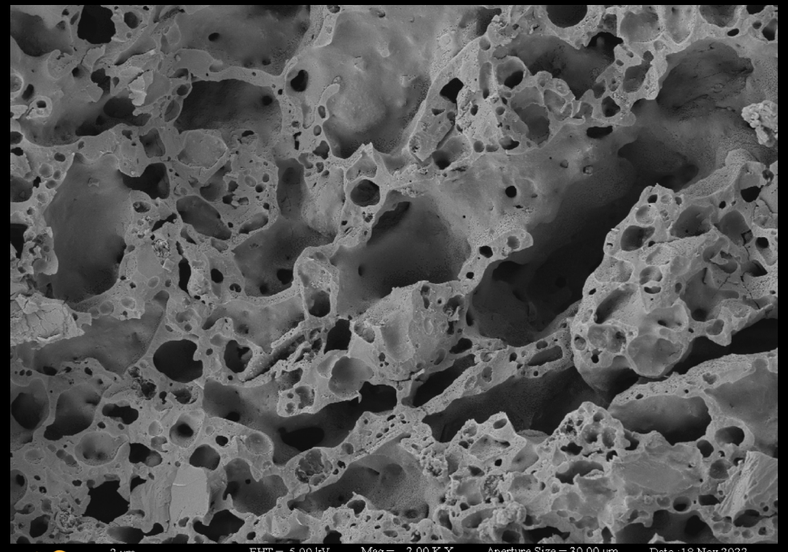

Fig. 47) FESEM microphotographs in fresh fracture. a-b) Continuous vitrification structure (CV) with high concentrations of a fine porosity (FB) (0.2 - 4 µm diameter) and a low concentration of medium porosity (mb) (2 - 10 µm diameter); JH1-19 on the top, KG23c-C2-13 on the bottom. (Maniatis and Tite, 1981)

a)

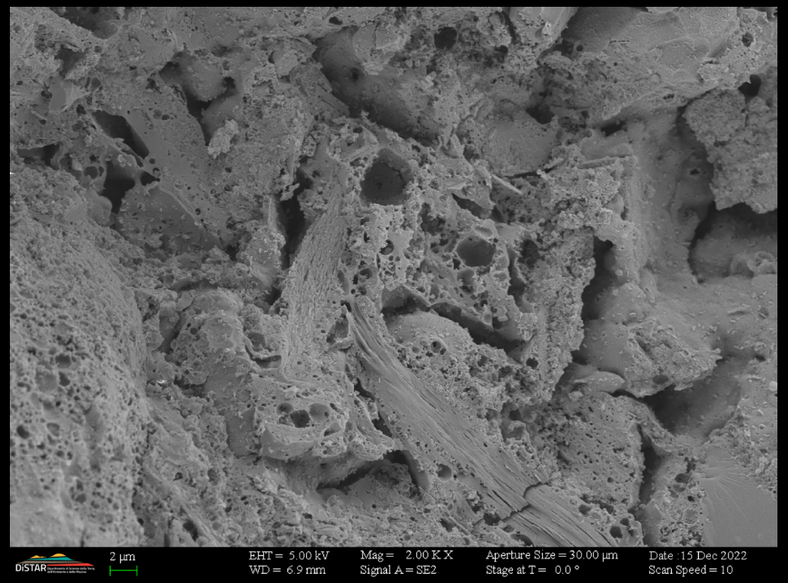

b)

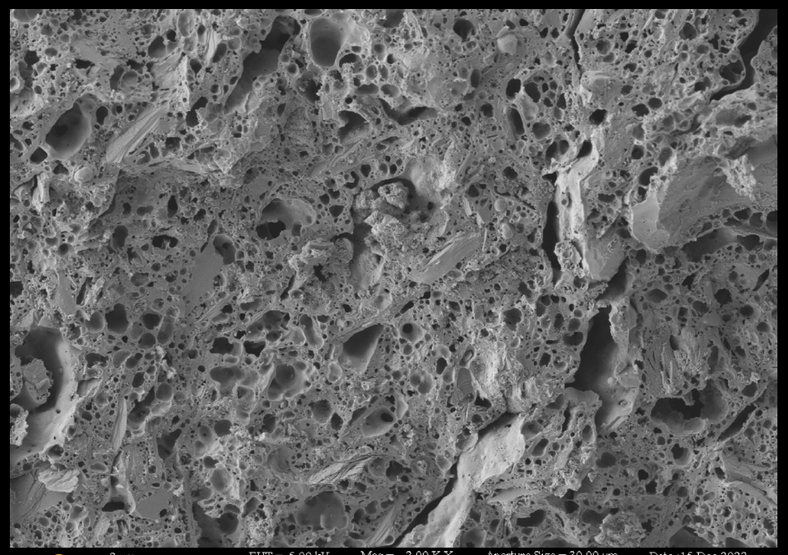

Fig. 48) FESEM microphotographs in fresh fracture. Relict structures. a) CV (FB) structure containing two relict ones: IV in the central portion and CV in the upper left; 1A-1. b) CV (FB) structure with islands of relict CV one; 3-1. (Maniatis and Tite, 1981)

At a later time, where conditions made it possible, for each sample the microstructure of its reduced portion was compared with one of its oxidised portion (Tab. 7). As stated above, dyschromia is generally blended and inhomogeneous and only in some samples they appear defined and homogenous.

In the first case, the samples show the same degrees of vitrification in both the reduced and oxidised portions (Fig. 49; Tab.7). Whereas, in the second case, there may be differences between the reduced and oxidised portions. In samples showing differences in the vitrification structures between the portions at different oxidation states, it can be seen that the oxidised portion exhibits a vitrification structure that precedes in degree one present in the reduced portion (Fig. 50; Fig. 51; Tab. 7); samples these mainly belonging to cultural groups of the latest dating. To point out is the occurrence, in the oxidised portions and where the vitrification structure allows, of both fine and medium porosity (Fig. 51, b; Tab.7). Please note that the occurrence of fine porosity or incipient porosity, which can also be expressed later in an oxidising environment, is characteristic of a reducing environment than an oxidising one (Maniatis and Tite, 1981).

(R)

a)

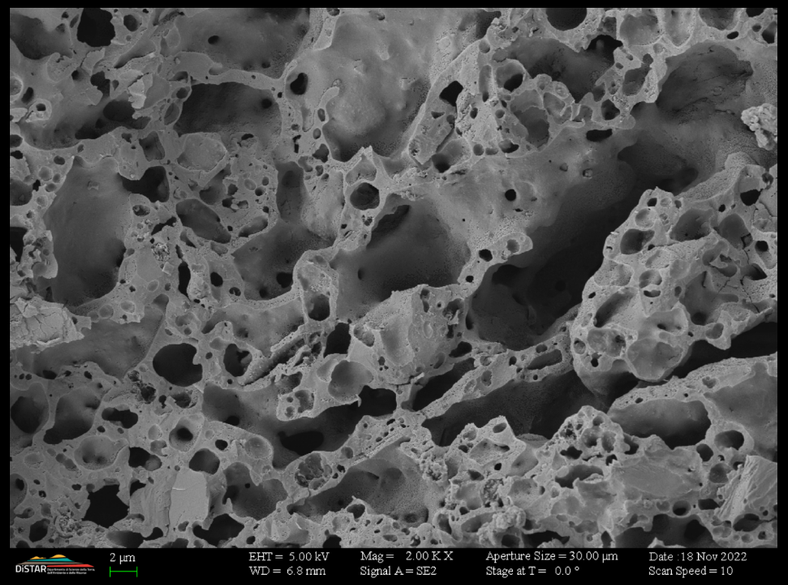

(O)

b)

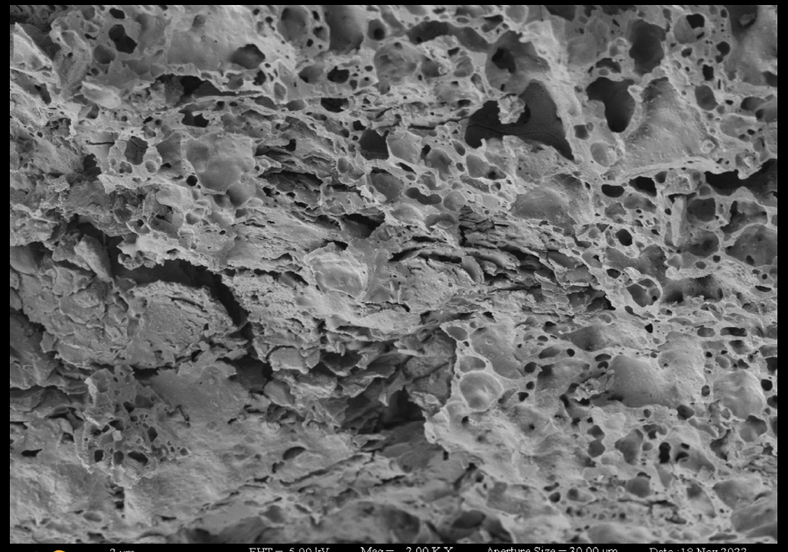

Fig. 49) Comparison between the vitrification structures respectively present in the reduced and oxidised portions of the same sample; KG23c-C2-12. a) Reducing portion (R) exhibiting CV (FB) + mb structure . b) Oxidising portion (O) exhibiting the same structure of reducing one. (Maniatis and Tite, 1981)

(R)

a)

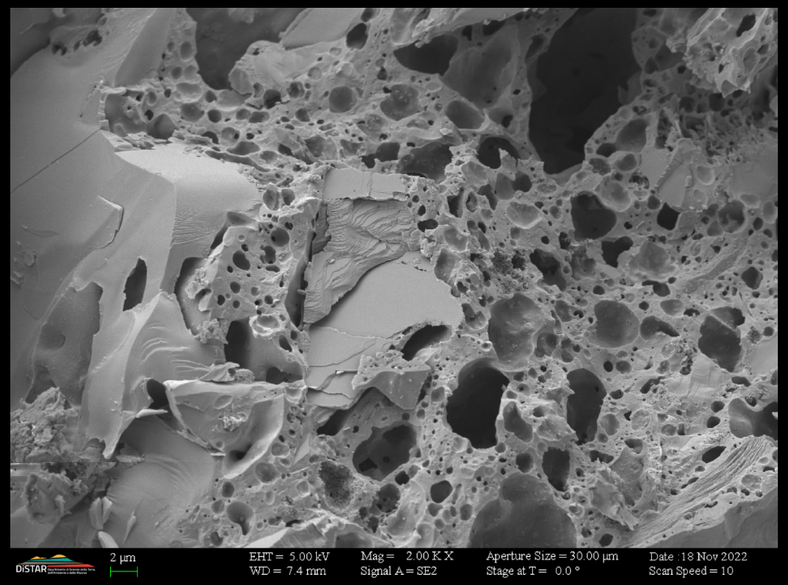

(O)

b)

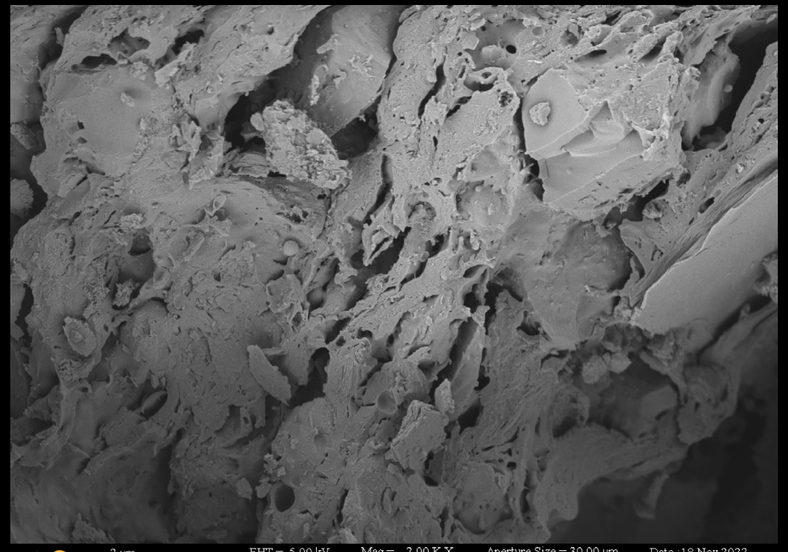

Fig. 50) Comparison between the vitrification structures respectively present in the reduced and oxidised portions of the same sample; JH1-19. a) Reducing portion (R) exhibiting CV (FB) + (mb) structure . b) Oxidising portion (O) exhibiting V (fb) + structure. (Maniatis and Tite, 1981)

(R)

a)

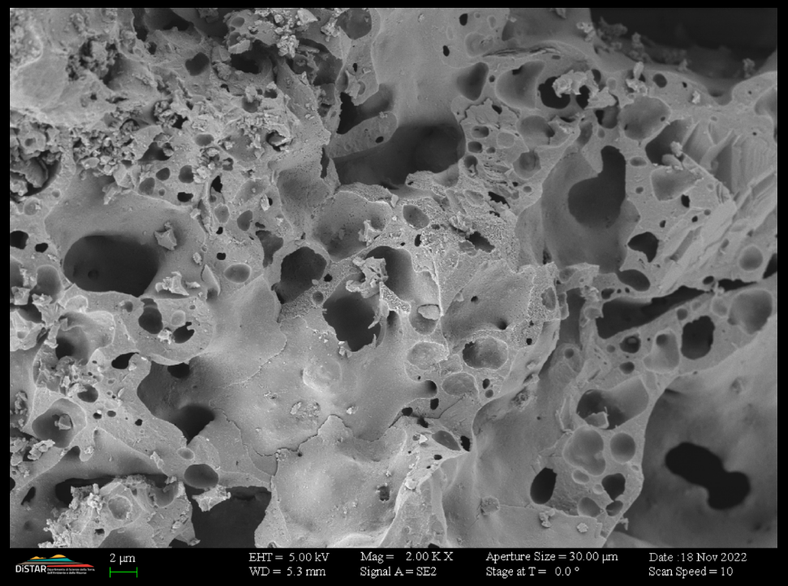

(O)

b)

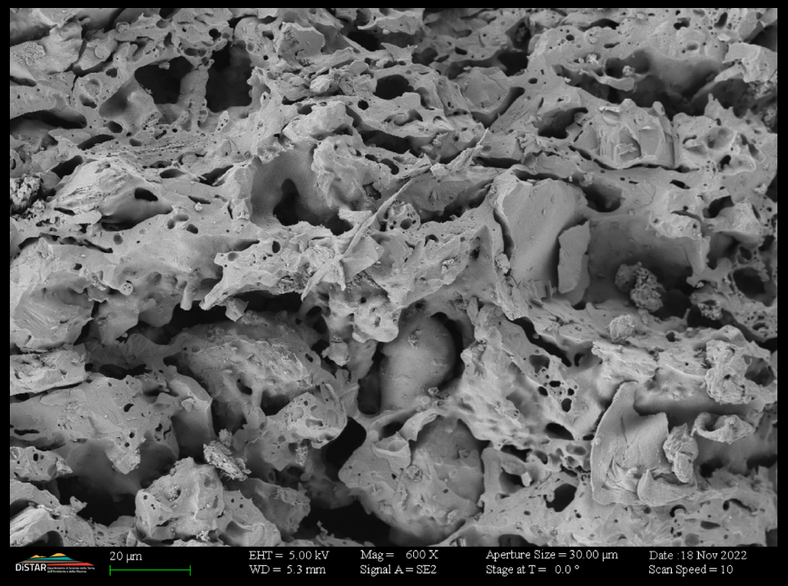

Fig. 51) Comparison between the vitrification structures respectively present in the reduced and oxidised portions of the same sample; JAG-1928. a) Reducing portion (R) exhibiting CV (FB) + (mb) structure . b) Oxidising portion (O) exhibiting V (fb) structure. (Maniatis and Tite, 1981)

Only in the samples (JAG-1928 and KG23c-C2-13) with a CV (FB) + mb (850-950°C) vitrification structure the absence of illite/mica is recorded (Fig. 52; Fig. 53). In the remaining samples with the same or lesser degree of vitrification, illite/mica is generally recorded, although with variable peak intensity (Fig. 52; Fig. 53). The variation in peak intensity of the latter phase tends to show, although irregularly, an inverse proportionality to increasing of the vitrification degree (Fig. 52; Fig. 53). Indeed, lower-grade vitrification structures may show lower illite/mica peaks intensities than those recorded in samples with more developed vitrification structures (Fig. 52; Fig. 53). Furthermore, it is necessary to note that samples with the same degree of vitrification and different matrix fraction amount may have similar illite/mica peak intensities (example) (Fig. 52; Fig. 53). In addition, in the matrices of samples UA 50 4 21, 1 Bis-1 and SEG 6-4, as mentioned above, not only the illite/mica phase is present, but also peaks related to chlorite are recorded (Fig. 52; Fig. 53).

There are samples that represent special cases. Into JH1-18 sample there is a slight bulge in the 2θ interval where the peaks referring to low-order clay minerals, such as smectite, occur; bulge, this, incoherent whit vetrification stage of the sample. While, in 4Bis-1, although a IV+ degree of vitrification is present, illite/mica is absent (Fig. 52; Fig. 53).

Moreover, the only samples that clearly show neoformation phases, specifically the latter referable to both trivalent Fe^{3+} (hematite) and bivalent Fe^{2+} (spinel) iron oxides, are: JH1-11, JH1-19, JAG-1928 and KG 23 23 C3 3 (Fig. 52; Fig. 53).

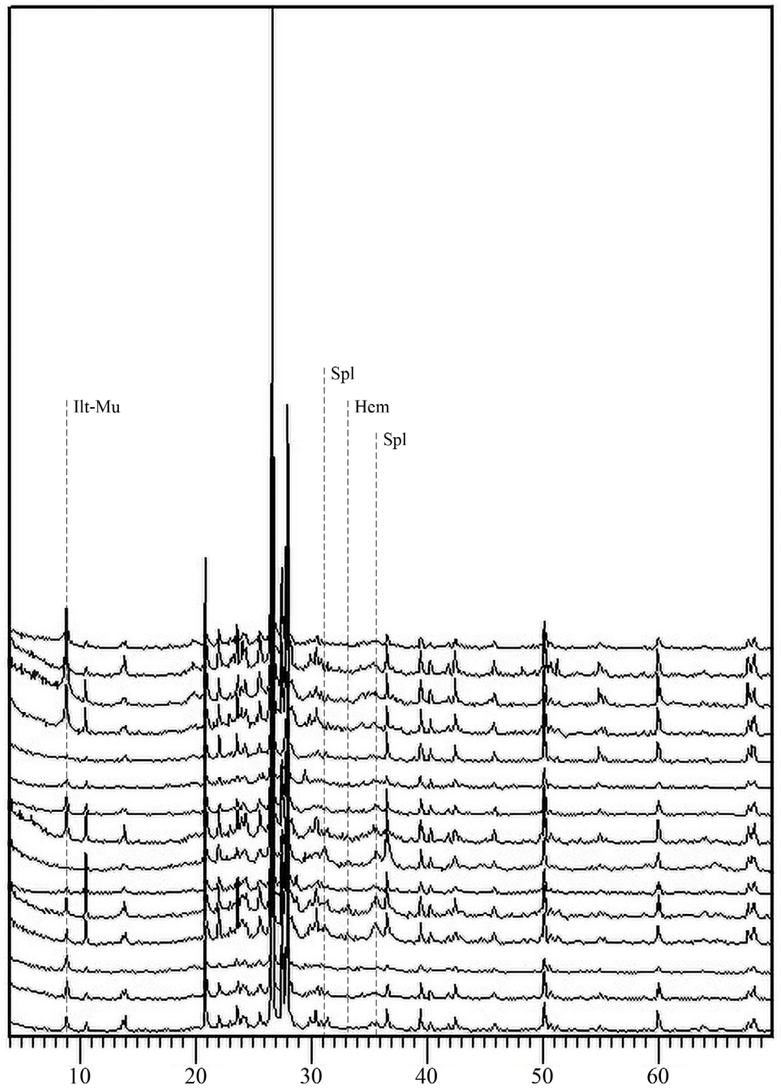

Fig. 52) XRPD pattern of the samples, dated in the 1800-2700 B.C. time span, of which the microstructure was investigated: 1, 1D-1; 2, 1A-1; 3, 3-1; 4, JH1-19; 5, JH1-11; 6, 3Bis-1; 7, JAG-1928; 8, JH1-18; 9, 1E-1; 10, 5-1; 11, 4Bis-1; 12, JH1-28; 13, JH1-25; 14, JH1-7; 15, 1C-1. Mineral abbreviation (Whitney and Evans, 2010): Hem, hematite; Ilt-Ms, illtite-muscovite; Spl, spinel.

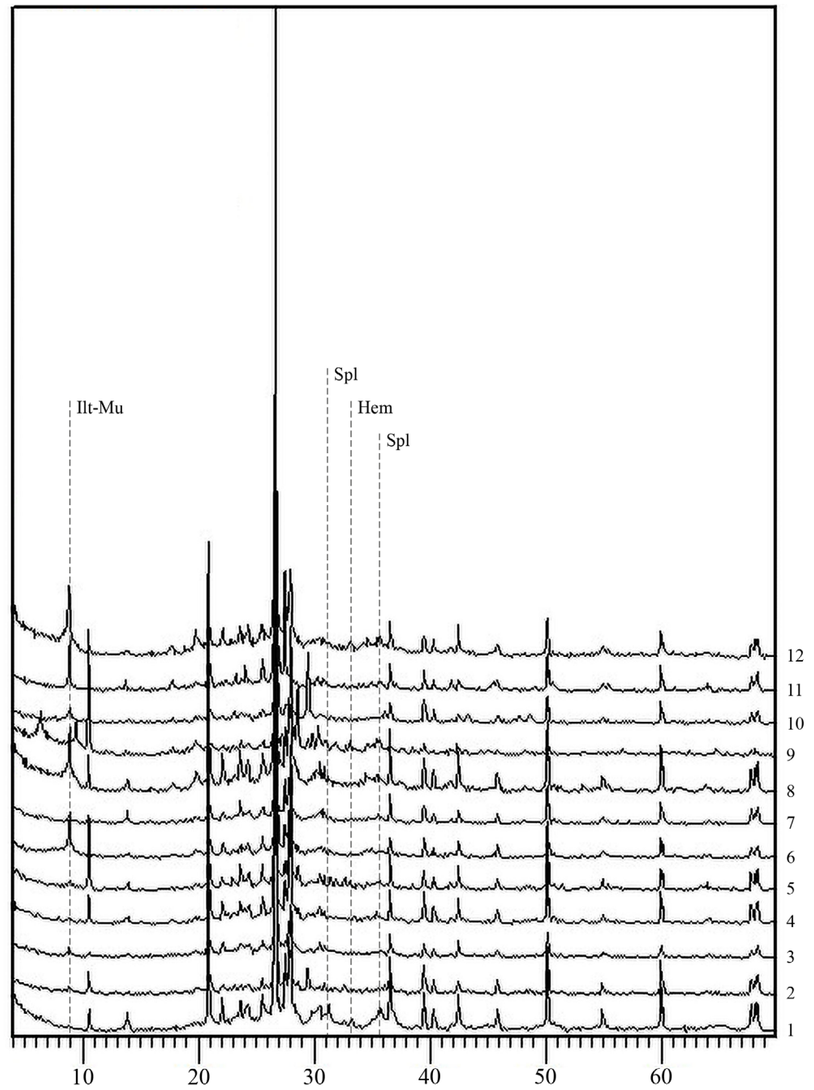

Fig. 53) XRPD pattern of the samples, dated in the 3000-6000 B.C. time span, of which the microstructure was investigated: 1, KG23c-C2-13; 2, UA50-3-10; 3, AAS1-112; 4, UA50-4-22; 5, UA50-2-2; 6, UA50-1-16; 7, AAS1-21; 8, KG23c-D1-17B; 9, UA50-4-21; 10, UA50-4-19; 11, ASS1-201; 12, KG23c-C3-3. Mineral abbreviation (Whitney and Evans, 2010): Hem, hematite; Ilt-Ms, illtite-muscovite; Spl, spinel.

6. Discussion

6.1. Raw materials: provenance and selection

In examining the various ceramic productions considered, the study of inclusions assumed a key role in defining the origin of the raw materials employed. The entire sampling was classified into four petrographic groups according to the nature of the inclusions (PT - dioritic gneiss inclusion, PT-1; PT - granodioritic gneiss inclusion, PT-2; PT - granitic gneiss inclusion, PT-3 and; PT - tonalitic gneiss inclusion, PT-4). Indeed, each of the groups contains inclusions, both lithic and loose mineralogical phases, resulting from the disintegration of a specific lithotype to which a secondary one can be marginally added, thus determining the definition of subgroups (SPT - granodioritic whit limestone inclusion, SPT-1 and; SPT - granodioritic whit basalt inclusion, SPT-2). The reconstruction of the nature of these lithotypes from the inclusions generated by their disintegration was essential in order to compare it, for the purpose of a provenance study, with that of the lithotypes occurring in the geological context of the area considered (Abbate, 2022; Andersson et al., 2006; Drury and De Souza Filho, 1998; Gabert, 1960; Geological & Mineral Resources Department (G. M. R. D. Khartoum - Sudan), 1981; Ghebreab, 1996 ; Ghebreab, 2005; Jhonson, 2021; Ruxton, 1956; Teklay, 1997; Vail, 1988).

As regards the fraction of inclusions in the petrographic groups, the nature of the mineralogical phases, both loose and aggregated in the lithics, and the structures recognised in the latter can be traced back to metamorphic lithotypes with magmatic protoliths. It will follow, in detail, the treatment of the best evidence from which significant information has been extracted that have allowed for definition of the nature of the lithotypes just mentioned. Initially, inclusions resulting from the disaggregation of secondary lithotypes characterising petrographic subgroups will be excluded.

The pyroxenes, where present (1Bis-1, UA50-4-21, SEG6-4), express both relict and metamorphic paragenesis, given the tendency respectively to high and low values of the $^{4}Al/^{6}Al$ ratio recorded in the pyroxenes, defining their origin as both magmatic and metamorphic; the latter origin being possible in medium-high metamorphic events (Deer, Howie and Zussman, 1997a; Spray, 1969; Winter, J.D., 2001) (Fig. 7). Grade this attributed by Drury and De Souza Filho, 1998 to the Barka sub-domain.

The pyroxenes of both natures are strongly altered and show a tendency to reorganise into amphiboles. The clinopyroxenes, which are augitic, show reorganisation into magnesiorneblende, which is stable in an amphibolite facies, and into actinolite, which is stable in one of the green schists (Fig. 4; Fig. 5, a-c, Fig. 6; Fig. 11; Tab. 3, Tab. 4) (Deer, Howie and Zussman, 1997a; Deer, Howie and Zussman, 1997c; Spray, 1969; Winter, 2001). In the latter facies, crystallisation of anthophyllite is also permitted at the expense of orthopyroxene, ferosilite (Fig. 5, d-f ; Fig. 6; Fig. 11; Tab. 3, Tab. 4) (Deer, Howie and Zussman, 1997a; Deer, Howie and Zussman, 1997c; Spray, 1969; Winter, 2001). These reorganisations can be distributed as rimes, portions and recrystallisations that follow the cleavage planes (Fig. 4; Fig. 5) (Spray, 1969; Winter, 2001). The fact that pyroxenes of a metamorphic nature also exhibit reorganisations, in phases that thermodynamically originate at a lower metamorphic grade than that in which pyroxenes originate, suggests a retrograde

metamorphic event (Spray, 1969; Winter, 2001).
The amphiboles themselves can express both a relict and metamorphic paragenesis; in fact, magnesiornblende and pargasite crystals of a magmatic nature reorganise into tshermakite, magnesiorneblende and pargasite, imposing an increase in the ^{6}Al content at the expense of ^{4}Al (Fig. 8, a-c; Fig. 9, a-c; Fig. 11; Fig. 13; Tab. 4); these reorganisations are stable under the thermodynamic conditions of the amphibolite facies (Deer, Howie and Zussman, 1997c; Spray, 1969; Winter, 2001). The above-mentioned amphiboles of both origins can be transformed into actinolite, anthophyllite and, to a lesser extent, into mica chlorite, phases which are typical of the green shale facies (Fig. 8, Fig. 9, d-f; Fig. 11; Fig. 12; Fig. 13; Tab. 4) (Deer, Howie and Zussman, 1997c; Spray, 1969; Winter, 2001). When the reorganisations characteristic of the green shale facies recur at the expense of the amphiboles formed in the amnfibolitic facies they suggest a retrograde metamorphic event (Spray, 1969; Winter, 2001). All of the above-mentioned reorganisations can be distributed as rim and/or portions at the expense of the phase from which they originate (Fig. 8; Fig. 9) (Spray, 1969; Winter, 2001). Amphiboles formed during the metamorphic event are the mineralogical phases that most closely record its evolution.

However, epidote and zoisite are also diagnostic minerals for evaluating the metamorphic grade because they are stable in the green shale facies and amphibolite one respectively (Fig. 8, d-f) (Deer, Howie and Zussman, 1997c; Spray, 1969; Winter, J.D., 2001).

The metamorphic event is also expressed by the various structures observed in the lithics: granoblastic, decussate, recrystallised quartz structures with irregular margins formed due to the bulging determined by the migration of grain boundaries and isoriented elongated quartz crystals (Fig. 10; Fig. 14, c-f; Fig. 16; Fig. 17, c-f) (Spray, 1969; Winter, J.D., 2001). Where the protolith becomes more sialic and there are no pyroxenes, amphiboles and epidotes in high amounts, it is the above-mentioned structures that express the metamorphic event the most.

Indeed, being aware of the existence of phases attributable to both a relict and a metamorphic component, both prograde and retrograde, and that the inclusions of each petrographic group strongly resemble the lithotype from whose disintegration they were generated, when examining the modes of the various mineralogical phases expressed in Tab. 2, it is evident that they significantly reflect the protolith assemblages (dioritic, granodioritic, granitic and tonalitic) of the metamorphic (gneiss) lithotypes.

All of this defines that the metamorphic lithotypes, the nature of which has been reconstructed, derive from magmatic protoliths with dioritic (PG-1), granodioritic (PG-2), granitic (PG-3) and tonalitic (PG-4) compositions subjected to regional metamorphism characterised by a progadic event in amphibolite facies followed by a retrograde event in green shale facies. These lithotypes have the same characteristics as those of the Barka sub-domain (Abbate, 2022; Andersson et al, 2006; Drury and De Souza Filho, 1998; Gabert, 1960; Geological & Mineral Resources Department (G. M. R. D. Khartoum - Sudan), 1981; Ghebreab, 1996 ; Ghebreab, 2005; Jhonson, 2021; Ruxton, 1956; Teklay, 1997; Vail, 1988) that are eroded by

the Gash and seasonal wadis that descend from the Eritrean Plateau downstream to the Southern Atbai Plain (Garzanti et al, 2006; Padoan et al., 2011) (Fig. 2). The result of their erosion characterises the fluvial deposits close to the studied archaeological sites; thus leading to the consideration of these deposits as possible supply sites for raw materials.

In terms of subgroups, the inclusions derived from the disintegration of a granodioritic gneiss are combined with those from limestone (SPG-1) and basalt (SPG-2) (Fig. 15). The chemistry of pyroxenes derived from the disintegration of basalts shows high values in the $^{4}Al/^{6}Al$ ratio, suggesting their obvious magmatic nature (Fig. 7; Fig. 15, c-d; Tab. 3) (Deer, Howie and Zussman, 1997a).

The reason for the presence of these secondary lithotypes always derives from a supply reason. Indeed, samples with inclusions from the disintegration of basalts are found in the proximity of the Atbara River, which cuts the Continetal Flood Basalt formation (Pik, 1997; Garzanti et al., 2006; Padoan et al., 2011). The Atbara deposits contaminate those of the older palaeochannels of the Gash, partially overlapping them (Garzanti et al., 2006; Padoan et al., 2011). With regard to the samples with limestone fragments, they present a significant concentration of lithics of this lithotype, leading them to fall into a subgroup. However, other samples also present limenestone lithics but not in significant quantities. This is due to the possible widespread occurrence in the area of this lithotype.

From Padoan et al., 2011, the $^{87}Sr/^{86}Sr$ and $^{143}Nd/^{144}Nd$ isotope ratios of the Gash and Abara sediments were collected to compare with those of the samples. It can be seen from the diagram that there is an affinity between the samples from the archaeological sites located along the current Gash channel and the Gash sediments. Whereas, for the samples from archaeological sites located near the Atbara and belonging to the granodioritic inclusion + basalt inclusions subgroup, there is a tendency towards an affinity with the sediments of the latter watercourse.

Increasing the degree of detail, the isotope ratios of a sediment sample from the possible supply site in the vicinity of site JH1 were also plotted in the diagram. Note how the samples from a specific site are close to the sediments from the same site.

Thus, the occurrence of one petrographic group rather than another at a specific archaeological site depends on the spatial distribution of the fluvial deposits in the area, on which lithotype the river course, which generates the deposit under consideration, cuts and erodes, and on the degree of transport. In detail, this occurrence depends on the nature of the deposit or deposits in the vicinity of the archaeological site under consideration. Moreover, sites with the same petrographic group may show differences between them, suggesting even more the locality of the supply

The latter statement is well demonstrated by the cluster analysis carried out on the chemical attributes of the sampling (Anderberg, 1973; Becker, Chambers, and Wilks, 1988; Everitt, 1974; Gordon, 1999; Hartigan, 1975; Legendre and Legendre, 2012; McQuitty, 1966; Murtagh, 1985; Murtagh and Legendre, 2014; Sneath and Sokal, 1973). Indeed, this analysis highlights the division into petrographic groups and subgroups providing a more detailed one, simultaneously tending to subdivide by archaeological site the samples belonging to the petrographic group granodioro-

Tab. 7) $^{87}Sr/^{86}Sr$ and $^{143}Nd/^{144}Nd$ isotopic ratios data of the selected sampling and raw material.

Sample	Site	Petrographic Group	Chemical Group	$^{87}Sr/^{86}Sr$ meas	2σ	$^{143}Nd/^{144}Nd$ meas	2σ
SEG6-4	SEG6	PG-1	CG-1	0.704178	±0.000007	0.512654	±0.000005
UA50-4-21	UA50	PG-1	CG-2	0.704681	±0.000006	0.512512	±0.000005
1Bis-1	SEG6	PG-1	CG-2	0.705062	±0.000007	0.512592	±0.000004
UA50-2-2	UA50	PG-2	CG-3	0.704836	±0.000006	0.512557	±0.000005
UA50-1-15	UA50	PG-2	CG-4	0.706313	±0.000006	0.512581	±0.000005
UA50-4-19	UA50	SPG-1	CG-5	0.707001	±0.000006	0.512571	±0.000004
4Bis-1	ES2	PG-4	CG-6	0.706641	±0.000007	0.512735	±0.000005
KG23c-C2-26	KG23c	SPG-2	CG-8	0.705138	±0.000006	0.512728	±0.000004
KG23c-D3-13	KG23c	SPG-2	CG-8	0.705466	±0.000006	0.512725	±0.000004
AAS1-112	ASS1	PG-2	CG-10	0.706862	±0.000006	0.512588	±0.000004
KG23c-C2-13	KG23	PG-2	CG-10	0.706392	±0.000007	0.512581	±0.000005
JAG-1928	JAG1	PG-2	CG-12	0.707203	±0.000006	0.512564	±0.000004
3-1	JAG1	PG-2	CG-12	0.707405	±0.000006	0.512571	±0.000005
AAS1-203	ASS1	PG-3	CG-13	0.715227	±0.000007	0.512561	±0.000005
AAS1-201	ASS1	PG-3	CG-13	0.710782	±0.000006	0.512712	±0.000004
JH1-7	JH1	PG-2	CG-14	0.706407	±0.000007	0.512474	±0.000004
JH1-10	JH1	PG-2	CG-15	0.705537	±0.000007	0.512505	±0.000005
JH1-11	JH1	PG-2	CG-15	0.705214	±0.000006	0.512503	±0.000005
JH1-2 RM	JH1			0.705357	±0.000004	0.512463	±0.000003
JH1-4 RM	JH1			0.705726	±0.000006	0.512504	±0.000003
JH1-1 RM	JH1			0.705253	±0.000006	0.512468	±0.000005

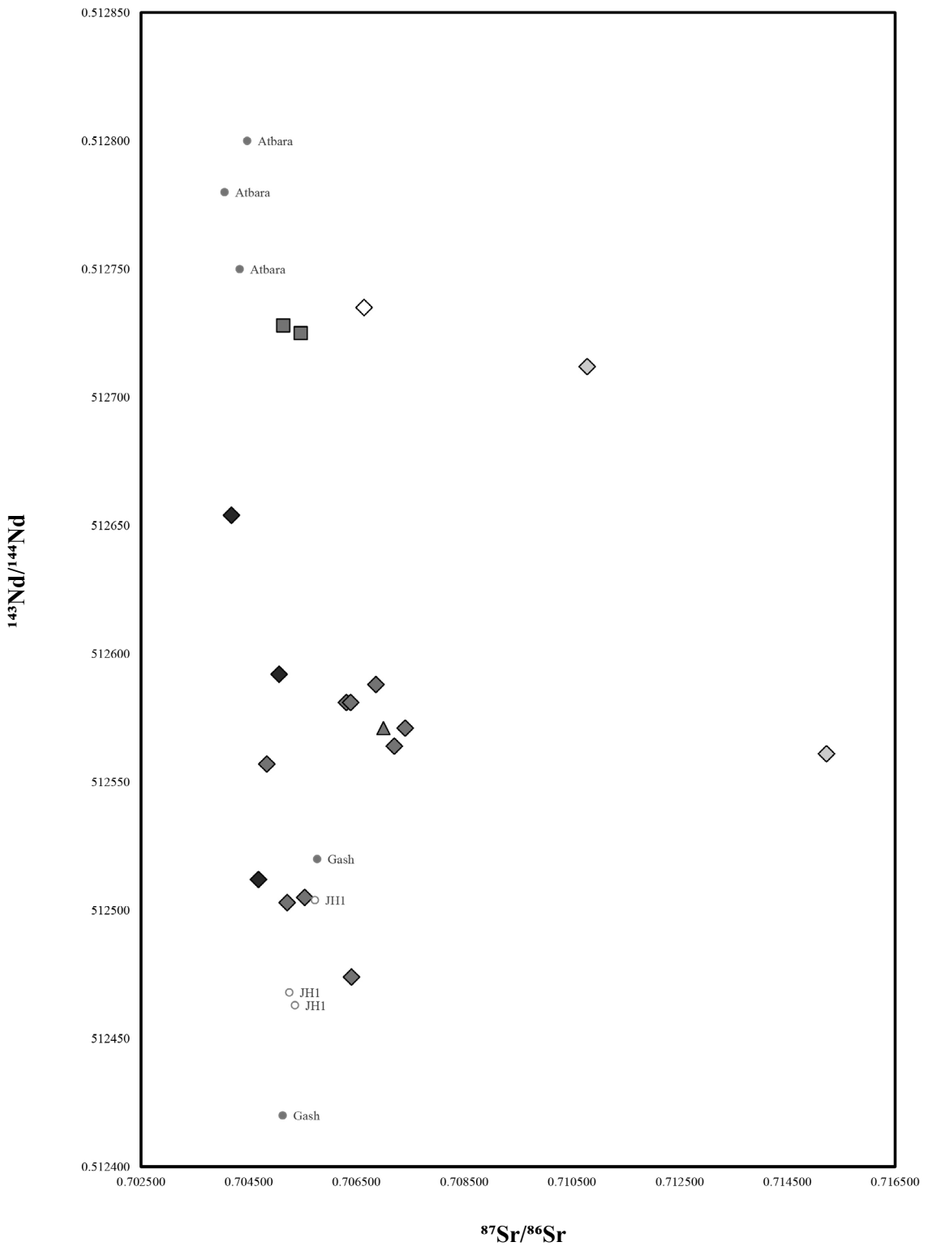

Fig. 54) $^{87}Sr/^{86}Sr$ versus $^{143}Nd/^{144}Nd$ binary diagram: Black rhombus, PT-Dioritic Gnesiss Inclusion; dark grey rhombus, PT-Granodioritic Gnesiss Inclusions; light grey rhombus, PT-Granitic Gnesiss Inclusions; white rhombus, PT-Tonalitic Gnesiss Inclusions; dark grey triangle, PT-Granodioritic Gnesiss + Basalt Inclusions; dark grey square, PT-Granodioritic Gnesiss + Limestone Inclusions, dark garey circle, Raw material from Padoan et. al, 2011; white circle, Raw material from JH1 site.

tic gneiss (Fig. 18; Fig. 19; Fig. 20; Fig. 21; Fig. 22; Fig. 23; Fig. 24; Fig. 25; Fig. 26; Fig. 27; Fig. 28; Fig. 29; Fig. 30; Fig. 31; Fig. 32; Tab. 2).

Indeed, the petrographic group granodiorite gneiss inclusion can be found in several sites (Tag. 5) being granodioritic gneiss the most commonly occurring lithotype in the area and the major contributor with its disintegration to make up the fluvial deposits (Abbate, 2022; Andersson et al, 2006; Drury and De Souza Filho, 1998; Garzanti et al, 2006; Gabert, 1960; Geological & Mineral Resources Department (G. M. R. D. Khartoum - Sudan), 1981; Ghebreab, 1996 ; Ghebreab, 2005; Jhonson, 2021; Padoan et al, 2011; Ruxton, 1956; Teklay, 1997; Vail, 1988). We speak of a tendency to subdivide by archaeological site because there are chemical groups falling into the latter petrographic group that comprise more and not all samples from an archaeological site (Tab. 5). This impurity can be explained either by the possibility of trade routes that cause a sample produced at one site to be found at another archaeological site, or by a limitation resulting from both methodological procedures and the natural variability inherent in the complex context under study. Indeed, it cannot be ruled out that the geological and geomorphological conditions occurring at one site are very similar to those at an adjacent site given the strong areal proximity, between them (Abbate, 2022; Andersson et al, 2006; Drury and De Souza Filho, 1998; Garzanti et al, 2006; Gabert, 1960; Geological & Mineral Resources Department (G. M. R. D. Khartoum - Sudan), 1981; Ghebreab, 1996 ; Ghebreab, 2005; Jhonson, 2021; Padoan et al, 2011; Ruxton, 1956; Teklay, 1997; Vail, 1988).

As described in detail above, each chemical group is explained by the sum of the attributes with positive outliers values and the sum of the attributes with negative outliers one. The chemical data, as just demonstrated, are those that were most successful in subdividing the sampling to the greatest degree of detail. Indeed, as reported in the section on the results in the parallelism between the mineralogical and chemical data, the mineralogical classification highlights the classification into petrographic groups and in part imperfectly justifies the chemical classification by making it dependent on the nature and mode of mineralogical phases present as inclusions. What is not explained in the chemical classification in this way is explained by the natural variability inherent in the complex geological setting.

Statistical analysis of the minimum Feret values frequency distributions allowed the extrapolation of the standard deviation and skewness. It was noted that the material used in cermic procuction had a particle size distribution distant from one peculiar to fluvial deposits, the only deposits naturally close to the archaeological sites, but rather was well sorted and either free of asymmetries or slightly asymmetrical towards the coarse fraction (Fig. 3; Tab. 2) (Folk, 1974; Friedmann, 1961). This proves the intentionality of choosing a raw material with these characteristics achievable through sieving or through natural decantation in specific points of the river deposit. Furthermore, this is supported by the low rounding degrees indicative of low transport inconsistent with such an accentuated sorting.

6.2. Firing condition

The presence of transitional vitrification structures (Fig. 41, b; Fig. 42; Fig. 43), of relict ones (Fig. 48), of the presence of fine porosity at high concentrations (Fig. 44; Fig. 46; Fig. 47; Fig. 48) and of the permanence of significant concentrations of illite/mica in incompatible thermal ranges (Fig. 52; Fig. 53; Tab. 7) generally lead to the definition of a fast temperature increase with a short stay of the ceramic body at the maximum temperature reached (Maniatis and Tite, 1981). However, there is also, rarely, the reverse case, that is samples kept at lower temperatures but for longer periods of time, demonstrated by the absence or low amount of illite/mica despite the fact that the temperature range allows for the existence of high amount of this phase (Fig. 52; Fig. 53; Tab. 7) (Maniatis and Tite, 1981; Gliozzo, 2020). The variation, among samples, in peaks intensities of the latter phase irregularly remarks an inverse proportionality with increasing degree of vitrification (Fig. 52; Fig. 53; Tab. 7) (Maniatis and Tite, 1981; Gliozzo, 2020). Furthermore, samples with the same degree of vitrification and different amount of the matrix fraction can have equal illite-mica referred peaks intensities (Fig. 52; Fig. 53; Tab. 2; Tab. 7) (Maniatis and Tite, 1981; Gliozzo, 2020). All this leads us to define the general tendency to brief firing times and also to unstandardized timings and therefore uncontrolled. Other evidence that makes us aware of how much the time factor is not controlled is the limited presence of the hematite and spinel neoformation phases to only two samples among all those presented vitrification states related to temperature ranges suitable for the formation of these phases (Fig. 52; Fig. 53; Tab. 2; Tab. 7) (Maniatis and Tite, 1981; Gliozzo, 2020).

The most stable information regarding the maximum temperature range achieved comes from the study of microstructure by FESEM. These ranges are shown in Table 7. As stated earlier there are two thermal groups: the first comprising more recent samples exhibits more high grade vitrification structures such as continue one adorned with both fine and medium porosity, while, in the second, containes older samples in which the occurrence of such vitrification states decreases dramatically. All this is indicative of a possibility in more recent times to reach higher temperatures in the firing process.

Regarding the discolorations, why the oxidized portion may or may not have the same vitrification structure as that occurring in the reduced portion depends on when the atmospheric changeover from reducing to oxidizing one occurs. If the influx of oxygen occurs near the maximum temperature then the outer portion is rearranged to the state of stable vitrification in the oxidizing atmosphere at the maximum temperature reached (Muan, 1957; Naslund, 1976) (Fig. 50; Tab. 7). However, retaining evidence, such as fine porosities, characteristic of the previous reducing atmosphere (Fig. 51; Tab. 7) (Maniatis and Tite, 1981). Whereas if the change takes place in the quenching phase the only change allowed is the chromatic one, indeed given the low temperatures no rearrangement of vitrification structures can take place and therefore those originated in the firing in the reducing atmosphere are re-proposed (Fig. 49; Tab. 7) (Maniatis and Tite, 1981). The atmosphere that contains the latter type of variation is referred to as R*.

The inflow of oxygen close to the maximum temperatures occurs almost entirely in

the most recent dated samples suggesting, along with the occurrence only in these samples of the high-grade vitrification structures, an technological advance inherent in both obtaining higher temperatures and controlling the inflow of oxygen.

7. Conclusions

The study just reported turns out to be one of the first of the archaeometric type inherent in the ceramic productions of southern Atbai. It provides to the scientific community a resolving key to the complex mineralogical, petrographic and chemical characteristics of this ceramic production. These characteristics depend on the raw materials used which reflect the complex geomorphological and geological context of Southern Atbai.

Actually, it is possible to state that there are no samples that show use of raw materials out of context; indeed, all samples are produced from raw materials consistent with the geological context of the area. Local supply is suggested in which each archaeological site employs its own deposit in its proximity. The classification and characterization achieved turns out to be important data to be employed in this to be employed in future studies to investigate the contacts of southern Atbai cultural groups within and outside this region, thus contributing to the delineation of the entire northeast African exchange network.

There is, moreover, an intentionality to employ a raw material possessing inclusions with a specific grain size and sorting. Intentionality this achieved either by appropriate sieving of material derived from river deposits or by selecting portions of the deposit where natural decantation had occurred.

The raw materials, once shaped, underwent firing whose conditions show improvement from the oldest to the most recent samples. Indeed, in the more recent samples, there appears a control of the firing environment, permanence at the maximum temperature and an increase in the same maximum temperatures reached, suggesting either different choices undertaken during the firing process or a transition from a pit firing to one in a structure that presents improvements. However, these choices and improvements are yet to be defined as well as their possible correlation between the establishment or interruption of contact between the southern Atbai cultural groups and other ones. In the case of correlation, the nature of the contact and its contribution in establishing or interrupting it can be assessed.

8. Bibliography

Abbate, E., Billi, P. 2022. Geology and Geomorphological Landscapes of Eritrea, in: Billi, P. (Eds.) Landscapes and Landforms of the Horn of Africa. World Geomorphological Landscapes. Springer, Cham, 41-80. https://doi.org/10.1007/978-3-031-05487-7_2.

Anderberg, M. R. 1973. Cluster Analysis for Applications. Academic Press, New York.

Andersson, U.B., Ghebreab, W., and Teklay, M. 2006. Crustal evolution and metamorphism in east-central Eritrea, south-east Arabian-Nubian Shield, Journal of African Earth Sciences, 44, 1, 45-65. doi: https://doi.org/10.1016/j.jafrearsci.2005.11.006.

Becker, R. A., Chambers, J. M. & Wilks, A. R. 1988. The New S Language. Wadsworth & Brooks/Cole Advanced Books & Software, Pacific Grove,

Barnard, H. and Duistermaat, K. 2012. The History of the Peoples of the Eastern Desert. Cotsen Institute of Archaeology Press, Los Angeles.

Carloni, D., Šegvić, B., Sartori, M., Zanoni, G., Moscariello, A., and Besse, M. 2021. Raw material choices and material characterization of the 3rd and 2nd millennium BC pottery from the Petit-Chasseur necropolis: Insights into the megalith-erecting society of the Upper Rhône Valley, Switzerland. Geoarchaeology, 36, 6, 1009-1044. doi: https://doi.org/10.1002/gea.21867.

Costanzo, S., Zerboni, A., Cremaschi, M. and Manzo, A. 2021. Geomorphology and (palaeo-)hydrography of the Southern Atbai plain and western Eritrean Highlands (Eastern Sudan/Western Eritrea), Journal of Maps, 17, 2, 51-62, doi: 10.1080/17445647.2020.1869112.

Cremaschi, M., D'Alessandro, A., Fattovich, R. and Piperno, M. 1986. Gash Delta Archaeological Project: 1985 Field Season. Nyame Akuma, 27, 7, 45-48.

Cucciniello, C., Avanzinelli, R., Sheth, H. and Casalini, M., 2022. Mantle and crustal contributions to the mount girnar alkaline plutonic complex and the circum-girnar mafic-silicic intrusions of saurashtra, northwestern Deccan traps. Journal of Petrology, 63, 3. doi: https://doi.org/10.1093/petrology/egac007.

De Bonis, A., Gassner, V., Ntaflos, T., Rizzo, M.L., Sauer, R., Serritella, A., Vassallo, S. and Bechtold, B., 2020. 5th-Century BC Himera and the Campanian Connection: Petrographic and Archaeological Studies on Western Greek Amphorae from Poseidonia and Elea Unearthed in the Necropolis of Himera. Minerals, 10, 3, 227. doi: https://doi.org/10.3390/min10030227.

Deer, W.A., Howie, R. A. and Zussman, J. 1997a. Single Chain Silicates (Rock-Forming Minerals) (v. 2A) Second Edition. Geological Society of London, London.

Deer, W.A., Howie, R. A. and Zussman, J. 1997b. Disilicates and Ring Silicatess (Rock-Forming Minerals) (v. 1B) Second Edition. Geological Society of London, London.

Deer, W.A., Howie, R. A. and Zussman, J. 1997c. Double Chain Silicates (Rock-Forming Minerals) (v. 2B) Second Edition. Geological Society of London, London.

Deines, P., Goldstein, S.L., Oelkers, E.H., Rudnick, R.L. and Walter, L.M. 2003. Standards for publication of isotope ratio and chemical data in Chemical Geology. Chemical Geology, 202, 1–2, 1-4. doi: https://doi.org/10.1016/j.chemgeo.2003.08.003.

Drury, S.A. and De Souza Filho, C.R. 1998. Neoproterozoic terrane assemblages in Eritrea: review and prospects, Journal of African Earth Sciences, 27, 3, 331-348, doi: 10.1016/S0899-5362(98)00066-9.

Everitt, B. 1974. Cluster Analysis. Heinemann Educational Books, London.

Fattovich, R. 1982. The Problem of Sudanese-Ethiopian Contacts in Antiquity: Status Quaestionis and Current Trends of Research. In J.M. Plumley (ed.), Nubian Studies. Proceedings of the Symposium for Nubian Studies: 76-86. Warminster, Aris & Phillips.

Fattovich, R. 1989a. The late prehistory of the Gash Delta (Eastern Sudan), in L. Krzyżaniak and M. Kobusiewicz (Eds.), Late Prehistory of the Nile Valley and the Sahara. Muzeum Archeologiczne w Poznaniu (Studies in African Archaeology 2), Poznań, 481-498.

Fattovich, R. 1989b. Il sito protostorico di Mahal Teglinos presso Kassala (Sudan Orientale). Rivista di Antropologia, 67, 221-238.

Fattovich, R. 1990. The peopling of the northern Ethiopian-Sudanese borderland between 7000 and 1000 BP: A preliminary model. Nubica, 1, 2, 3-45.

Fattovich, R. 1991. Ricerche archeologiche italiane nel delta del Gash (Kassala), 1980-1989, un bilancio preliminare. Rassegna di Studi Etiopici, 33, 1989, 89-130.

Fattovich, R. 1993. The Gash Group of the Eastern Sudan: an outline, in: L. Krzyżaniak, M. Kobusiewicz and J. Alexander (Eds.), Environmental Change and Human Culture in the Nile Basin and the Northern Africa until the Second Millennium BC. Muzeum Archeologiczne w Poznaniu (Studies in African Archaeology 4), Poznań, 439-448.

Fattovich, R. 2010. The Development of Ancient States in the Northern Horn of Africa, c. 3000 BC–AD 1000: An Archaeological Outline. Journal of World Prehistory 23, 145–175. doi: https://doi.org/10.1007/s10963-010-9035-1.

Fattovich, R., Marks, A.E. and Mohammed Ali, A. 1984. The archaeology of the Eastern Sahel, Sudan: preliminary results. African Archaeological Review 2: 173-188.

Fattovich, R., Sadr, K., and Vitagliano, S. 1988–1989. Society and territory in the Gash delta (Kassala, Eastern Sudan), 3000 BC–AD 300/400. Origini, 14, 329–357.

Fattovich, R., and Vitagliano, S. 1987. Gash Delta Archaeological Project: 1987

Field Season. Nyame akuma, 29, 56-59.

Folk, R.L. and Ward, W.C. 1957. Brazos River bar [Texas]; a study in the significance of grain size parameters. Journal of Sedimentary Research, 27, 1, 3–26. doi: https://doi.org/10.1306/74D70646-2B21-11D7-8648000102C1865D

Folk, R. L. 1966. A review of grain-size parameters. Sedimentology, 6, 2, 73-93.

Franciosi, L., D'Antonio, M., Fedele, L., Guarino, V., Tassinari, C. C. G., De Gennaro, R., & Cucciniello, C. (2019). Petrogenesis of the Solanas gabbro-granodiorite intrusion, Sàrrabus (southeastern Sardinia, Italy): Implications for Late Variscan magmatism. International Journal of Earth Sciences, 108, 989-1012. doi: https://doi.org/10.1007/s00531-019-01689-8.

Friedman, G. M. 1961. Distinction between dune, beach, and river sands from their textural characteristics. Journal of Sedimentary Research, 31, 4, 514-529.

Friedman, R. F. 2002. Egypt and Nubia. Gifts of the Deserts, The British Museum Press, London.

Gabert, G., Ruxton, B.P. and Venzlaff, H. 1960. Über untersuchungen im Kristallin der nördlichen Red Sea Hills im Sudan. Geologisches Jahrbuch, 77, 241-270.

Garzanti, E., Andò, S., Vezzoli, G., Abdel Megid, A. A. and El Kammar, A. 2006. Petrology of Nile River sands (Ethiopia and Sudan): Sediment budgets and erosion patterns, Earth and Planetary Science Letters, 252, 3–4, 327-341. doi: https://doi.org/10.1016/j.epsl.2006.10.001.

Ghebreab, W. 1996. An outline of major Pan-African lithologic assemblages and shear zones in Eritrea: implications for mineral exploration. Africa Geoscience Review, 3, 355–366.

Ghebreab, W., Talbot, C. J. and Page, L. 2005. Time constraints on exhumation of the East African Orogen from field observations and 40Ar/39Ar cooling ages of low-angle mylonites in Eritrea, NE Africa. Precambrian Research, 139, 1-2, 20-41. doi: https://doi.org/10.1016/j.precamres.2005.05.009.

Gordon, A.D. 1981. Classification, Chapman and Hall, London.

Guarino, V., de'Gennaro, R., Melluso, L., Ruberti, E., and Azzone, R. G. 2019. The Transition from miaskitic to agpaitic rocks, as highlighted by the accessory phase assemblages in the Passa Quatro alkaline complex (southeastern Brazil). The Canadian Mineralogist, 57, 3, 339-361. doi: https://doi.org/10.3749/canmin.1800073.

Hartigan, J.A. (1975). Clustering Algorithms. Wiley, New York.

Johnson, P.R. 2021. The Arabian-Nubian Shield, an introduction: historic overview, concepts, interpretations, and future issues, in: Hamimi, Z., Fowler, A.R., Li´egeois, J.-P., Collins, A., Abdelsalam, M.G., Abd Ei-Wahed, M. (Eds.), The Geology of the Arabian-Nubian Shield. Springer International Publishing, Cham, 1-38.

Leake, B. E., Woolley, A. R., Arps, C. E. S., Birch, W. D., Gilbert, M. C., Grice, J. D., Hawthorne, F. C., Kato, A., Kisch, H. J., Krivovichev, V. G., Linthout, K., Laird, J., Maresch, W. V., Nicke, E. H., Rock, N. M. S., Schumacher, J. C., Smith, D. C., Stephenson, N. C. N., Ungaretti, L., Whittaker, E. J. W. & Youzhi, G. (1997). Nomenclature of amphiboles: report of the Subcommittee on amphiboles of the International Mineralogical Association Commission on new minerals and mineral names. Mineralogical Magazine, 61, 295–321.

Legendre, P. and Legendre, L. 2012. Numercial ecology (3rd ed.). Elsevier, Amsterdam.

Maniatis, Y. and Tite, M.S. 1981. Technological examination of Neolithic-Bronze Age pottery from central and southeast Europe and from the Near East. Journal of Archaeological Science, 8, 1, 59-76. doi: https://doi.org/10.1016/0305-4403(81)90012-1.

Maniatis, Y., Katsanos, A. and Caskey, M. E. 1982. niatis, Y., Katsanos, A., Caskey, M.E., 1982. Technological examination of low-fired terracotta statues from Ayia Irini, Kea. Archaeometry, 24, 2, 191-198.

Manzo, A. 2011. Italian Archaeological Expedition to the Sudan of the University of Naples 'L'Orientale'. 2010 Field Season. Naples, Il Torcoliere, Università degli Studi di Napoli 'L'Orientale'.

Manzo, A. 2012. From the sea to the deserts and back: New research in Eastern Sudan. British Museum Studies in Ancient Egypt and Sudan, 18, 75-106.

Manzo, A. 2014. Beyond the Fourth Cataract: Perspectives for research in eastern Sudan, in: Anderson, J. R., and Welsby, D. A. (Eds.), The Fourth Cataract and Beyond, Peeters, London, 1149–1157.

Manzo, A. 2017. Eastern Sudan in its Setting: The archaeology of a region far from-the Nile Valley. Archaeopress, Oxford

Manzo, A., Coppa, A., Beldados Aleho, A., & Zoppi, V. 2010. Italian Archaeological Expedition to the Sudan of the University of Naples "L'Orientale", 2010 Field Season.

Manzo, A., Coppa, A., Beldados Aleho, A., & Zoppi, V. 2012. Italian Archaeological Expedition to the Sudan of the University of Naples 'L'Orientale'. 2011 Field Season. Il Torcoliere, Università degli Studi di Napoli 'L'Orientale, Naples.

Mardia, K. V., J. T. Kent, and J. M. Bibby (1979) Multivariate Analysis, London: Academic Press.

Marks, A.E. 1897. Terminal Pleistocene and Holocene hunters and gatherer in the eastern Sudan. African Archaeological Review, 5, 79–92. doi: https://doi.org/10.1007/BF01117084.

Marks, A.E. and Fattovich, R. 1989. The later prehistory of the Eastern Sudan: preliminary view, in: L. Krzyżaniak and M. Kobusiewicz (Eds.), Late Prehistory of

the Nile Valley and the Sahara. Muzeum Archeologiczne w Poznaniu (Studies in African Archaeology 2), Poznań, 451-458.

Marks, A.E. and Mohammed Ali, A. 1980. Survey of Northern Butana. Nyame Akuma 16: 30-35.

Marks, A.E. and Sadr, K. 1988. Holocene Environments and Occupations in the-Southern Atbai, Sudan: A Preliminary Formulation, in: J. Bower and D. Lubell (Eds.), Prehistoric Cultures and Environments in the Late Quaternary of Africa. British Archaeological Reports (British Archaeological Reports International Series 405, Cambridge Monographs in African Archaeology 26), Oxford, 69-90.

McQuitty, L.L. 1966. Similarity Analysis by Reciprocal Pairs for Discrete and Continuous Data. Educational and Psychological Measurement, 26, 4, 825–831. doi:10.1177/001316446602600402.

Murtagh, F. and Legendre, P. 2014. Ward's hierarchical agglomerative clustering method: which algorithms implement Ward's criterion? Journal of Classification, 31, 274–295. doi:10.1007/s00357-014-9161-z.vv.

Murtagh, F. 1985. Multidimensional Clustering Algorithms.Physica, Wurzburg.

Pik, R., Deniel, C., Coulon, C., Yirgu, G., Hofmann, C. and Ayalew, D. 1998. The northwestern Ethiopian Plateau flood basalts: Classification and spatial distribution of magma types. Journal of Volcanology and Geothermal Research, 81, 1–2, 91-111. doi: https://doi.org/10.1016/S0377-0273(97)00073-5.

Padoan, M., Garzanti, E., Harlavan, Y. and Villa, I.M. 2011. Tracing Nile sediment sources by Sr and Nd isotope signatures (Uganda, Ethiopia, Sudan). Geochimica et Cosmochimica Acta, 75, 12, 3627-3644. doi: https://doi.org/10.1016/j.gca.2011.03.042.

Quinn, P.S. 2022. Thin Section Petrography, Geochemistry and Scanning Electron-Microscopy of Archaeological Ceramics. Archaeopress, Oxford. doi: https://doi.org/10.2307/j.ctv2nwq8x4.

-Ruxton, B.P. 1956. The major rock groups of the northern Red Sea Hills, Sudan. Geol. Mag., 93, 4, 314-330. doi: https://doi.org/10.1017/S0016756800066723.

Salvatori, S. 2012. Disclosing Archaeological Complexity of the Khartoum Mesolithic: New Data at the Site and Regional Level. African Archaeological Review 29, 399–472. doi: https://doi.org/10.1007/s10437-012-9119-7.

Sneath, P.H.A. and, Sokal, R.R., 1973. Numerical Taxonomy. Freeman, San Francisco.

Spry A.,1969. Metamorphic Textures. Pergamon. Oxford

Shiner, J.L. 1971. The Prehistory and Geology of Northern Sudan, Part II. Dallas, unpublished report to the National Science Foundation, Grant GS 1192.

Teklay, M. 1997. Petrology, geochemistry and geochronology of Neoproterozoic magmatic arc rocks from Eritrea: implications for crustal evolution in the southern Nubian Shield. Department of Mines-Ministry of Energy Mines and Water Resources-State of Eritrea.

Terry, R.D., Chilingar, G.V., 1955. Summary of concerning some additional aids in studying sedimentary formations by M.S. Shvetsov. J. Sediment. Petrol. 25 (3), 229–234. https://doi.org/10.1306/74D70466-2B21-11D7-8648000102C1865D.

Trigger, B. G. 1994. Paradigms in Sudan Archaeology. The International Journal of African Historical Studies, 27, 2, 323–345. doi: https://doi.org/10.2307/221028

Vail, J.R. 1988. Lexicon of Geological Terms for the Sudan, Routledge, London. doi: https://doi.org/10.1201/9780203749036.

Venables, W.N. and Ripley B.D. 2002. Modern Applied Statistics with S. Springer, Berlin.

Winter J.D., 2001. An Introduction to Igneous and Metamorphic Petrology. Prentice Hal.